Online State and Parameter Estimation for Lithium-ion Batteries Based on a Reduced-order Electrochemical Life Model

by

Yalan Bi

A dissertation submitted to the Graduate Faculty of
Auburn University
in partial fulfillment of the
requirements for the Degree of
Doctor of Philosophy

Auburn, Alabama
May 02, 2020

Keywords: Estimation, Lithium-ion battery, Lithium plating, Nonlinear filtering, Parameter, Reduced-order model, State-of-charge, State-of-health, SEI layer.

Approved by

Song-Yul Choe, Chair, Professor of Mechanical Engineering
David M. Bevly, Professor of Mechanical Engineering
Roy Knight, Professor of Mechanical Engineering
John Y. Hung, Professor of Electrical and Computer Engineering

Abstract

Inaccurate estimation of the state-of-charge (SOC) and the state-of-health (SOH) may lead to safety issues. Currently, estimations of SOC and SOH that based on electric equivalent circuit models (ECMs) have been widely applied. ECMs consist of electrical elements, which do not represent electrochemical behaviors, so they lack the ability of long-term prediction of battery lives. Alternatively, an electrochemical-based reduced-order model (ROM) can predict internal states, such as concentrations and potentials, which are directly related to the SOC. Moreover, degradation mechanisms can be modeled and integrated into the ROM to predict change aging-related parameters such as loss of lithium ions, loss of active materials, consumption of the electrolyte solvent and increase of internal resistances, which are related to the SOH.

In this work, we propose an SOC and SOH estimator in conjunction with the beginning-of-life (BOL) and aging parameter estimation method based on a ROM. At first, a procedure for automatic estimation of parameters of a lithium-ion battery at the BOL is developed, where a two-step sensitivity analysis is designed to group the parameters and divide them by the best SOC window. Then, the genetic algorithm is applied to minimize a multi-objective function that is the mean square error of voltage for each SOC window.

Based on the ROM with accurately estimated parameters, an SOC estimation algorithm is developed using an adaptive square-root sigma-point Kalman filter (ASR-SPKF) with equality state constraints. Equality state constraints derived from the principle of charge conservation are introduced to improve the accuracy of both anode and cathode SOC estimations. Because of its fast convergence speed, the cathode SOC is used to represent the bulk SOC. Approaches used to adaptively update the covariance matrices of the filter based on the covariance matching method

are also incorporated. As a result, the covariance matrix of process noise is adjusted automatically. Comparative studies of three nonlinear filters concerning estimation accuracy, error bounds, recovery time from an initial offset, and computational time reveal that the ASR-SPKF has the most outstanding performance.

Finally, an online estimator for SOH and aging parameters is developed using a high-fidelity, reduced-order physics-based life model, where a pseudo-two-dimensional model coupled with degradation model of two types of side reactions—solid electrolyte interphase (SEI) layer formation and lithium plating—is used for the negative electrode, and a single particle model is used for the positive electrode to increase computational efficiency. A control-oriented incremental aging model is developed with the employment of a particle filter, from which the SOH and aging parameters are continuously monitored from real-time current and terminal voltage measurements. Finally, the developed method is tested in a battery-in-the-loop test station with a large format, 42 Ah, lithium-ion battery with $Li(NiMnCo)O_2$/Carbon electrode chemistry.

Acknowledgments

My deep gratitude goes first to my advisor, Dr. Song-Yul Choe, for giving me the opportunity to get involved in this research field. Without his guidance and persistent help this dissertation would not have been possible. My appreciation also extends to my committee members, Dr. David Bevly, Dr. Roy Knight, and Dr. John Hung, for their encouragement, insightful comments, and hard questions. Sincere thanks to my co-workers: Xinchen Zhao, Yilin Yin, Minseok Song, and Yang Hu, for the intense discussions and their support to my work. Last but not lease, I would like to thank my family, for their support and unconditional love.

Table of Contents

List of Tables

List of Figures

List of Symbols

A	sandwich area of the cell (m^2)
a_s	specific surface area of electrode (m^{-1})
c	ion concentration (mol m^{-3})
D	diffusion coefficient (m^2 s^{-1})
F	Faraday constant (96,487 C mol^{-1})
I	applied current (A)
i_0	exchange current density of intercalation (A m^{-2})
j	reaction rate of intercalation (A m^{-3})
k_0	isolation coefficient due to SEI
l	thickness of the micro cell (m)
Q	capacity of the cell (Ah)
q	amount of ion loss (Ah)
R	resistance (Ω) or universal gas constant (8.314 J mol^{-1} K^{-1})
R_s	radius of spherical electrode particle (m)
r	coordinate along the radius of electrode particle (m)
T	cell temperature (K)
t	time (s)

U potential (V)

V voltage (V) or volume of the composite electrode (m^3)

$\tilde{V}$ molar volume (m^3 mol^{-1})

x stoichiometric number of the anode

y stoichiometric number of the cathode

z output state of the nonlinear state-space model

Greek symbols

α transfer coefficient for an electrode reaction

δ thickness (m)

ε volume fraction of a porous medium

ϕ potential (V)

η overpotential of electrode reaction (V)

θ aging parameters

κ ionic conductivity (S m^{-1})

σ conductivity (S m^{-1})

λ fraction of plated lithium to form secondary SEI

Subscripts and Superscripts

a	anodic
aged	aged cell
ave	average
c	cathodic
e	electrolyte phase
eff	effective
eq	equality constraint
equ	equilibrium
ex	intermedium state of electrolyte concentration
fresh	fresh cell
i	index of the sigma point
int	intercalation
k	discrete-time sample index
lp	lithium plating
max	maximum
neg	negative composite electrode
pos	positive composite electrode

releasable	releasable capacity
s	solid phase
sep	separator
surf	electrode particle surface
sx	intermedium state of lithium ion concentration

List of Abbreviations

BMS battery management system

BIL battery-in-the-loop

BOL beginning-of-life

CC constant current

CV constant voltage

DFN Dolye-Fuller-Newman

DL deposit layer

DST dynamic stress test

EC ethylene carbonate

ECM equivalent circuit model

EIS electrochemical impedance spectroscopy

EKF Extended Kalman filter

EOL end-of-life

FOM full order model

GA Genetic algorithm

HPPC hybrid pulse power characteristic

KF Kalman filter

LM Levenberg-Marquardt

MPC model predictive control

NMC nickel manganese cobalt

OCV open-circuit voltage (V)

PDE partial differential equation

PF particle filter

PSO particle swarm optimization

P2D pseudo-two-dimensional

RNN recurrent neural network

ROM reduced order model

SEI solid electrolyte interphase

SEM Scanning Electron Microscopy

SOC state-of-charge

SOH state-of-health

SPKF sigma-point Kalman filter

SPM single particle model

UDDS urban dynamometer driving schedule

Chapter 1. Introduction

1.1 Background

In recent years, lithium-ion batteries have been widely used as rechargeable energy storage for hybrid electric vehicles, plug-in hybrid electric vehicles, and electric vehicles, due primarily to their high energy density as well as their long cycle life capability.

A lithium-ion battery is built from a number of principal components, which includes a negative electrode, a positive electrode, the electrolyte, a separator, and current collectors, as shown in Figure 1.

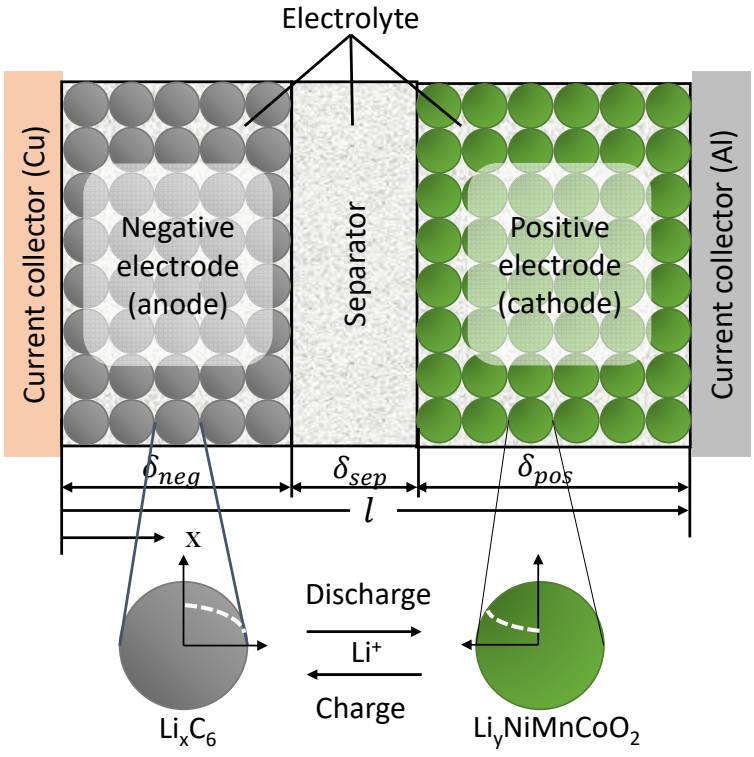

Figure 1. Schematic diagram of a lithium-ion battery.

The negative electrode of a lithium-ion battery is commonly made of graphite, whereas the positive electrode is often a metallic oxide—e.g., $Li(NiMnCo)O_2$ for a nickel-manganese-cobalt (NMC) cell. When a cell is fully charged, lithium is stored within the negative electrode. During discharge, the lithium atoms at the surface of the negative electrode particles give up electrons—which travel through the external circuit—and become positively charged lithium ions, which deintercalate from the negative electrode, and dissolve into the electrolyte. Conversely, lithium ions in the vicinity of the surface of the positive electrode particle receive electrons from the external circuit and becoming charge-neutral lithium atoms intercalate into the electrode. During charge, this process if completely reversed.

In practice, in order to increase the surface area of the electrodes, allowing easier lithium access, decreasing cell internal resistance, and enhancing power delivery capability, the electrodes are manufactured from a large number of small electrode particles with porous. In addition, the electrode materials are mixed with binders, such as polyvinylidene fluoride (PVdF), and conductive additives, such as carbon black, to adhere the particles together as well as enhance electron conduction.

To protect batteries from operating outside of its safe operating range, and continuously monitor battery states and parameters, a battery management system (BMS) is required, and two of the major tasks of a BMS are the state of charge (SOC) estimation, and state of health (SOH) estimation. The SOC is defined as the ratio of releasable charges stored in a battery and the maximum capacity of the battery. Electrochemically, SOC is related to the average concentration of lithium in the electrode particles. As shown in Figure 2, the SOC is at 100% when the average ion concentration in the negative electrode is at the highest while that in the cathode is at the lowest. Conversely, at 0% SOC, the ion concentrations of negative and positive electrode are reversed.

The SOH is a measure of the changes to battery health-related parameters. It is common to estimate SOH in terms of cell present total capacity and internal resistance, which are also known as capacity fade, and power fade, respectively.

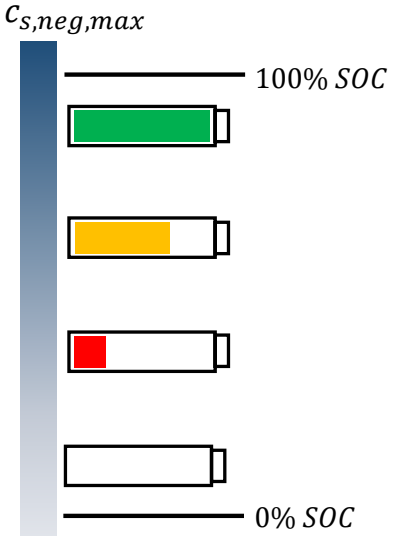

Figure 2. Relationship between negative-electrode average lithium concentration and SOC.

1.2 Motivation and objectives

Inaccurate estimation of SOC and SOH may lead to safety issues. SOC measures the releasable charge of an electrode, which is directly related to lithium ion concentration inside electrodes. SOH, on the other hand, indicates aging status, which is related obtained by evaluating capacity fade and the power fade. Currently, estimations methods based on electric equivalent circuit models (ECMs) have been widely applied [1]. ECMs use electrical-circuit analogies to approximate voltage response of a cell to different input currents, which lack the ability to predict cell internal electrochemical dynamics, so they exhibit limited long-term prediction power of battery lives. On the contrary, an electrochemical-based reduced-order model (ROM) can predict internal states, such as concentrations and potentials, which are closely related to the SOC.

Moreover, degradation mechanisms can be modeled and integrated into the ROM to predict the change of aging-related parameters such as loss of lithium ions, loss of active materials, consumption of the electrolyte solvent and increase of internal resistances, which are related to the SOH.

However, in order to implement ROM in the battery management system (BMS), several technical challenges need to be addressed. One is the difficulty of the identification of the parameters of the model. For example, parameters such as diffusion coefficients are dependent on the operating conditions and are therefore hard to measure unless carrying out the material analysis. The second is the accurate estimation of SOC based on the ROM in conjunction with an efficient adaptive estimator, which enables real-time implementation in the BMS hardware. The other is the lack of incorporation of different degradation mechanisms such as solid electrolyte interphase (SEI) layer formation and lithium plating into online estimation, especially under different input profiles and temperatures.

Therefore, it is imperative to develop a method that can efficiently find a set of optimal parameters, as well as can accurately estimate electrochemical and aging states of a battery. The objective of this proposal is to develop an online state and parameter estimation method based on a ROM, which predicts the end-of-charge/discharge and end-of-life (EOL) under different input profiles, and ambient temperatures. More specifically, these objectives are 1) Development of a ROM with an automatic parameter estimation scheme. 2) Development of a SOC and internal state estimation method. 3) Development of a SOH and aging parameter estimation method up to 20% capacity fade with the consideration of input current and temperature effect.

1.3 Scholarly contributions and dissertation structure

The parameter and state estimation methods developed in this work could make certain scholarly contributions since it is one of the first attempts to estimate states and parameters for lithium-ion batteries based on a ROM through a lifetime. In particular, the contributions are:

- The parameters of a ROM are automatically estimated and optimized that replaces the time-consuming manually tuning process or material analysis.
- An adaptive SOC estimation algorithm based on a square-root sigma-point Kalman filter (SR-SPKF) is developed considering charge conservation as equality constraints that improve the robustness of the estimator and accuracy of estimated SOC.
- A new online SOH and aging parameter estimation algorithm is developed with the consideration of the physical causes of degradation such as SEI layer formation and lithium plating.

This dissertation is organized as follows.

- Chapter 1 introduces the research background, motivation and objectives, and scholarly contributions.
- Chapter 2 includes a brief introduction to the electrochemical governing equation and order reduction techniques. An automatic parameter estimation procedure is developed including grouping, sensitivity analyses, and parameter optimization.
- Chapter 3 presents an online internal state and SOC estimation method that is developed based on an adaptive SR-SPKF with the consideration of cyclable charge conservation as equality constraints. A comparative study is conducted and the proposed method is validated against the BIL test at different charging conditions and temperatures.

• Chapter 4 describes an online aging parameter and SOH estimation method that is developed using a particle filter based on a degradation model with the consideration of two different side reactions—SEI layer formation and lithium plating. The proposed method is validated against the BIL test at different charging conditions and temperatures.

• Chapter 5 concludes the dissertation.

Chapter 2. Automatic parameter estimation for BOL

2.1 Review of parameter estimation methods

A number of recent studies have addressed the parameter estimation methods that can be divided into gradient and non-gradient based methods. Santhanagopalan et al. proposed a parameter estimation method for a ROM based on a least-square framework using the Levenberg-Marquardt (LM) method, which was validated against the experimental data up to 2C [1]. However, with inappropriate parameter initialization, the LM method may drive the objective function to a local minimum, which ends up with false optimal values. To resolve the problem of local optimum entrapment, Forman et al. used a genetic algorithm (GA) to find the values of 88 parameters extracted from a Doyle-Fuller-Newman (DFN) model [2]. The parameters were estimated using two driving cycles and then validated using another five driving cycles. Simulations showed a good match with the experimental data, but only at low C-rate discharge (≤1C). In addition, it took three weeks to complete the calculation of the parameter set on a cluster of computers without grouping or ranking the parameters. Jokar et al. proposed another parameter estimation method using the GA that considered both low (≤1C) and high (>1C) C-rates discharge. Based on a simplified DFN model, the model parameters were separated and optimized by time intervals obtained from sensitivity analyses of discharge characteristics [3]. The proposed method was tested with batteries with different electrode materials like $LiCoO_2$, $LiMn_2O_4$, and $LiFePO_4$ [4]. However, the parameters estimated using discharge characteristics may not be appropriate for validations of charging or driving cycles. A similar heuristic computation method, particle swarm optimization (PSO), was employed to estimate four parameters of a $LiCoO_2$ battery [5], where the fitness function reached the minimum value within 100 iterations. However, the fast convergence was achieved by setting the initial values of estimated parameters as obtained from the literature.

The studies mentioned above reveal that LM as a gradient-based algorithm allows for a fast convergence but does not guarantee the global minimum. In addition, it is error-prone to calculate the derivatives for a complex system like the ROM. Conversely, gradient-free algorithms such as the GA and the PSO, allow for easy implementation and convergence of a global minimum but consume a relatively considerable amount of time. In this section, we proposed an automatic parameter estimation procedure for a lithium-ion battery at the BOL. The procedure enables one to find a set of parameters without conducting postmortem analysis, regardless of formats or designs, and without putting a vast effort by manual tuning. This procedure consists of a grouping of parameters, defining objective functions and optimization. The grouping is carried out based on two criteria, sensitivity of the parameters under influences of charging and discharging characteristics, and SOC. The objective functions are defined as the L^2 norm of the voltage errors for each SOC window and are minimized by the GA that results in a set of optimal parameters. Constant current charge and discharge profiles at different C-rates are used for the optimization process. The ROM with the automatically estimated parameters is validated against data obtained from two cycling tests. Additionally, voltage errors are evaluated to assess the performance of the proposing procedure.

2.2 Model development

2.2.1 Governing equations

The ROM used in this study is based on the concentrated solution and porous electrode theory, coupled with electrochemical kinetics to describe cell physical behavior along electrode and separator thickness and the electrode particle radius direction. The governing equations are a set of nonlinear PDEs coupled with a nonlinear algebraic equation, as given in Table 1. The

equations consider the principles of mass conservation, charge conservation, and electrochemical kinetics. Finally, the terminal voltage is calculated according to the difference of cell potential, ϕ_s, at two current collectors in conjunction with the voltage drop caused by the film resistance of the cell. These equations can be numerically solved by applying either the finite difference method or the finite element method. In fact, the computational power needed for solving such a full order model (FOM) is high compared to an ECM. Therefore, the FOM is further reduced in order to implement it into the BMS.

Table 1 Governing equations of the FOM.

Ion concentration in the electrode	$\frac{\partial c_s}{\partial t} = \frac{D_s}{r^2}\frac{\partial}{\partial r}\left(r^2 \frac{\partial c_s}{\partial r}\right)$; $\left.\frac{\partial c_s}{\partial r}\right\|_{r=0} = 0, \left.\frac{\partial c_s}{\partial r}\right\|_{r=R_s} = -\frac{1}{D_s F a_s} j^{Li}$.
Ion concentration in the electrolyte	$\frac{\partial(\varepsilon_e c_e)}{\partial t} = \frac{\partial}{\partial x}\left(D_e^{eff}\frac{\partial}{\partial x}c_e\right) + \frac{1-t_+^0}{F} j^{Li}$; $\left.\frac{\partial c_e}{\partial x}\right\|_{x=0} = \left.\frac{\partial c_e}{\partial x}\right\|_{x=l} = 0$.
Potential in the electrode	$\frac{\partial}{\partial x}\left(\sigma^{eff}\frac{\partial}{\partial x}\phi_s\right) - j^{Li} = 0$; $-\sigma_{neg}^{eff}\left.\frac{\partial \phi_s}{\partial x}\right\|_{x=0} = \sigma_{pos}^{eff}\left.\frac{\partial \phi_s}{\partial x}\right\|_{x=l} = \frac{I}{A}$; $\left.\frac{\partial \phi_s}{\partial x}\right\|_{x=\delta_{neg}} = \left.\frac{\partial \phi_s}{\partial x}\right\|_{x=\delta_{neg}+\delta_{sep}} = 0$.
Potential in the electrolyte	$\frac{\partial}{\partial x}\left(\kappa^{eff}\frac{\partial}{\partial x}\varphi_e\right) + \frac{\partial}{\partial x}\left(\kappa_D^{eff}\frac{\partial}{\partial x}\ln c_e\right) + j^{Li} = 0$; $\left.\frac{\partial \phi_e}{\partial x}\right\|_{x=0} = \left.\frac{\partial \phi_e}{\partial x}\right\|_{x=l} = 0$.
Electrochemical kinetics	$j^{Li} = a_s i_0 \left\{\exp\left[\frac{\alpha_a F}{RT}\eta\right] - \exp\left[-\frac{\alpha_c F}{RT}\eta\right]\right\}$.

2.2.2 Reduced-order model

Since solving coupled nonlinear PDEs is computationally intensive, a ROM is derived, which is a single-particle model with electrolyte dynamic incorporated that is similar to Ref. [1,6]. However, different order reduction techniques, such as Padé approximation and residual grouping methods, are applied to further reduced the computational complexity [7]. The reduction and simplification methods for each equation are described below.

2.2.2.1 Ion concentration in solid

The Padé approximation was used to simplify the equation of ion concentration in electrodes, resulting in a linear state-space subsystem:

$$\dot{c}_{sx} = \mathrm{A}_{cs} c_{sx} + \mathrm{B}_{cs} j^{Li} \text{ and} \tag{1}$$

$$\begin{bmatrix} c_{s,surf} \\ c_{s,ave} \end{bmatrix} = \begin{bmatrix} \mathrm{C}_{cs,surf} \\ \mathrm{C}_{cs,ave} \end{bmatrix} c_{sx} \tag{2}$$

.

The initial conditions for Eq. (1) were obtained by assuming that the system is initially at a steady state. When a battery is at rest, the input of the system is $j^{Li} = 0$. Therefore, no concentration gradient is formed, and thus, $c_{s,surf} = c_{s,ave} = c_{s,0}$.

The states of Eq. (1) contain information regarding the ion concentration of the particle surface, $c_{s,surf}$, and the volume-averaging concentration, $c_{s,ave}$, which represent the outputs of the subsystem. $c_{s,surf}$ and $c_{s,ave}$ are critical internal variables because of their direct relationship with the SOC and overpotential. The order of the subsystem is determined by the order of the Padé approximation. A third order was chosen from the tradeoff between accuracy and computational complicity, which results in six states in total for positive and negative electrodes.

2.2.2.2 Ion concentration in electrolyte

A third-order residual grouping method was employed to calculate the average lithium ion concentration in the electrolyte, where the intercalation current density, as an input to the subsystem, was assumed to be uniform for each electrode, as shown in Eq. (3):

$$j_{neg}^{Li} = \frac{I}{a_{s,neg}\delta_{neg}A} \text{ and}$$
$$j_{pos}^{Li} = -\frac{I}{a_{s,pos}\delta_{pos}A}. \tag{3}$$

Similar to Eqs. (1) and (2), a linear state-space representation was derived that contains three intermediate states, in conjunction with the electrolyte as the output,

$$\dot{c}_{ex} = \mathrm{A}_{ce}c_{ex} + \mathrm{B}_{ce}j^{Li} \text{ and}$$
$$c_e = \mathrm{C}_{ce}c_{ex} + \mathrm{D}_{ce}j^{Li}. \tag{4}$$

Eq. (4) is a third-order linear system with matrices A_{ce}, B_{ce}, C_{ce}, and D_{ce} with the dimensions of 3×3, 3×2, $M\times3$, and $M\times2$, respectively, where M denotes the number of node points along the microcell thickness direction.

2.2.2.3 Potentials in electrolyte

The intercalation current density is also the input for calculating the potential in the electrolyte, ϕ_e. Due to the averaged value of the electrolyte concentration, the gradient of c_e is zero, and the equation can be simplified as follows:

$$\frac{\partial}{\partial x}\left(\kappa^{eff}\frac{\partial}{\partial x}\varphi_e\right) + j^{Li} = 0. \tag{5}$$

Under the assumption that the effective ionic conductivity, κ^{eff}, in each domain is constant, the difference of ϕ_e between current collects can be explicitly calculated as

$$\phi_e(l,t) - \phi_e(0,t) = -\frac{I}{2A}\left(\frac{\delta_{neg}}{\kappa_{e,neg}^{eff}} + \frac{2\delta_{sep}}{\kappa_{e,sep}^{eff}} + \frac{\delta_{pos}}{\kappa_{e,pos}^{eff}}\right). \quad (6)$$

2.2.2.4 Electrochemical kinetics

The current density is also described using Butler-Volmer equation:

$$j^{Li} = a_s i_0 \left\{ \exp\left[\frac{\alpha_a F}{RT}\eta\right] - \exp\left[-\frac{\alpha_c F}{RT}\eta\right] \right\}, \quad (7)$$

where i_0 is the exchange current density:

$$i_0 = k(c_e)^{\alpha_a}\left(c_{s,\max} - c_{s,surf}\right)^{\alpha_a}\left(c_{s,surf}\right)^{\alpha_c}. \quad (8)$$

Since the same number of charges are transported between the anode and cathode during operation, both charge-transfer coefficients, α_a and α_c, are equal to 0.5, and the activation overpotential is expressed as

$$\eta = \frac{RT}{\bar{\alpha}F}\sinh^{-1}\left(\frac{j^{Li}}{2a_s i_0}\right), \quad (9)$$

where $\bar{\alpha} = 0.5$.

Note that the activation overpotential can also be expressed as

$$\eta = \phi_s - \phi_e - U_{equ}, \text{ or } \phi_s = U_{equ} + \phi_e + \eta. \quad (10)$$

Therefore, the output terminal voltage is computed as

$$\begin{aligned} V_t &= \phi_s(l,t) - \phi_s(0,t) - R_{film} \cdot I \\ &= U_{equ,pos}(l,t) - U_{equ,neg}(0,t) + \phi_e(l,t) - \phi_e(0,t) + \eta_{pos}(l,t) - \eta_{neg}(0,t) - R_{film} \cdot I \end{aligned} . \quad (11)$$

2.3 Design of automatic parameter estimation method

2.3.1 Sensitivity analysis

At the beginning-of-life (BOL), the developed ROM has 20 parameters that are listed in Table 2. The values of parameters are obtained from the manufacturer, literature, or measurements. In particular, the diffusion coefficients can be measured by examining voltage response to a dc current, and the stoichiometric numbers can be measured by doing postmortem analyses [8]. However, these tests are time-consuming and often times impractical outside specialized laboratory environments. Otherwise, the parameters can be found by manual tuning, which is based on trial and error and therefore challenging to find the optimal values. Therefore, it is imperative to develop an automatic procedure that can efficiently find a set of optimal parameters.

Table 2. Sources of parameters at the BOL.

Source	Parameter	Symbol	Unit
Manufacturer	Electrode plate area	A	cm^2
	Thickness	δ	cm
	Particle radius	R_s	cm
	Active material volume fraction	ε_s	-
	Porosity	ε_e	-
	Polymer phase volume fraction	ε_p	-
	Conductive filler volume fraction	ε_f	-
	Maximum solid phase concentration	$c_{s,max}$	$mol \cdot cm^{-3}$
Experimental measurement or estimation	Diffusion coefficient in solid	$D_{s,neg}$,$D_{s,pos}$	$cm^2 \cdot s^{-1}$
	Diffusion coefficient in electrolyte	D_e	$cm^2 \cdot s^{-1}$
	Stoichiometry at 0% SOC	x_0, y_0	-

	Stoichiometry at 100% SOC	x_{100}, y_{100}	-
	Film resistance	R_{film}	Ω
Literature	Exchange current density [9]	i_0	$A \cdot cm^{-2}$
	Charge transfer coefficients [9,10]	α_a, α_c	-
	Bruggeman exponent [11]	P	-
	Electrolyte phase ionic conductivity [12,13]	σ	$S \cdot cm^{-1}$
	Li+ transference number [9,10,12]	t_+^o	-
	Equilibrium potential of positive electrode [14]	$U_{equ,pos}$	-
	Equilibrium potential of negative electrode [15]	$U_{equ,neg}$	-

Out of 20 parameters, we selected eight parameters because of their dependency on operating conditions. They are the diffusion coefficients in solid and electrolyte phase ($D_{s,neg}$,$D_{s,pos,}$ D_e), the stoichiometry numbers at 0% and 100% SOC of positive and negative equilibrium potentials ($x_{0,}$ $y_{0,}$ $x_{100,}$ y_{100}), and a film resistance (R_{film}). Values of diffusion coefficients in the solid phase are dependent on the size and porosity of particles and temperature, while the value of the electrolyte is affected by temperature only. Besides, the values vary widely depending on different chemistries used for electrodes and electrolytes [4]. The stoichiometry numbers at 0% and 100% SOC are estimated so that the difference of the equilibrium potentials coincides with the measured OCV. The film resistance is a sum of the internal resistance of the cell, which is directly related to the battery terminal voltage.

The sensitivity analysis procedure is depicted in Fig. 1, which is performed automatically without being interrupted by any manual tuning. It includes two sub-procedures, deviation, and Jacobian analysis. The former is used to decide estimation sensitivity of parameters and the latter is to study the sensitivity of parameters in the SOC domain.

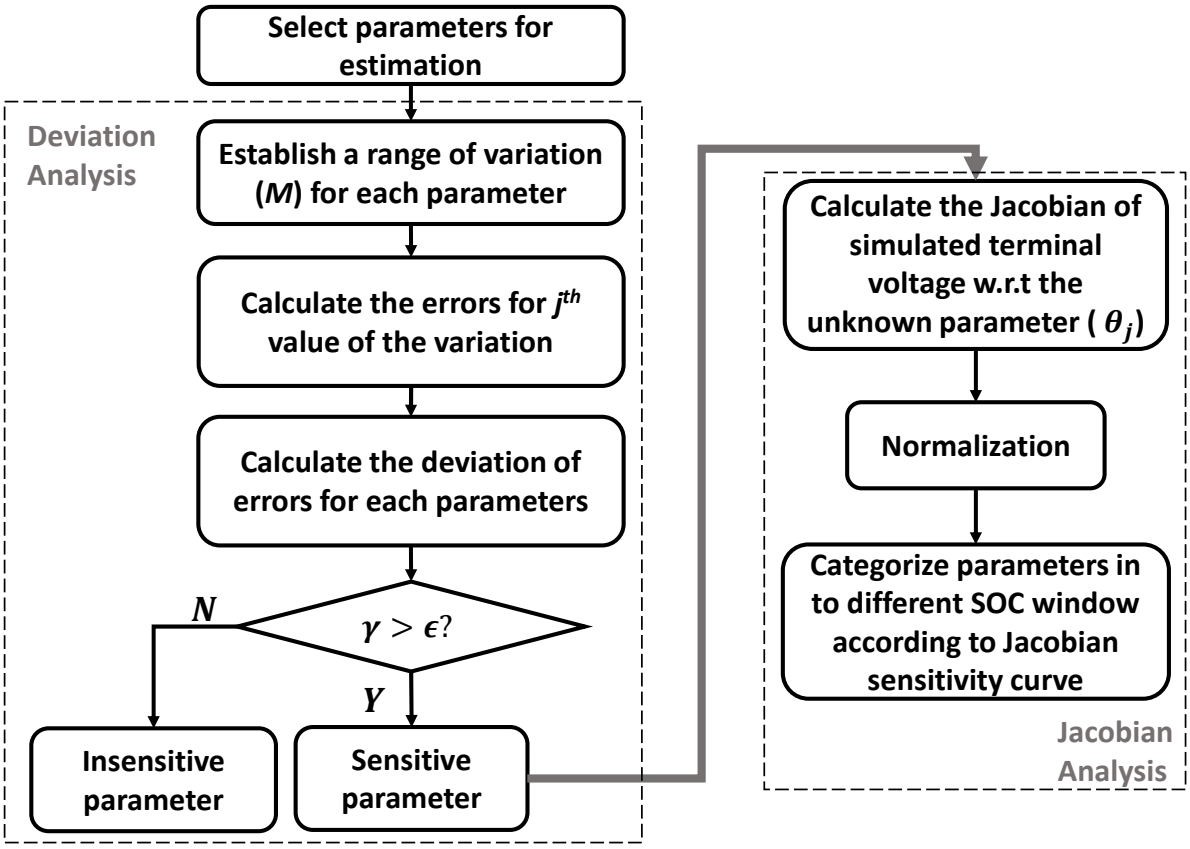

Figure 3. Procedure of parameter sensitivity analysis.

In order to decide the sensitivity of parameters, a range of variations of each parameter ($\boldsymbol{\theta}$) is arbitrarily set, and then several values within the range are selected and used to calculate terminal voltages of charge and discharge processes. The resulting relative error that is defined as a root-mean-square error is calculated for each simulation:

$$Error_i = \left(\frac{1}{N} \sum_{k=1}^{N} \left(\frac{V_{\exp}[k] - V_{sim,i}[k]}{V_{\exp}[k]} \right)^2 \right)^{\frac{1}{2}}, \tag{12}$$

where k and N denote the *kth* data point and the total number of data points, respectively. i represents the *ith* parameter variation. The subscripts *exp* and *sim* denote the voltage data obtained from experiments and simulations, respectively.

Then, a normalized deviation of the errors (γ) for each parameter is calculated as follows:

$$\gamma = \frac{\sum_{i=1}^{M} (Error_i - Error^*)}{M}, \tag{13}$$

where M is the total number of variations of parameters within its range. $Error^*$ is the error calculated from the reference value.

Finally, a threshold value (ε) is introduced to group insensitive and sensitive parameters, where ε is set as 10^{-4} with the standard deviation of 1% of the relative error. The grouping results show that the three sensitive parameters are the film resistance (R_{film}) and the solid phase diffusion coefficient of the positive and negative electrodes ($D_{s,p}$ and $D_{s,n}$).

On the other hand, a Jacobian analysis is carried out to determine the sensitivity characteristics of SOC domain. The Jacobian matrix, J, is calculated as the first order partial derivative of the simulated terminal voltages for the sensitive parameters (θ_j), as follows:

$$J(\theta_j) = \frac{\partial V_{sim}}{\partial \theta_j}. \tag{14}$$

Due to the coupled equations showed in Table I, J cannot be expressed as an explicit form, so J is expressed using a finite difference method:

$$\frac{\partial V_{sim}}{\partial \theta_j} = \frac{V_{sim}\left(\theta_j + \Delta\theta_j\right) - V_{sim}\left(\theta_j\right)}{\Delta\theta_j}. \tag{15}$$

Because the Jacobian matrices have different orders of magnitudes for different parameters, a dimensionless expression is introduced as

$$J_{\theta_j} = \theta_j^* J\left(\theta_j\right), \tag{16}$$

where θ_j^* is the reference value of the corresponding parameter.

The dimensionless Jacobian matrices as a function of SOCs of the three sensitive parameters for 1C are plotted in Figure 4 because of similar trends at other C-rates. For each of the parameters, the dimensionless Jacobian values vary with different SOCs. The higher the values are, the higher the sensitivity becomes. The magnitudes of $D_{s,pos}$ are always greater than those of the $D_{s,neg}$, which implies that the diffusion coefficient of the positive electrode is much more sensitive than that of the negative electrode. This is because the magnitudes of the equilibrium potential of the positive electrode are much greater than those of the negative electrode. The dimensionless Jacobian values of R_{film} is constant except for constant-voltage (CV) charge processes, which indicates that this parameter has the same sensitivity over the entire constant-current (CC) region. In addition, the signs of the Jacobian matrices at charge and discharge are always opposite. In other words, when altering the value of a parameter, if the charge curve goes upward, then the discharge curve goes downward, and vice versa. Therefore, both characteristics should be considered to find optimal values of parameters.

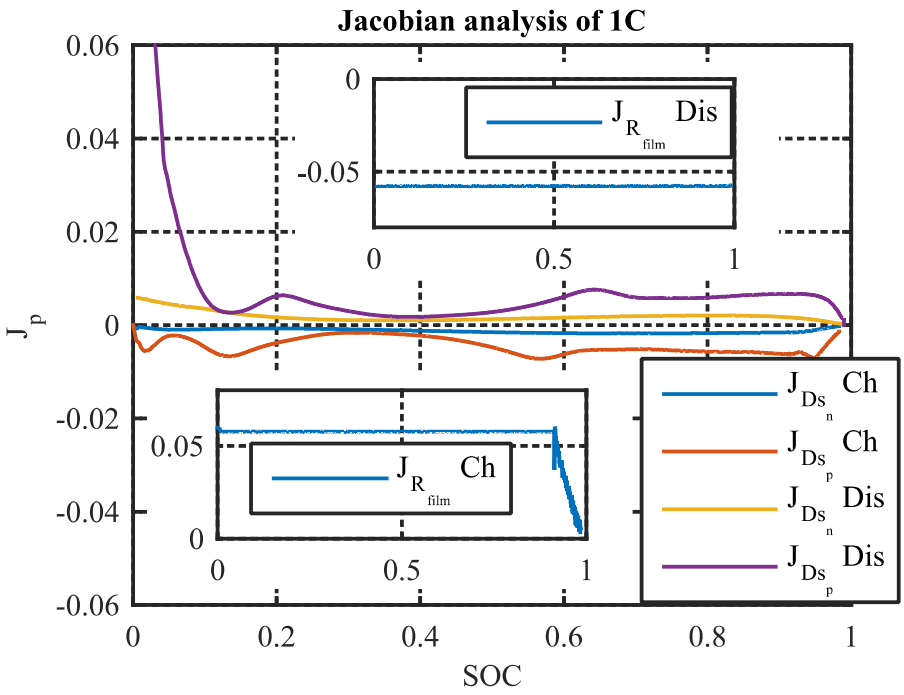

Figure 4. Sensitivity characteristics of charge and discharge curve at 1C.

Based on the sensitivity characteristics in Figure 4, the SOC domain is divided into two regions at discharge and three regions at charge depending upon the magnitudes of J_θ, as shown in Table 3. For the charging process, region I starts from 0% SOC to 10%, where $D_{s,pos}$ and R_{film} are considered, while in the region II, all three parameters are considered. Region III is in the CV mode, where R_{film} is considered since its sensitivity is not affected by the SOC. Similarly, the discharge process is divided in the same fashion as the charging process without the CV region.

Table 3. Best SOC domain for estimation.

Region	I	II	III
SOC range	**0-10%**	**10%-100%**	**CV (if applicable)**
Charge	$D_{s,pos}$, R_{film}	$D_{s,pos}$, $D_{s,neg}$, R_{film}	R_{film}
Discharge	$D_{s,pos}$, R_{film}	$D_{s,pos}$, $D_{s,neg}$, R_{film}	_

2.3.2 Objective function

The objective functions are defined as the L^2 norm of the error given by the difference between the experimental and the simulation data for each SOC window. The SOC can be estimated using a coulomb counting method, where an initial SOC and the input current are known for a charge or discharge profile.

$$\min_{\theta_j} \begin{cases} \sum_{k \in regionI} \left(V_{\exp}[k] - V_{sim,j}[k] \right)^2 \\ \sum_{k \in regionII} \left(V_{\exp}[k] - V_{sim,j}[k] \right)^2 \\ \sum_{k \in regionIII} \left(V_{\exp}[k] - V_{sim,j}[k] \right)^2 \end{cases} \tag{17}$$

subject to $\theta_{j,\min} \le \theta_j \le \theta_{j,\max}$,

where V represents voltage that is the output of the model or of the experiment. $\theta_{i,min}$ and $\theta_{i,max}$ are lower and upper bounds of each parameter.

2.3.3 Optimization

A goal of optimization processes is to minimize the objective function. An overall estimation process with current as input is depicted in Figure 5. The voltage errors between experiment and simulation by ROM at every time step, and the corresponding SOCs, are calculated to obtain the value of the objective functions. Then the parameters of ROM are updated, and the estimation process is repeated until the stopping criterion is met. After the process has been completed, the model parameters are produced as outputs.

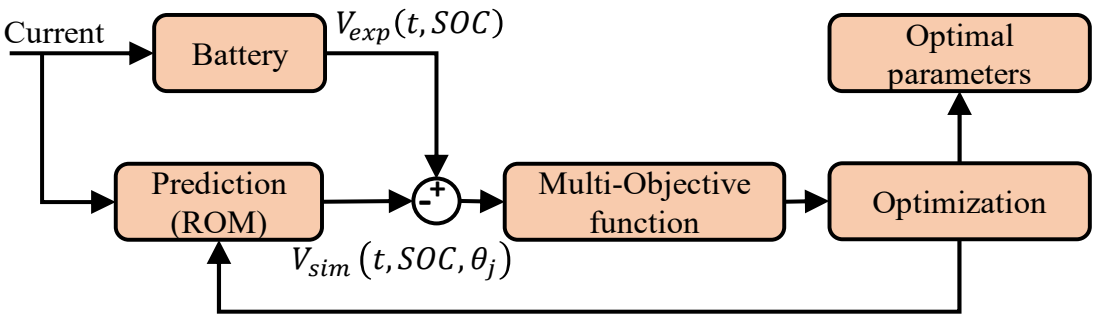

Figure 5. Concept of parameter estimation process.

A number of optimization methods have been applied to solve the problem. These methods can be categorized into deterministic and stochastic approaches. The deterministic approach requires an explicit form of the first or second order derivatives. Due to its high sensitivity to the initial guess, it likely results in a local minimum. On the other hand, a stochastic approach such as the GA guarantees a global optimization and its convergence speed can be increased using a multi-objective function. Thus, the GA was chosen.

To start the estimation process, initial values of parameters are randomly selected within a given range determined empirically. Then the iteration process begins, in which a new generation of parameters produced to replace the old generation based on the objective function. The new generation is produced in three ways: selection, crossover, and mutation. The selection is established based on the probability that is determined by the value of the objective function calculated at each iteration. The crossover and mutation reproduce new parameters by combining the old parameters with those randomly selected. Once the value of the objective function reaches one of two tolerances, either the minimum relative change in the objective function value or the number of generations that exceeds the maximum generation, this process is completed and exports the estimated parameters. The tolerances are set to 1e-4 and 50, respectively.

2.4 Result and discussion

The automatically estimated parameters are exported after applying the GA procedure. Units, starting ranges as well as estimated values are listed in Table 4.

Table 4. Estimated parameters.

Symbol	**Unit**	**Range**		**Estimated value**
		min	*max*	
$D_{s,pos}$	cm2·s-1	1e-11	1e-9	7.69e-10
$D_{s,neg}$	cm2·s-1	1e-11	1e-9	9.50e-10
R_{film}	Ω	0	50	9.68

Even though the optimization takes place in the SOC domain, performance is examined in the time domain to check its practicability. Comparisons between simulations and experiments carried out with different C-rates show a good agreement, as plotted in Figure 6 and Figure 7.

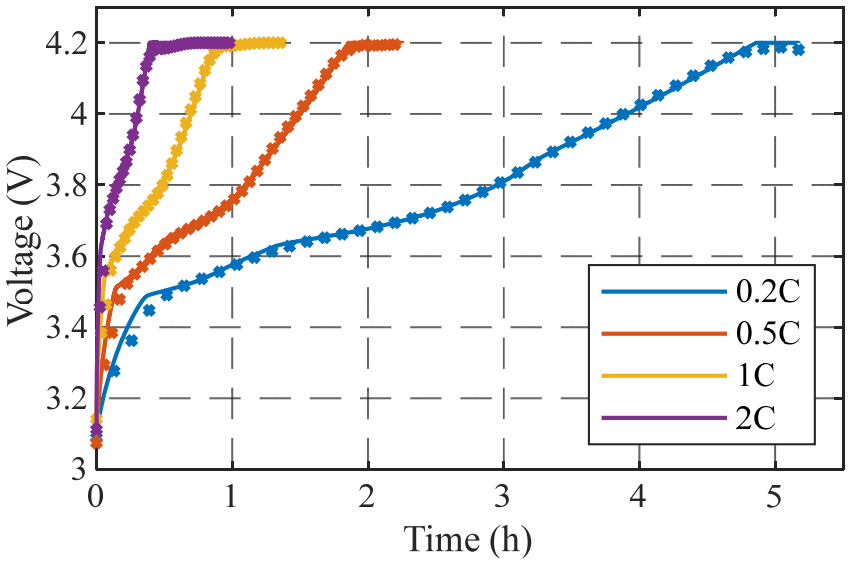

Figure 6. Voltage comparisons between experiment and simulation of CC charging. Solid lines and markers indicate the experimentally obgained and simulated terminal voltage, respectively.

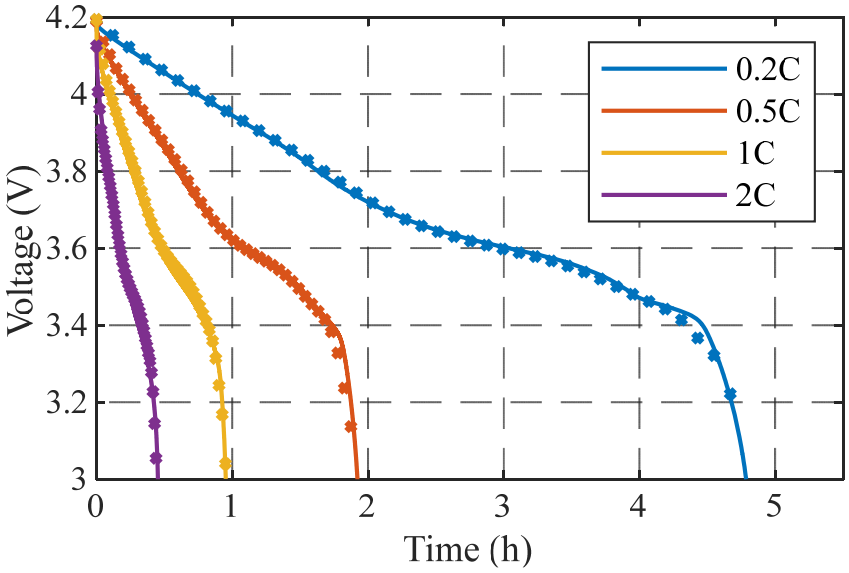

Figure 7. Voltage comparisons between experiment and simulation of CC-CV discharging. Solid lines and markers indicate the experimentally obtained and simulated terminal voltage, respectively.

In addition, two multiple-cycle tests have been conducted. The first test consists of 40 cycles of 2C CC charge and discharge. Figure 8 shows comparisons of terminal voltages over time at every ten cycles, which shows excellent agreement. The second test uses a current profile obtained from an electric vehicle driving cycle as shown in Figure 9. A comparison of corresponding terminal voltages and its absolute error are plotted in Figure 10**Error! Reference source not found.**, where the error remains within 12mV.

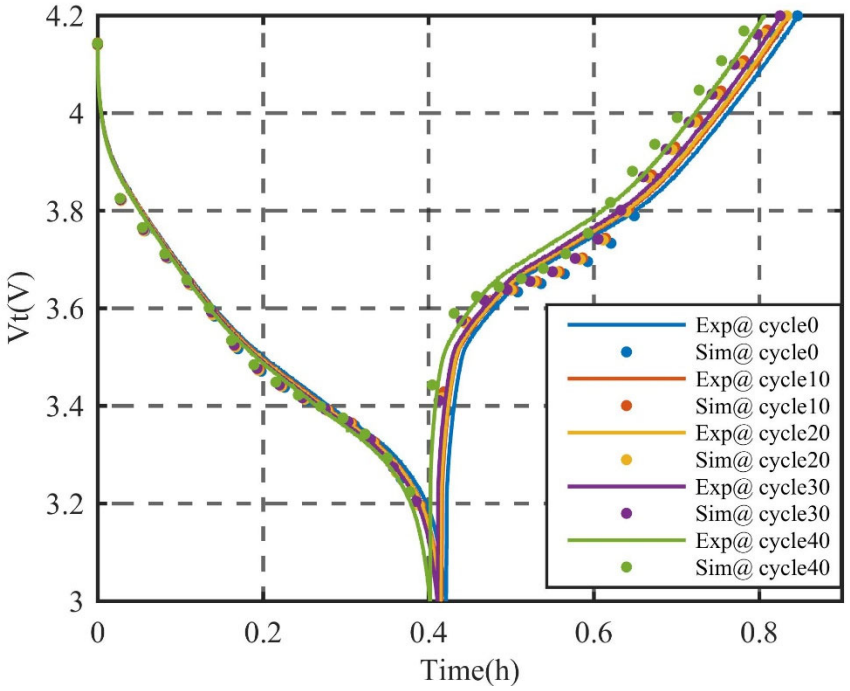

Figure 8. Comparisons of terminal voltages for every ten cycles.

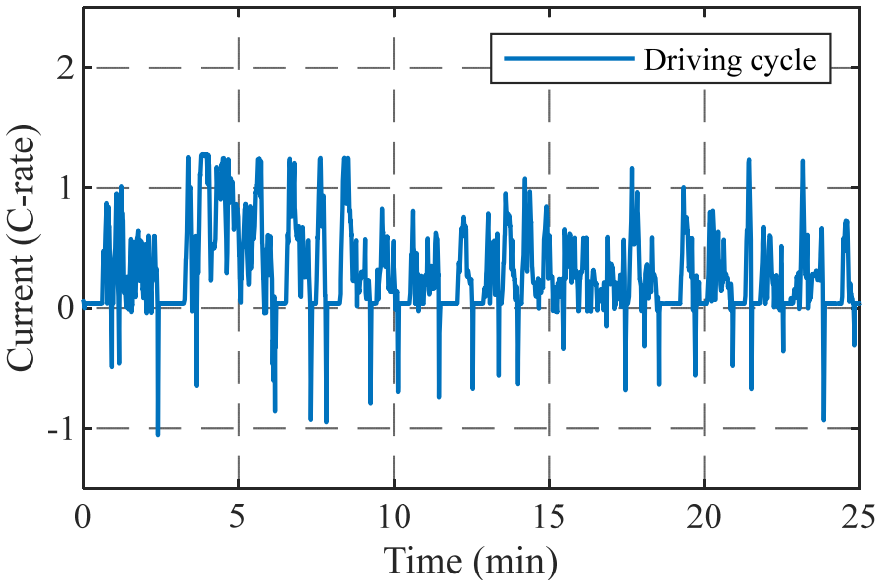

Figure 9. Current profile of a driving cycle.

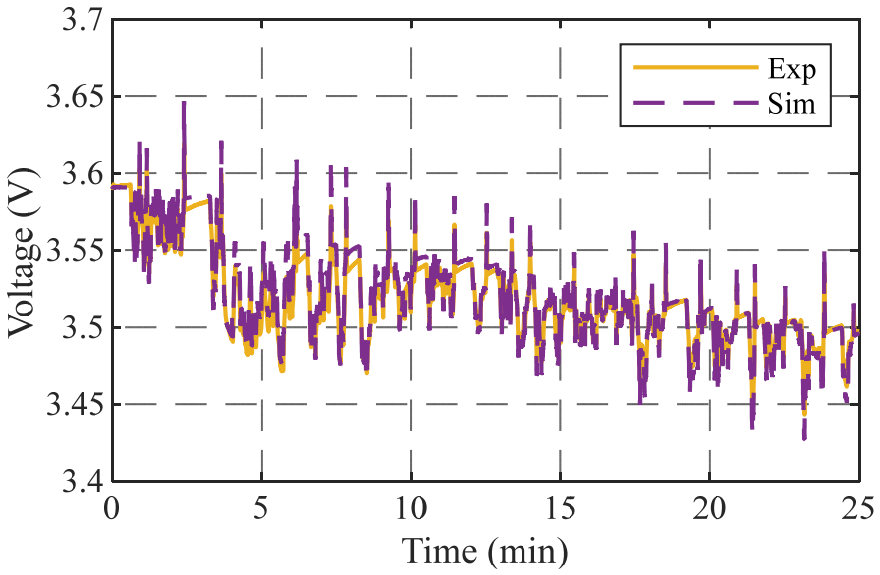

Figure 10. A comparison of terminal voltages of a driving cycle.

2.5 Summary

In this section, we present an automatic parameter estimation procedure that estimates BOL parameters of the ROM. The procedure consists of grouping, sensitivity analyses and optimization of the parameters. We estimate three sensitive parameters from the ROM including the solid phase diffusion coefficients of the positive and negative electrodes, and the film resistance. The parameters are estimated from charge and discharge experimental data at C/5, C/2, 1C, and 2C. Then, a genetic algorithm is employed as an optimization method that considers a multi-objective function. Finally, the ROM with the optimized parameters is validated against experimental data obtained from a multiple-cycle and a driving cycle test. The results show a great agreement with the experimental data up to forty cycles. The overall voltage errors remain within 12 mV.

Chapter 3. Online internal state and SOC estimation

3.1 Literature review

SOC represents the remaining capacity of a battery that can be released. It plays a crucial role in ensuring a safe and reliable battery operation by preventing under- or over-charge, and predicting available power and energy because of its close relationship to the lithium ion concentration, which is one of the core physical states of a lithium-ion battery. However, SOC cannot be directly measured. Many attempts have been made to find the best approach that enables an accurate estimation of SOC, and one of the most widely used methods is based on an equivalent circuit model (ECM) that uses electrical components–resistors, capacitors, and voltage sources–to mimic battery dynamics [16]. Then, parameters of the ECMs, as well as the SOC, are simultaneously updated by an estimator. However, the parameters of the ECMs do not provide physical information of the battery, such as ion concentrations, potentials, overpotentials, and current density, to name a few. The accurate estimation of such variables provides various benefits, such as the detection of ion concentration depletion/saturation [17], degradation prediction that considers side reactions and lithium deposition reactions [18,19], and the optimization of ultra-fast charging protocols that considers concentration and potential limitations [20].

In fact, electrochemical models account for the transport of lithium ions, electrochemical kinetics, and material properties [21], which are ideal for the above-mentioned applications since they offer the advantages of providing information regarding internal physical variables, in addition to accurately predicting terminal voltage. The governing equations of the models are a set of coupled nonlinear partial differential equations (PDEs), and solving these equations demands considerable computational power. In order to use the electrochemical model in a real-time application while retaining its physical insights, the model order should be reduced, which results

in a reduced-order model (ROM). The order reduction is performed by employing Padé approximation and residual grouping to simplify the equations of ion concentrations in both electrodes and electrolytes in conjunction with an analytical solution of cell potentials [7].

The estimator also plays a key role in accurately predicting the SOC. Despite the fact that the accuracy of a ROM can be improved by optimizing its parameters, there are still errors caused by model inaccuracy, uncertainties in initial conditions of the states in the model, and process and measurement noise. Therefore, to further reduce these errors, the nonlinear Kalman-based estimators are the potential candidates for the following reasons:

- The feedback loop can minimize the differences between predicted and measured terminal voltages so that uncertainties in the model and initial conditions are compensated.

- Recursive methods do not require the storage of all the past data but only the results of the last recursion. They are particularly suitable for estimating SOC online since the algorithm is usually embedded in a microprocessor with limited memory.

- Statistical methods are used to suppress unknown inputs (i.e., process noise) and uncertainties in the output (i.e., measurement noise). In particular, the process and measurement noises are assumed to be Gaussian distributed random variables. Although this assumption rarely holds true in practice, results reported in the research literature [16] and our results demonstrate that the method works well.

- Simple implementation with only several lines of code is even more suitable for a real-time application, such as SOC estimation, which is implemented in an onboard battery management system (BMS).

There are different types of nonlinear Kalman filters (KFs). One of the most widely used KFs is called the extended Kalman filter (EKF), which is based on the probability theory and a least-square minimization framework. The nonlinearity of a system is linearized by employing a first-order Taylor series expansion at each operating point to calculate the mean and covariance of the states. However, for a highly nonlinear system, such as an electrochemical model, the actual mean and covariance of the states may differ from the linearized results, which causes errors, and even divergence, in estimations. To overcome the drawbacks of the EKF, another nonlinear KF, an SPKF, takes a set of sample points and propagates them through the nonlinear system, from which the mean and covariance are calculated. The set of sample points, called the sigma points, is formed by calculating the matrix square-root of the state covariance. The SPKF performs better on a highly nonlinear system, such as the ROM, but the calculation of matrix square-root becomes one of the most costly operations. To further improve the computational efficiency of the SPKF, a square-root sigma-point Kalman filter (SR-SPKF) was developed [22] that propagates the square-root of covariance directly.

Some recent studies have focused specifically on utilizing an EKF with a ROM. For example, Santhanagopalan et al. applied an EKF to a ROM that simplifies a porous electrode into a single spherical particle and ignores the gradients of concentration and potential in the electrolyte [1], where the average concentration in the solid is used as the state for calculating the cell SOC. However, only the results for the anode were presented. A “three-sigma” error bound is used that indicates where the true state should remain 99% of the time. However, the results showed that the actual error was outside the error bounds 30% of the time, which implies that the error bounds provided by the EKF were not reliable. Domenico et al. applied an EKF to a ROM by averaging the input current as the cell kinetic current density [23]. The cell SOC and surface concentrations

were estimated and compared with a full-order model. However, neither of these studies addressed the problem of initial SOC offset, and the SOC errors were primarily determined by the accuracy of the time update using the model. Therefore, it is difficult to evaluate the performance of the model and estimator separately. Similarly, Stetzel et al. estimated the SOC and internal variables, including ion concentrations, cell potentials, and current density, using an EKF in conjunction with a one-dimensional ROM and provided the bounds for errors [24]. Despite their detailed analysis of each state, the used simulation profile used was only a driving condition of approximately 60% SOC.

Alternatively, despite the fact that the SPKF was reported more suitable for nonlinear systems [25,26], it has not been fully explored with the ROMs. For example, the authors in Ref. [1] implemented the SPKF with few details. On the other hand, recent studies have focused more on using the SPKF in conjunction with the ECMs. Particularly, the authors in Ref. [27] proposed a co-estimator utilizes the recursive least square for parameter identification, the EKF for online parameter updating, and the SPKF for SOC estimation. It is reported that the RMSE of the latter was less than 2.5% with high robustness. Moreover, Yang et al. conducted a comparative study of the EKF, SPKF, and particle filter in conjunction with an empirical model where the RMSE of SOC estimation was less than 3% with computational efficiency that is comparable to the EKF [28].

In summary, most of the aforementioned studies employed the EKFs to the ROMs, while the SPKF was primarily applied to the ECM and the empirical models. We realized that there is a lack of a thorough analysis of the performance of different nonlinear KFs, other than the EKF, in conjunction with an electrochemical model. Therefore, the goal of this chapter is to answer questions including which nonlinear Kalman filter¬–among EKF, SPKF, and SR-SPKF–has the

best performance when employed to the ROM; as well as how to modify the filters to achieve higher robustness. Specifically, we chose to investigate three enhanced nonlinear KFs that include a modified EKF, SPKF, and SR-SPKF in conjunction with a developed ROM [7,29] that entails a similar computational cost to that of an ECM. We investigated how state equality constraints affect SOC estimation results and how process and measurement noise can be automatically compensated for without manually tuning of filter parameters. Performance of the nonlinear KFs was compared with respect to the accuracy, computational time, and ability to reject the initial errors, which demonstrates that an adaptive sigma-point Kalman filter outperforms others that are validated in real-time using a battery-in-the-loop (BIL) test station. This chapter provides three main contributions: (1) the proposed method incorporates additional equality constraints systematically without revisiting the structure of the original model, which addresses the problem of weak observability from the terminal voltage [23]; (2) estimation of SOC from the cathode results in a faster convergence speed when an initial offset of SOC is present; and (3) comparative studies as well as systematic analysis on several modified nonlinear Kalman filters are conducted to assess the best SOC estimator based on the ROM.

3.2 Design of SOC and internal state estimator

Although the performance of the ROM has been demonstrated as described, there are still errors, particularly in real-time applications. Potential sources for the errors are listed below:

- Executing the ROM in real-time requires advanced knowledge of initial states, such as the solid ion concentration and SOC. However, these initial states are usually not precisely known.
- Model uncertainties due to model simplification and unknown physics.
- Measurement errors caused by a current or voltage sensor.

Furthermore, when these errors accumulate over time, predicted states could diverge from the true states. To actively compensate for these errors, we propose an online SOC estimation algorithm based on the ROM along with an adaptive nonlinear filtering technique, which allows for accurate estimation of the states without error accumulation.

3.2.1 State and output equation

For the design of an adaptive nonlinear filter, a general discrete-time state-space form is needed as follows:

$$x_k = f\left(x_{k-1}, u_{k-1}, w_{k-1}\right), \tag{18}$$

$$y_k = g_k(x_k, u_k), \text{ and} \tag{19}$$

$$z_k = h\left(x_{k-1}, u_{k-1}, v_{k-1}\right). \tag{20}$$

Eq. (18) is called a "state equation" where x_k is the state vector of the system at any time index k. The input of the system is denoted as u_k, and w_k refers to process noise, which represents unknown disturbances that affect the state of the system. The internal variable vector, y_k in Eq. (19), is as a function of u_k and x_k, while the output of the system in Eq. (20), z_k, is a function of y_k, u_k, and v_k, where v_k represents the sensor noise that only affects measurements of the system.

Therefore, Eqs. (1) and (3) of the ROM are rewritten from the above form as

$$x_{k+1} = \mathbf{A}_k x_k + \mathbf{B}_k \left(j_k^{Li} + w_k\right), \tag{21}$$

Where $\mathbf{A} = \mathbf{A}_{cs}$ and $\mathbf{B} = \mathbf{B}_{cs}$.

Furthermore, the input of the system is the intercalation current density j^{Li}, and the process noise is modeled as being added to the input.

To estimate the solid ion concentration as well as the cell SOC, c_{sx} are chosen as the state of the filter, that is, $x = c_{sx}$. The dimension of x is determined by the reduction order of the Padé approximation that is 6×1, which is also the order of the nonlinear filter. Then the estimated internal states are calculated from Eq. (2) as

$$y_k = \begin{bmatrix} c_{s,surf} \\ c_{s,ave} \end{bmatrix} = \begin{bmatrix} \mathrm{C}_{cs,surf} \\ \mathrm{C}_{cs,ave} \end{bmatrix} x_k \,. \tag{22}$$

Finally, the terminal voltage of the cell is the output and Eq. (20) is rewritten as

$$V_k = z_k = h(y_k, j_k^{Li}) + v_k \,, \tag{23}$$

where the noise, v_k, is modeled as being added to the voltage measurement.

3.2.2 Calculation of SOC

The estimated internal state, $c_{s,ave}$, is then used to calculate the SOC of a cell. SOC is defined as the ratio of releasable capacity ($Q_{releasable}$) to the maximum capacity (Q_{max}):

$$\mathrm{SOC} = \frac{Q_{releasable}}{Q_{\max}} \cdot 100\% \,. \tag{24}$$

The total number of cyclable charges should be governed by the charge conservation. Therefore, $Q_{releasable}$ is the difference between the numbers of charges residing in the electrode and those at the lowest stoichiometric number of that electrode, which can be either the anode or the cathode:

$$Q_{releasable} = \int_0^{\delta_{neg}} \left[\varepsilon_{s,neg} \cdot F \cdot c_{s,ave,neg} \cdot A - \varepsilon_{s,neg} \cdot F \cdot c_{s,\max,neg} \cdot A \cdot x_0 \right] dx \text{ ; or,} \tag{25}$$

$$Q_{releasable} = \int_{\delta_{neg}+\delta_{sep}}^{\delta_{neg}+\delta_{sep}+\delta_{pos}} \left[\varepsilon_{s,pos} \cdot F \cdot c_{s,ave,pos} \cdot A - \varepsilon_{s,pos} \cdot F \cdot c_{s,\max,pos} \cdot A \cdot y_{100} \right] dx \,, \tag{26}$$

where δ is the electrode thickness, subscript *neg*, *sep*, and *pos* denotes the negative electrode, separator, and the positive electrode, respectively, while ε_s is the active material volume fraction, and F is the Faraday's constant; $c_{s,ave}$ and $c_{s,max}$ denote the volume average and maximum concentration, respectively, of the solid phase of each particle; A is the plate area, and x_0 and y_{100} is the anode and cathode stoichiometric number at 0% and 100% SOC, respectively.

Since the solid ion concentration is calculated using a single particle approximation, Eqs. (25) and (26) are rewritten as

$$Q_{releasable} = \delta_{neg} \cdot \left[\varepsilon_{s,neg} \cdot F \cdot c_{s,ave,neg} \cdot A - \varepsilon_{s,neg} \cdot F \cdot c_{s,\max,neg} \cdot A \cdot x_0 \right]; \text{ or,} \tag{27}$$

$$Q_{releasable} = \delta_{pos} \cdot \left[\varepsilon_{s,pos} \cdot F \cdot c_{s,ave,pos} \cdot A - \varepsilon_{s,pos} \cdot F \cdot c_{s,\max,pos} \cdot A \cdot y_{100} \right]. \tag{28}$$

Q_{max} is expressed as a function of the difference of charges in the composite electrode, from the highest to the lowest stoichiometric number:

$$Q_{\max} = F \cdot A \cdot \varepsilon_{s,neg} \delta_{neg} \cdot c_{s,\max,neg} (x_{100} - x_0); \text{ or,} \tag{29}$$

$$Q_{\max} = F \cdot A \cdot \varepsilon_{s,pos} \delta_{pos} c_{s,\max,pos} (y_0 - y_{100}), \tag{30}$$

where x_{100} and y_0 is the stoichiometric number at 100% SOC.

Substituting Eqs. (25) to (30) into Eq. (24) results in

$$SOC = \frac{c_{s,ave,neg} - c_{s,\max,neg} \cdot x_0}{c_{s,\max,neg} \left(x_{100} - x_0 \right)} \cdot 100\% = \frac{c_{s,ave,pos} - c_{s,\max,pos} \cdot y_{100}}{c_{s,\max,pos} \left(y_0 - y_{100} \right)} \cdot 100\% . \tag{31}$$

Therefore, SOC is calculated as a ratio of the average ion concentration to the maximum ion concentration in the solid of either the composite anode or the cathode. The only variable of the equation is $c_{s,ave}$, which is calculated from Eq. (22).

3.2.3 Nonlinear filtering

On the one hand, we have known that noise is present both in the state equation and the output equation, which we denoted as w_k and v_k. Reasonably, these uncertainties can be further assumed to have Gaussian distribution according to the central limit theorem. Because of these noises, estimation of cell state becomes a sequential probabilistic inference problem, whose propose is estimating unmeasurable states based on a model using only information of input and noisy output. This makes the Kalman filter based methods are perfect candidates for such a problem. On the other hand, Eq. (7) and (11) of the ROM show severe nonlinearities. Therefore, the nonlinear KFs can be used to estimate states of systems that are nonlinear and stochastic. They are also recursive, so the states can be predicted in real-time. The EKFs and SPKFs are two types of filters that reduce errors caused by model inaccuracy, sensor noises as well as any initial state errors.

3.2.3.1 EKF

EKF linearizes a nonlinear system by a first-order Taylor series expansion at each time step. In the first step, a time update is performed to compute the present state from the prior information in conjunction with the system model. Then, a measurement update is performed that uses present measurements to further compensate for corruption in the predicted state caused by the noise in the system. The details are illustrated as follows.

Time update (1). Firstly, the expectation of state is calculated based on the system model and stored information from the previous time step:

$$\hat{x}_k^- = E\left[f\left(x_{k-1}, u_{k-1}, w_{k-1}\right)\right] = f\left(\hat{x}_{k-1}^+, u_{k-1}, w_{k-1}\right) \tag{32}$$

where $\hat{x}$ indicates an estimated value that is different from the actual state *x*. A superscript "-" denotes a prediction based on past data, while a superscript "-" denotes an estimation based on not only the past data but also the measurements taken at the current time. $E[\cdot]$ is the statistical expectation operator.

Time update (2). Then, error covariance *P* is calculated as

$$\mathbf{P}_k^- = E\left[\left(x_k - \hat{x}_k^-\right)\left(x_k - \hat{x}_k^-\right)^T\right] \approx \mathbf{A}_{k-1}\mathbf{P}_{k-1}^+\mathbf{A}_{k-1}^T + \mathbf{B}_{k-1}\mathbf{Q}_{k-1}\mathbf{B}_{k-1}^T \tag{33}$$

where A_{k-1} and B_{k-1} are the first order Taylor-series expansion of state function *f* with respect to x_{k-1} and w_{k-1}. That is,

$$\mathbf{A}_{k-1} = \left.\frac{\partial f\left(x_{k-1}, u_{k-1}, w_{k-1}\right)}{\partial x_{k-1}}\right|_{x_{k-1}=\hat{x}_{k-1}^+} \tag{34}$$

$$\mathbf{B}_{k-1} = \left.\frac{\partial f\left(x_{k-1}, u_{k-1}, w_{k-1}\right)}{\partial w_{k-1}}\right|_{w_{k-1}=\overline{w}_{k-1}} \tag{35}$$

Time update (3). Finally, the output z_k is predicted that is based on the output equation

$$\hat{z}_k = E\left[h\left(x_{k-1}, u_{k-1}, v_{k-1}\right)\right] = h\left(\hat{x}_{k-1}^+, u_{k-1}, v_{k-1}\right) \tag{36}$$

Measurement update (1). The estimator gain is calculated as

$$\mathbf{L}_k = E\left[\left(x_k - \hat{x}_k^-\right)\left(z_k - \hat{z}_k\right)^T\right] E\left[\left(z_k - \hat{z}_k\right)\right]^{-1} = \mathbf{P}_k^-\mathbf{C}_k^T\left[\mathbf{C}_k\mathbf{P}_k^-\mathbf{C}_k + \mathbf{D}_k\mathbf{R}_k\mathbf{D}_k^T\right]^{-1} \tag{37}$$

where C_k and D_k are calculated by performing Taylor series expansion on the output equation as

$$\mathbf{C}_k = \left.\frac{\partial h(x_k, u_k, v_k)}{\partial x_k}\right|_{x_k = \hat{x}_k^-} \tag{38}$$

$$\mathbf{D}_k = \left.\frac{\partial h(x_k, u_k, v_k)}{\partial v_k}\right|_{v_k = \bar{v}_k} \tag{39}$$

Measurement update (2). Then x_k is updated using L_k,

$$\hat{x}_k^+ = \hat{x}_k^- + \mathbf{L}_k\left(z_k - \hat{z}_k\right) \tag{40}$$

Measurement update (3). Finally, the error covariance matrix is updated as

$$\mathbf{P}_k^+ = \mathbf{P}_k^- - \mathbf{L}_k\mathbf{C}_k\mathbf{P}_k^- \tag{41}$$

This completes one recursive iteration of the EKF. This is by far the most widely used nonlinear filtering method. However, one of the drawbacks of the EKF lies in the linearization approach to calculating the mean and covariance, in which they undergo a nonlinear transformation. For a highly nonlinear system, the linearized mean and covariance may not represent the true distribution of the output [25].

3.2.3.2 SPKF

The SPKF addresses the aforementioned problems by taking a minimal set of sample points and propagating them through the nonlinear system, from which the mean and covariance are calculated. A minimal number of sigma points are chosen according to the dimension of the system.

To apply the SPKF to the ROM, the same state-space formulation used by the EKF is used as shown in Eqs. (18) to (20). An augmented state is constructed, which is comprised of the original state vector, process noise w_k, and measurement noise v_k:

$$x_k^a = \left[x_k^T, w_k^T, v_k^T \right]^T \tag{42}$$

where superscript *a* denotes an augmented state.

The corresponding sigma points are then calculated as follows:

$$\mathcal{X} = \left\{ \bar{x}, \bar{x} + h\sqrt{\mathbf{P}}, \bar{x} - h\sqrt{\mathbf{P}} \right\}. \tag{43}$$

where $\bar{x}$ indicates the mean of the system state, and *h* is a scaling factor that determines how far the sigma points are spread out from the mean.

Scaling factor *h* is also related to a set of weights that is used to recover the true state from the sigma points. A central difference Kalman filter (CDKF) scheme [30] is used that allows fewer tuning parameters to be used compared with other SPKF forms. The weights are defined as follows:

$$\alpha_0^{(m)} = \alpha_0^{(c)} = \frac{h^2 - \dim\left(x_k^a\right)}{h^2} \quad \text{and} \tag{44}$$

$$\alpha_i^{(m)} = \alpha_i^{(c)} = \frac{1}{2h^2}, \tag{45}$$

where the superscripts *m* and *c* represent the weights on the states and covariance, respectively, and for Gaussian random noises, $h = \sqrt{3}$.

For each iteration, the estimation process of SPKF is similar to that of the EKF but different in detail as described below.

Time update (1). Firstly, a set of sigma points is chosen so that the mean and covariance of the points match the estimated mean $x_{k-1}^{a,+}$, and covariance $P_{x,k-1}^{a,+}$ at the previous time step, *k-1*,

$$\mathcal{X}_{k-1}^{a,+} = \left\{ \hat{x}_{k-1}^{a,+}, \hat{x}_{k-1}^{a,+} + h\sqrt{\mathbf{P}_{x,k-1}^{a,+}}, \hat{x}_{k-1}^{a,+} - h\sqrt{\mathbf{P}_{x,k-1}^{a,+}} \right\}. \tag{46}$$

The nonlinear state function is then evaluated as

$$\mathcal{X}_{k,i}^{x,-} = f\left(X_{k-1,i}^{x,+}, u_{k-1}, X_{k-1,i}^{w,+} \right). \tag{47}$$

Finally, the state prediction is computed as a weighted sum of $p+1 = 2 \times \dim\left(x_k^a\right) + 1$ sigma points:

$$\hat{x}_k^- = \sum_{i=0}^{p} \alpha_i^{(m)} \mathcal{X}_{k,i}^{x,-}. \tag{48}$$

Time update (2). Using the sigma points computed from Eq. (46). The error covariance is computed as

$$\mathbf{P}_{x,k}^- = \sum_{i=0}^{p} \alpha_i^{(c)} \left(\mathcal{X}_{k,i}^{x,-} - \hat{x}_k^- \right)\left(\mathcal{X}_{k,i}^{x,-} - \hat{x}_k^- \right)^T. \tag{49}$$

Time update (3). Next, we compute a set of transformed sigma points by evaluating the output equation using $\mathcal{X}$

$$\mathcal{Z}_{k,i} = h\left(\mathcal{X}_{k-1,i}^{x,+}, u_{k-1}, \mathcal{X}_{k-1,i}^{v,+} \right). \tag{50}$$

Then, the system output is estimated as

$$\hat{z}_k = \sum_{i=0}^{p} \alpha_i^{(m)} \mathcal{Z}_{k,i}. \tag{51}$$

Measurement update (1). This step is to compute the estimator gain using covariance matrices:

$$\mathbf{P}_{z,k} = \sum_{i=0}^{p} \alpha_i^{(c)} \left(\mathcal{Z}_{k,i} - \hat{z}_k^- \right)\left(\mathcal{Z}_{k,i} - \hat{z}_k \right)^T \text{ and} \tag{52}$$

$$\mathbf{P}_{xz,k}^{-} = \sum_{i=0}^{p} \alpha_i^{(c)} \left(\mathcal{X}_{k,i}^{x,-} - \hat{x}_k^{-} \right) \left(\mathcal{Z}_{k,i} - \hat{z}_k \right)^T . \tag{53}$$

Then, we compute

$$\mathbf{L}_k = \mathbf{P}_{xz,k}^{-} \left(\mathbf{P}_{z,k} \right)^{-1} . \tag{54}$$

Measurement update (2). This step updates the predicted state, which is the same as shown in Eq. (40).

Measurement update (3). The final step updates the error covariance, which is the same as in Eq. (41).

3.2.3.3 SR-SPKF

Although an SPKF can accurately capture the distribution of the output of a nonlinear system, one of its drawbacks is a high computational complexity due to the matrix square root calculation when updating a new set of sigma points at each time step. Computational efficiency can be improved by a square-root form [22] that updates the state covariance in a Cholesky-factored form. This method involves using three linear algebra techniques [22,26];

• *QR decomposition*. The QR decomposition factors a matrix into an orthogonal matrix, Q, and an upper triangular matrix, R, that can be used to compute the Cholesky factor of covariance in Eqs. (43), (46) and (47). This process is denoted as qr{.}.

• *Cholesky factor update.* Cholesky factor update solves the square-root when a matrix is negative definite, which is denoted as cholupdate{.}. It is useful when the weights of the sigma-points are negative.

• *Efficient least squares.* This method solves the least square problem $xA=B$ efficiently using back-substitution, that is, $x=B/A$. Specifically, the estimator gain is solved from $\mathbf{L}_k\left(\mathbf{S}_{z,k}\mathbf{S}_{z,k}^T\right)=\mathbf{P}_{xz,k}^-$, which is computed via efficient least-squares twice: first, find $x=\mathbf{P}_{xz,k}^-/\mathbf{S}_{z,k}^T$, and then solve $\mathbf{L}_k=x/\mathbf{S}_{z,k}$.

Implementing an SR-SPKF is similar to that of an SPKF, except that the error covariance update is replaced with an update of a new square-root form. The SR-SPKF used in this study is summarized in Table 5.

Table 5. The SR-SPKF algorithm.

Nonlinear state and output equations	Eqs. (18) to (20)
Definition of the augmented states and the sigma points	Eqs. (42) and (46)
Initialization	$\hat{x}_0^+, \mathrm{P}_0^+$
Time update	***(1) State prediction:*** Eqs. (47) and (48). ***(2) Error covariance prediction:*** $\mathbf{S}_{x,k}^- = qr\left\{\left[\sqrt{\alpha_1^{(c)}}\left(\mathcal{X}_{1:p,k}-\hat{x}_k\right) \quad \sqrt{\mathbf{Q}}\right]\right\}$ $\mathbf{S}_{x,k}^- = cholupdate\left\{\mathbf{S}_{x,k}^-, \mathcal{X}_{0,k}-\hat{x}_k^-, \alpha_0^{(c)}\right\}$ ***(3) Output estimation:*** Eqs. (50) and (51).
Measurement update	***(1) Estimator gain:*** $\mathbf{S}_{y,k} = qr\left\{\left[\sqrt{\alpha_1^{(c)}}\left(\mathcal{Z}_{1:p,k}-\hat{z}_k\right) \quad \sqrt{\mathbf{R}}\right]\right\}$ $\mathbf{S}_{y,k} = cholupdate\left\{\mathbf{S}_{y,k}, \mathcal{Z}_{0,k}-\hat{z}_k, \alpha_0^{(c)}\right\}$ $\mathbf{P}_{xz,k}^- = \sum_{i=0}^{p}\alpha_i^{(c)}\left(\mathcal{X}_{k,i}^{x,-}-\hat{x}_k^-\right)\left(\mathcal{Z}_{k,i}-\hat{z}_k\right)^T$

	$\mathbf{L}_k = \left(\mathbf{P}^{-}_{xz,k} / \mathbf{S}^{T}_{z,k}\right) / \mathbf{S}_{z,k}$ ***(2) State correction:*** Eq. (40). ***(3) Error covariance correction:*** $\mathbf{S}^{+}_{x,k} = cholupdate\left\{\mathbf{S}^{-}_{x,k}, \mathbf{L}_k \mathbf{S}_{z,k}, -1\right\}$

3.2.4 State equality constraints

When a nonlinear filter is employed in the ROM, the voltage errors may be overcompensated. As plotted in Figure 11, the potential of the cathode is higher than that of the anode; hence, any potential changes in the cathode will affect the terminal voltage error more than that of the anode. As a result, the estimated SOC does not correspond to the actual SOC. As an example, which is shown in Figure 12, under the assumption of a 20% initial SOC error, the estimation of the cathode converges to values that are higher than the actual SOC, while the estimation of the anode remains biased by the initial error.

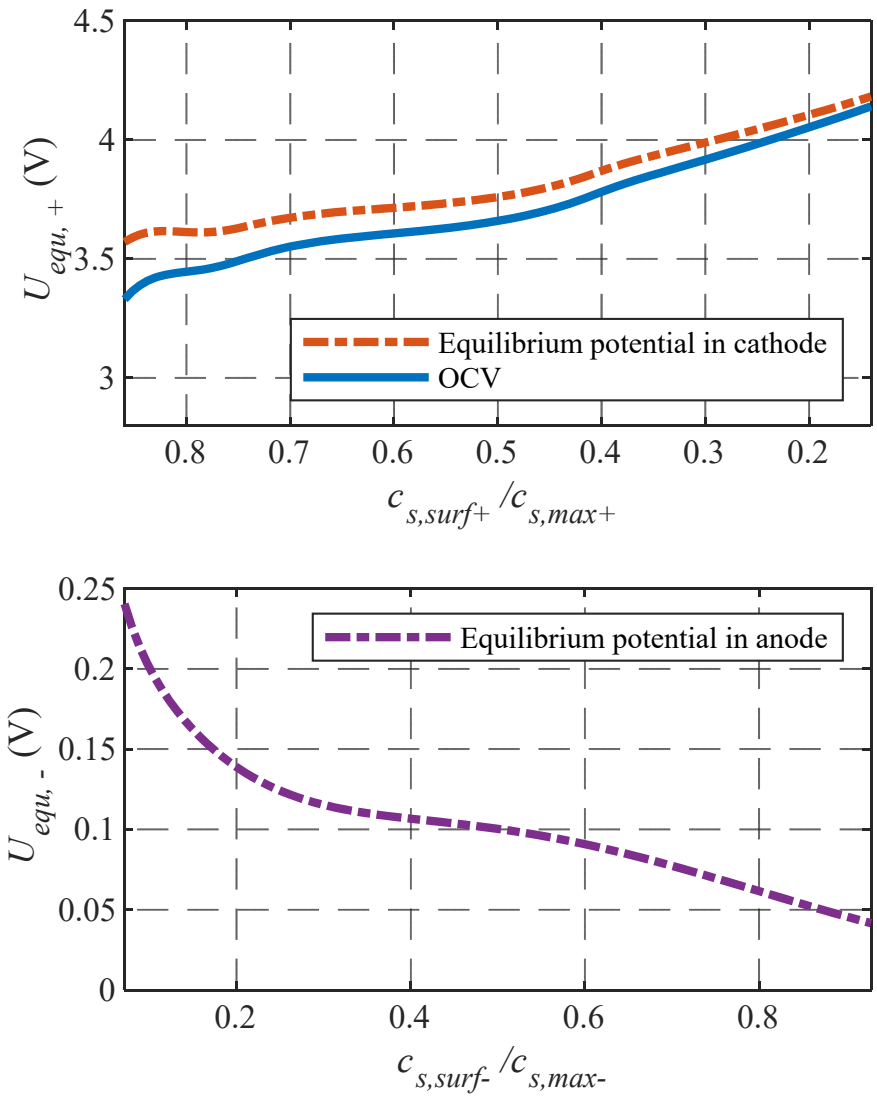

Figure 11. Open circuit voltage and equilibrium potentials of both electrodes.

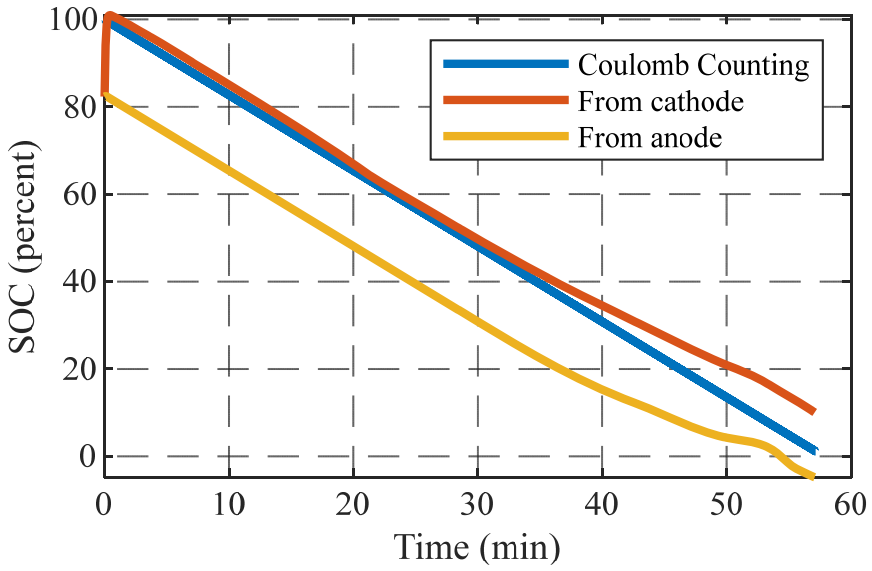

Figure 12. SOC estimation without adding equality state constraints.

In fact, the number of charges transferred from one electrode is equal to that left from the other electrode during operations when there is no ion loss, as shown in Eq. (31). However, this charge conservation as an equality constraint is not incorporated into the state equation. To solve this problem, the constraint is incorporated as follows.

Firstly, we rewrite Eq. (31) as

$$\begin{bmatrix} \dfrac{1}{c_{s,\max,neg}\left(x_{100}-x_0\right)} & \dfrac{1}{c_{s,\max,pos}\left(y_0-y_{100}\right)} \end{bmatrix} \begin{bmatrix} c_{s,ave,neg} \\ c_{s,ave,pos} \end{bmatrix} = \frac{x_0}{x_{100}-x_0} - \frac{y_{100}}{y_0-y_{100}}, \tag{55}$$

where $c_{s,ave} = \begin{bmatrix} c_{s,ave,neg} & c_{s,ave,pos} \end{bmatrix}^T$ is one of the internal variables computed from Eq. (22), that is,

$$c_{s,ave} = \mathrm{C}_{cs,ave} x_k . \tag{56}$$

Combining Eqs. (55) and (56) results in

$$D_{eq} x_k = d_k , \tag{57}$$

where $D_{eq} = \left[\frac{1}{c_{s,\max,neg}\left(x_{100} - x_0\right)} \quad \frac{1}{c_{s,\max,pos}\left(y_0 - y_{100}\right)} \right] \mathrm{C}_{cs,ave}$, and $d_k = \frac{x_0}{x_{100} - x_0} - \frac{y_{100}}{y_0 - y_{100}}$.

The goal is to minimize the mean square error subject to the state equality constraints, that is,

$$\min_{\tilde{x}} E\left[\left(x - \tilde{x}\right)^T \left(x - \tilde{x}\right)\right] \text{ such that } D_{eq} x = d \,, \tag{58}$$

where $\tilde{x}$ indicates an updated state estimation after incorporating the constraint: $E\left[\left(x - \tilde{x}\right)^T \left(x - \tilde{x}\right)\right] = \hat{x}^T \hat{x} - 2\tilde{x}^T \hat{x} + \tilde{x}^T \tilde{x}$, and $\hat{x} = E\left[x\right]$.

Therefore, the cost function can be rewritten as

$$J_L = E\left[\left(x - \tilde{x}\right)^T \left(x - \tilde{x}\right)\right] + 2\lambda^T \left(D_{eq} x - d\right). \tag{59}$$

where λ is the Lagrange multiplier.

To find a minimum of the function, its first order derivatives are taken, which results in

$$\frac{\partial J_L}{\partial \tilde{x}} = 0, \text{and} \frac{\partial J_L}{\partial \lambda} = 0 \,, \tag{60}$$

Finally, the solution is

$$\tilde{x} = \hat{x} - D_{eq}^T (D_{eq} D_{eq}^T)(D_{eq} \hat{x} - d) \,, \tag{61}$$

which is integrated after the *measurement update (2)*.

The results of SOC estimation with the incorporated equality constraint are shown in Figure 13, where the SOC of both electrodes were consistent with the experimental result after convergence. Additionally, it took 45 seconds for the cathode SOC to converge, which is 87% faster than that of the anode (345 seconds), because the cathode equilibrium potential has a larger

magnitude. Therefore, the SOC calculated from the cathode, rather than the anode, is used for further SOC estimation because of its fast convergence speed.

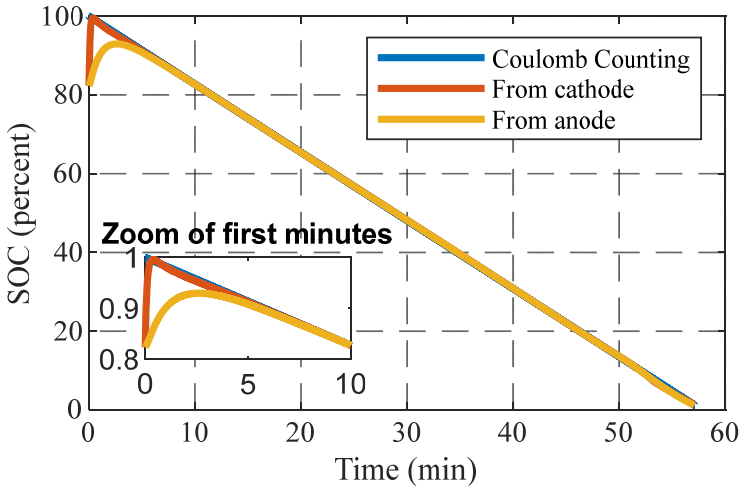

Figure 13. SOC estimation after adding equality state constraints.

3.2.5 Adaptive noise covariance matrices

As previously mentioned, process and measurement noise are assumed to be normally distributed random variables. In fact, it is also required that the distribution has a zero mean. Therefore, the process and measurement noise can be expressed as

$$w \sim \mathcal{N}(0, \mathbf{Q}) \text{ and } v \sim \mathcal{N}(0, \mathbf{R}),$$

where **Q** and **R** are the covariance matrices of w and v, respectively.

Usually, the noise covariance matrices are constant parameters determined offline before the estimation process begins. In practice, the characteristics of noises vary depending on the choice of sensors and the operating conditions. Hence, the previously found noise covariance matrices do not work optimally, but they can be improved by a covariance-matching technique. The method

estimates **Q** and **R** adaptively by making the covariance computed from the output error consistent with their theoretical values, that is,

$$\mathbf{C}\left(\mathbf{APA}^T+\mathbf{Q}\right)\mathbf{C}^T+\mathbf{R}=E\left[r_k r_k^T\right] \tag{62}$$

where $r=z-\hat{z}$ is the residual. We can also compute the covariance $E\left[r_k r_k^T\right]$ as

$$E\left[r_k r_k^T\right]=\frac{1}{m}\sum_{i=i_0}^{m+i_0} r_i r_i^T \tag{63}$$

where *m* is an empirically selected moving window that determines the amount of data considered, and i_0 indicates the first element of the estimation window.

Therefore, when **R** is determined, **Q** can be updated as follows:

$$\hat{\mathbf{Q}}_k=\mathbf{C}_k^{-1}\left(E\left[r_k r_k^T\right]-\mathbf{C}_k\mathbf{A}_k\mathbf{P}_k^{+}\mathbf{A}_k^T\mathbf{C}_k^T-\mathbf{R}_k\right)\left(\mathbf{C}_k^T\right)^{-1}. \tag{64}$$

For the EKF, when Q is known, then R is updated as,

$$\hat{\mathbf{R}}_k=\frac{1}{m}\sum_{j=1}^{m} r_{i-j} r_{i-j}^T-\mathbf{C}_k\mathbf{P}_k^{-}\mathbf{C}_k^T. \tag{65}$$

Similarly for the SPKF and SR-SPKF [31],

$$\hat{\mathbf{R}}_k=\frac{1}{m}\sum_{j=1}^{m} r_{i-j} r_{i-j}^T-\sum_{i=0}^{p}\alpha_i^{(c)}\left(\mathcal{Z}_{k,i}-\hat{z}_k^{-}\right)\left(\mathcal{Z}_{k,i}-\hat{z}_k\right)^T. \tag{66}$$

To analyze the performance of the proposed method, noise is added to the input and the output equations. Comparison of terminal voltage is plotted in Figure 14(a). The blue, red, and yellow lines show the noisy, actual, and simulated voltage, respectively. The simulation shows a good match with the actual voltage, and the voltage error quickly converges to within 15 mV while

the residual varies between ± 200 mV as shown in Figure 14(b). Additionally, although the magnitude of the noises changed after 18 and 36 minutes, respectively, the simulated terminal voltage was not affected since the covariances are adjusted adaptively. Figure 14(c) shows the results of the SOC estimation, which match well with the experimental results. After convergence from an 18% initial error, the SOC error is kept within 2%. Overall, since the covariance was changed adaptively, the predicted terminal voltage, as well as the estimated SOC, were not affected. Likewise, the adaptive method was applied to the SPKF and SR-SPKF, which are referred to as ASPKF and ASR-SPKF, and finally, their performance is compared.

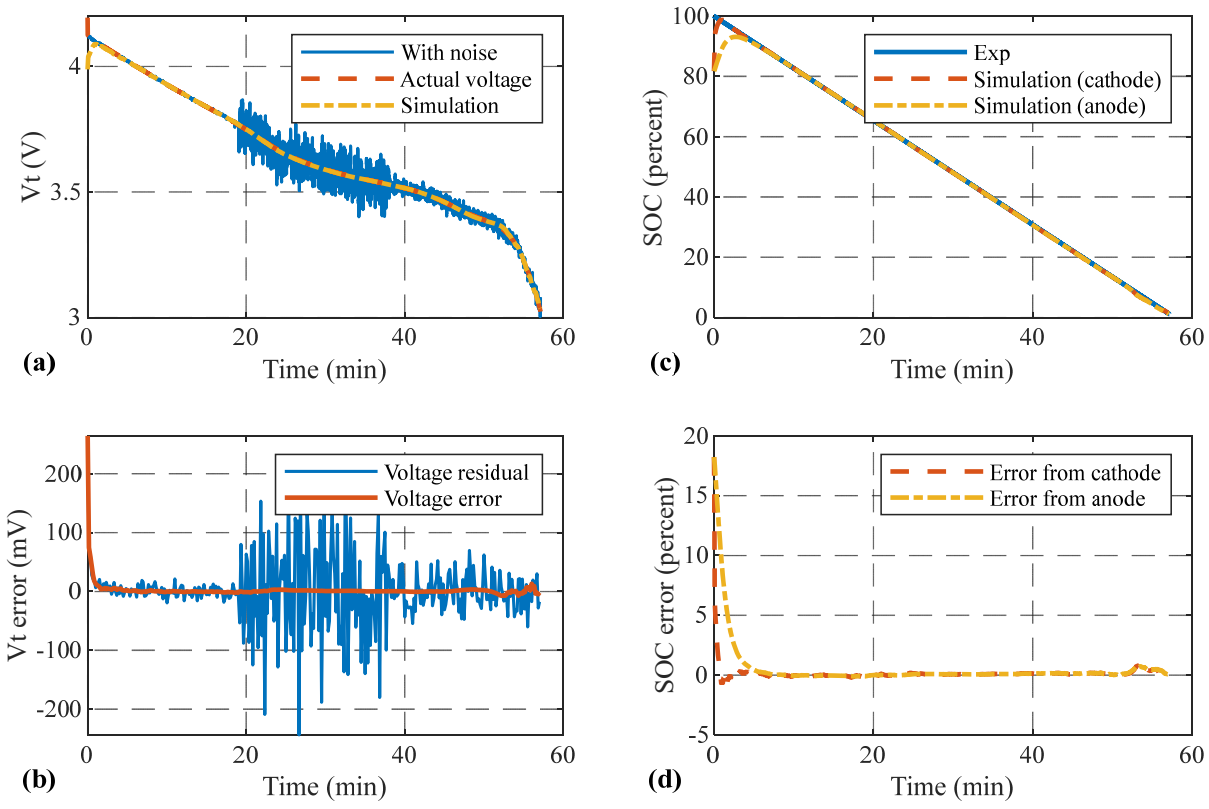

Figure 14. Performance of the adaptive algorithm. (a) Terminal voltage; (b) voltage error and residual; (c) estimated SOC; (d) SOC error.

3.3 Result and discussion

3.3.1 SOC errors and error bounds

The absolute SOC estimation error and predicted error bounds for the hybrid pulse power characteristic (HPPC) test using the AEKF are shown in Figure 15(a), where the initial SOC value was correctly initialized to 100%. The solid blue and gray lines show the absolute error and error bounds, respectively. The absolute error is defined as the difference between the experimentally calculated SOC and the estimated SOC, which was less than 5%, of which one of the dominant sources is due to the Taylor series approximation of the nonlinearity in the voltage equation. Moreover, the error bound was unable to encompass the true errors 35% of the time. In Figure 15(b) and (c), the results are plotted for the ASPKF and ASR-SPKF, respectively, which are nearly the same since the mathematical treatments for deriving the square-root form only affect computational efficiency. Additionally, the RMSEs and the maximum SOC errors of ASPKF and ASR-SPKF were 1.68% and 3.1%, respectively, as listed in Table 6. Improvements against the AEKF were 35% and 45%, respectively. Furthermore, the error bounds are correctly included the calculated error 100% of the time.

In real-time applications, initial states might be different from actual states, when the prior state of a battery is unknown. To mimic such cases, an offset was added to the estimated SOC. The results of the HPPC test are shown in Figure 15(d) to (f). Although the AEKF, ASPKF, and ASR-SPKF had the same initial error covariance matrices, it took the AEKF 18 minutes to recover from the initial state, while the ASPKF and ASR-SPKF took less than five minutes, which was a 72% improvement. After convergence, the error of the AEKF remained less than 6%, which was 50% greater than of the other two filters. Similar to the previous case, the SOC errors of the AEKF

exceeded the bounds more than 30% of the time, while errors of the ASPKF and ASR-SPKF remained within bounds during the entire time. Additionally, the ASPKF and ASR-SPKF improved the RMSE by about 30%. Finally, for comparison, the RMSEs, maximum errors, and the convergence times are listed in Table 6. Particularly, the convergence speed of ASPKF and ASR-SPKF are 8.25 and 7.82 times faster than the results reported in Ref. [26] (~1138 s), respectively.

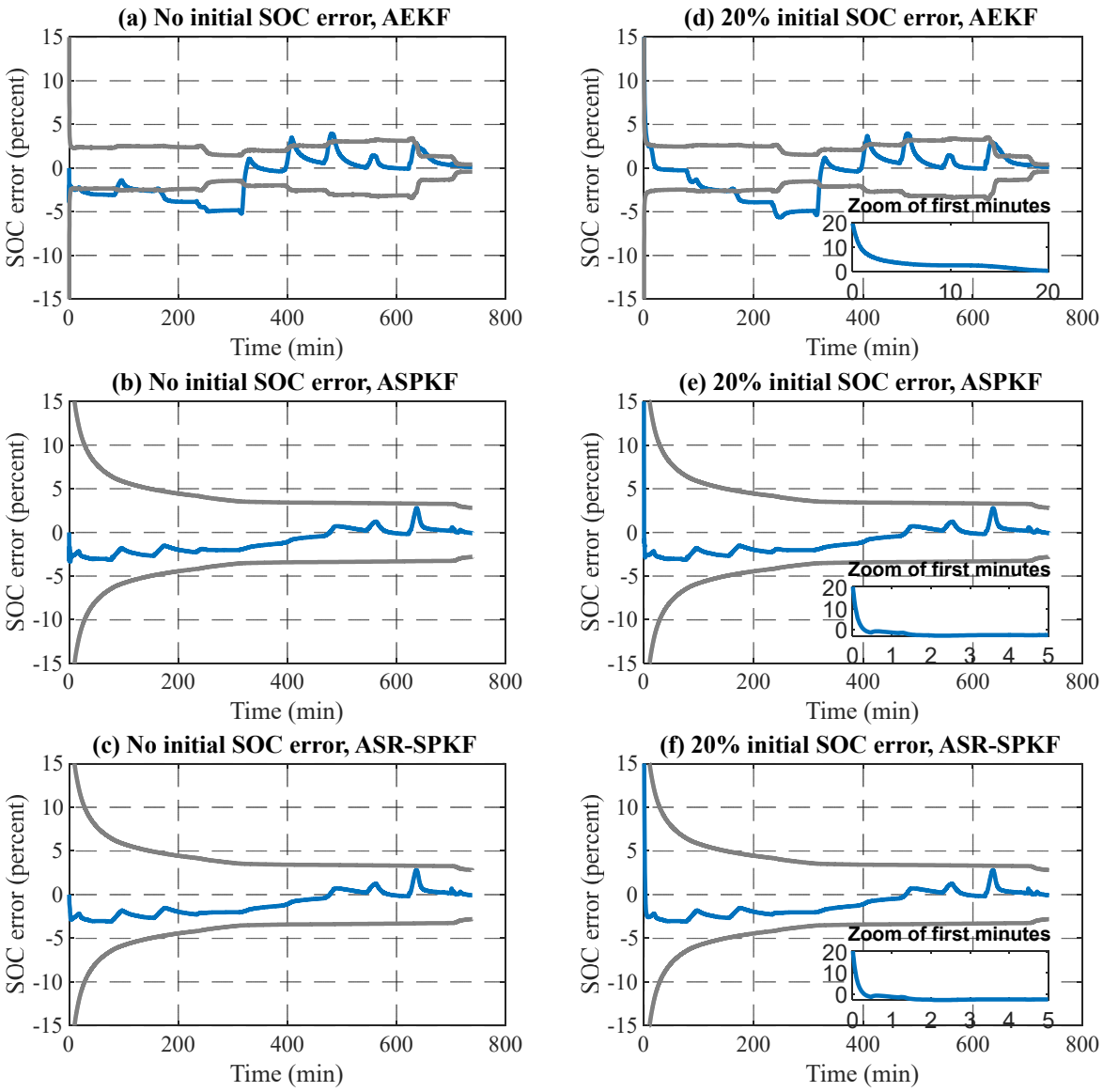

Figure 15. SOC estimation errors with error bounds of the HPPC test. (a-c) No initial SOC errors; (d-f) 20% initial SOC errors.

Table 6. Comparison of AEKF, ASPKF, and ASR-SPKF on the HPPT test of estimated SOC.

	No initial SOC errors		20% initial SOC errors		
	RMS error (%)	Maximum error (%)	RMS error (%)	Maximum error (%)	Time to converge (s)
AEKF	2.57	5.60	2.50	20.38	1116
A-SPKF	1.68	3.10	1.68	20.38	123
ASR-SPKF	1.68	3.10	1.76	20.38	129

3.3.2 Computational time

The average computational time of each filter per step is measured using a desktop computer with an eight-core 2.60 GHz Intel® i7-860 CPU and 6 GB RAM, and the results are listed in Table 7. The results were obtained by calculating the average value of the total time taken for 1000 time steps. As shown in Table 7, the computational time per step of AEKF is comparable to that of the ASPKF but more than that of the ASR-SPKF, which makes it 23% and 19% faster than the former, respectively. As a result, the ASR-SPKF is the most efficient method to implement in the BMS hardware.

Table 7 Average computational time per step.

	AEKF	ASPKF	ASR-SPKF
Avg. computational time/step (ms)	0.586	0.559	0.451

3.3.3 Validation at different temperature

Based on the above comparative studies, we have concluded that the ASR-SPKF had the most outstanding performance. In order to test the performance of the proposed method at different

temperatures, comparisons of SOC of CC discharging were made and are plotted in Figure 16(a) and (c). The solid lines and dots represent the experiments and simulations, respectively. Since a constant current was applied, the slope of the SOC should be a constant. Moreover, some parameters, such as diffusion coefficients of the solid and electrolyte phase are highly sensitive to the temperature variation. Capacity is especially affected by the diffusion coefficient of the solid; thus, the discharge time at 45 ºC was longer than at 25 ºC, even with the same discharge rate. Therefore, the temperature dependence of the diffusion coefficients is modeled using the Arrhenius-type equation.

$$D_s = D_{s0} \cdot \exp\left[\frac{E_a}{R}\left(\frac{1}{T_0} - \frac{1}{T}\right)\right], \tag{67}$$

where E_a is the activation energy.

The SOC estimations were in a good match with the experimental results. Figure 16(c) and (d) show that the estimated errors quickly converged from the initial offset and remained within ± 1%. This is comparable to the results of using the ECM that is reported in Ref. [32] (that is, less than 1.5%). In the next section, we show that by using the ROM, the internal variables could also be predicted, which becomes an improvement when compared with an ECM-based method.

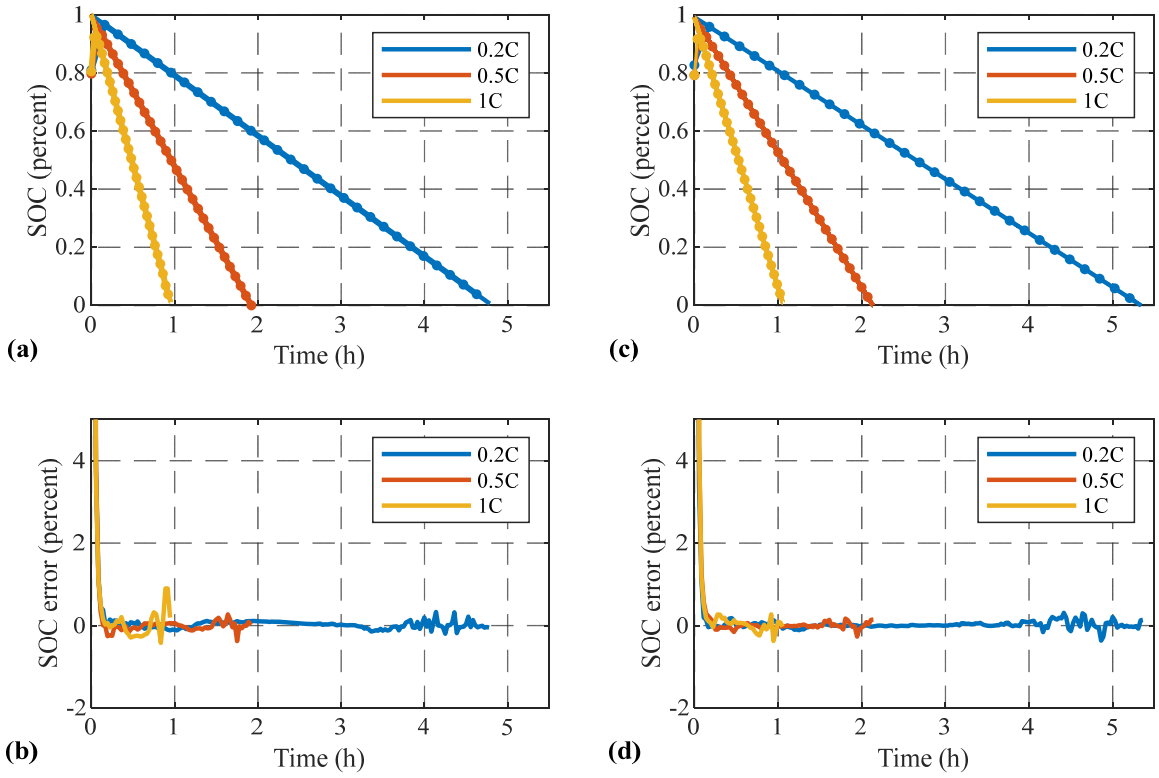

Figure 16. SOC estimation results when using the proposed method at different temperatures. (a-b) Comparison of SOC and SOC errors at 25 ºC; (c-d) comparison of SOC and SOC errors at 45 ºC. Solid lines and dots indicate the experimentally obtained and estimated SOC, respectively.

3.3.4 Validation of BIL test

Finally, the proposed method was implemented into a BIL test station. Figure 17 depicts the configuration of the testing station that consists of a computer that embeds LabVIEW, a data acquisition board, a power supply, an electric load, and a battery that is placed in a thermal chamber. The ROM with the SOC estimation algorithm was written in a MATLAB script and embedded in the LabVIEW. At each time step, the input current profile was updated. The terminal

voltage and temperature were also measured, and the difference between the measured and estimated voltage was calculated to estimate SOC and ion concentrations.

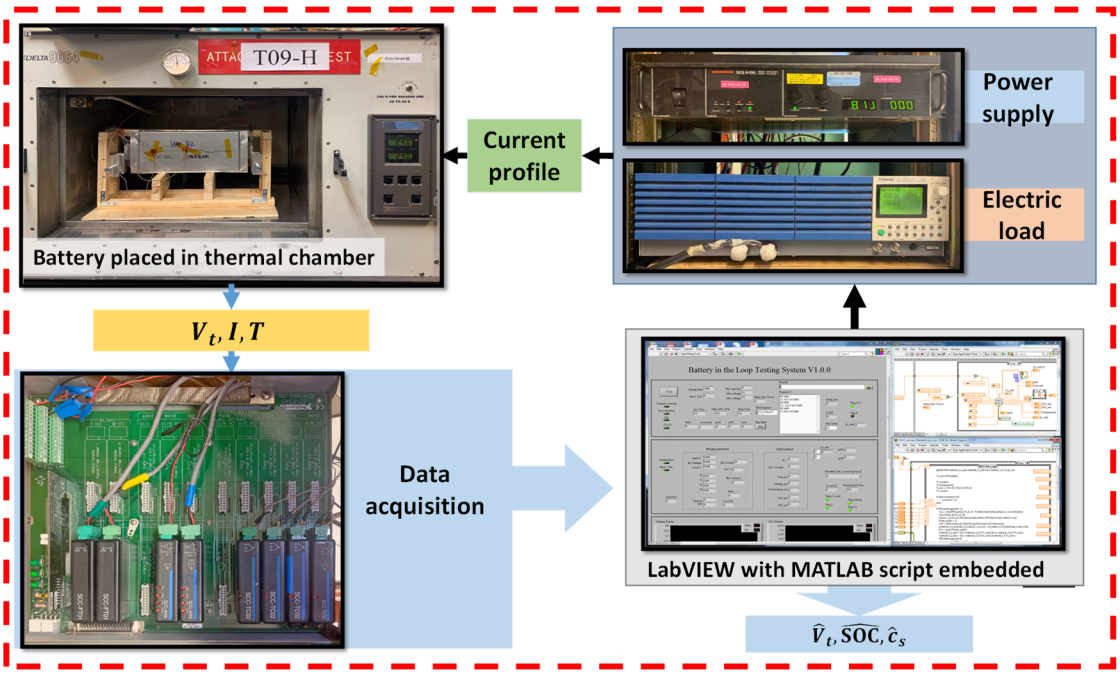

Figure 17. Schematic diagram of the BIL testing station.

To assess voltage and SOC estimation accuracy during a fast charging test. A profile from 0% to 98% SOC was generated as an example, which includes pulse charging, CC charging with decreasing C-rate and CV charging, as shown in Figure 18(a). The maximum charge and discharge rates were 5 C and 2 C, respectively. In Figure 18(b), the solid blue line, solid purple line, and dashed red line represent the terminal voltage of experiments, the ROM, and the ROM with the ASR-SPKF, respectively. Based solely on the plots of voltage, both simulated voltages are consistent with the experimental data. However, the voltage errors plotted in Figure 18(c) show that the voltage errors during the pulse charging and discharging were higher. This is because when a high-current pulse is applied, overpotential builds rapidly. Thus, when a negative pulse is subsequently applied, the terminal voltage of the cell decreases drastically, which also occurs with

the concentration gradient. Furthermore, due to model simplification, the concentration gradient inside an electrode is ignored, so the drastic change in voltage cannot be accurately predicted. The ASR-SPKF took voltage measurement into consideration, and the voltage error decreased from 35 mV to 22 mV. Additionally, in the CV region, using the proposed method further decreased errors by 4 mV. The SOC calculated from the average ion concentration also had a good match with experiments, as shown in Figure 18(c). It is also noticed that the SOC changes smoothly compare to the terminal voltage, due to the change in overpotential is affected by the surface concentration instead of its average. The SOC error was shown in Figure 18(d), which was less than 2%. Figure 18(e) shows the surface (dashed line) and average (solid line) ion concentrations of the composite anode and cathode, respectively. During charging, the surface concentration was higher than the average concentration in the anode due to the diffusion process of lithium ions. On the surface of an electrode particle, the accumulated lithium ions easily saturated the plated as metallic lithium. Therefore, the surface concentration should be estimated in conjunction with the average concentration.

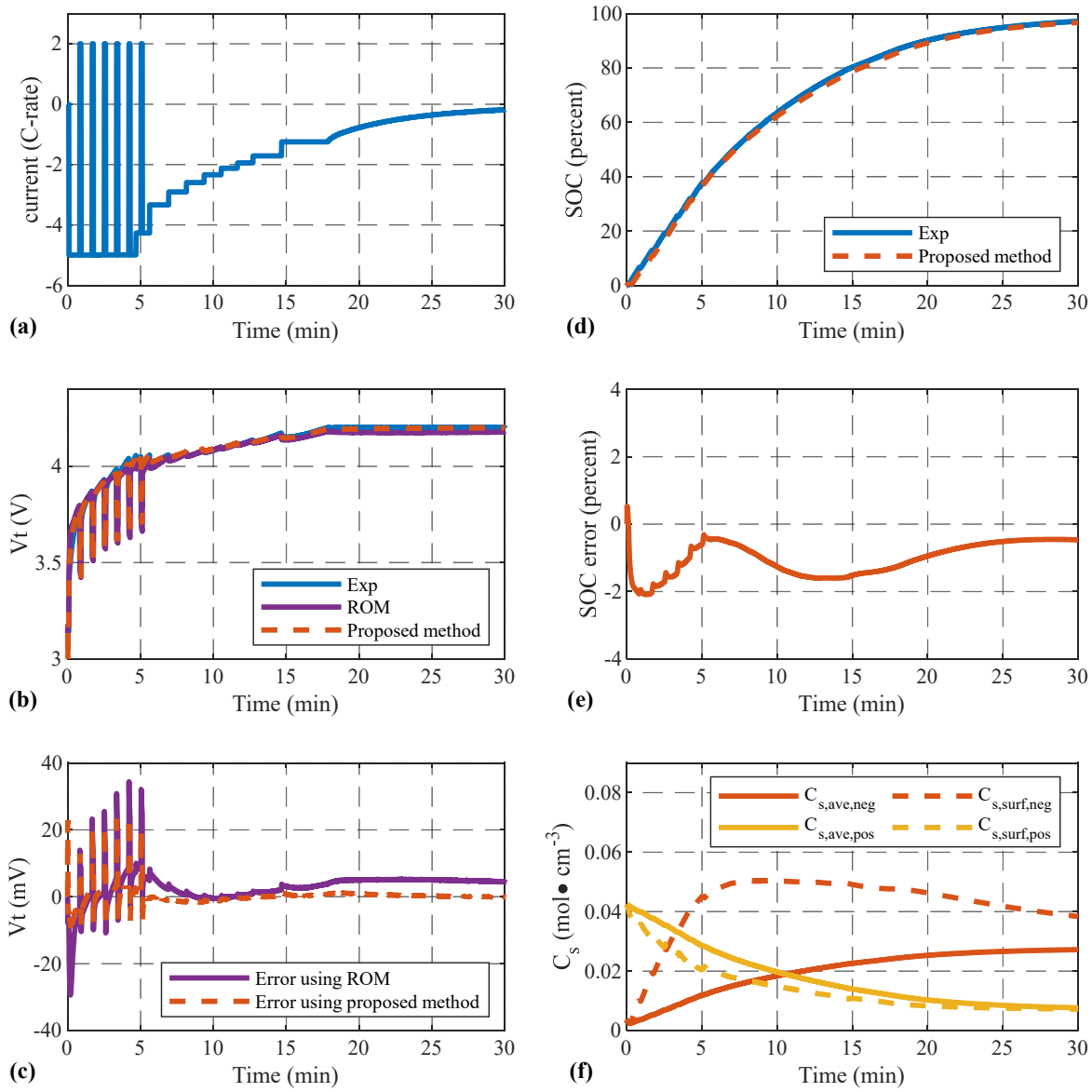

Figure 18. Results of a BIL test using a fast charging profile. (a) Current profile; (b) estimated and experimentally-measured terminal voltage; (c) voltage errors; (d) estimated and experimentally obtained SOC; (e) SOC estimation errors; (f) ion concentration in solid.

SOC and voltage estimation performance was also tested using a driving cycle profile. The current profile, as shown in Figure 19(a), is an electric vehicle driving cycle with a maximum current rate of 1.5 C. Although the terminal voltage of experiments, the ROM, and the ROM with

the ASR-SPKF matched well with each other as shown in Figure 19(b), the maximum voltage error produced using the ASR-SPKF was 20 mV less than when using only the ROM, as shown in Figure 19(c). The ASR-SPKF also eliminates the accumulation of voltage errors in the ROM. This shows that the proposed method can accurately predict the terminal voltage up to 10 Hz. The estimated SOC and SOC errors are plotted in Figure 19(d) and (e), where the maximum SOC errors were less than 2%. That is four times smaller than the results reported in Ref. [6], where a similar driving cycle input profile was used. Moreover, recently published data-driven methods produce SOC error that is comparable to that of this work [33,34]. In Figure 19(e), the dashed and solid lines show the surface and average ion concentrations in solid of the anode and cathode, respectively. The magnitude of the surface and average ion concentrations are nearly the same due to the current of the profile was primarily small, that is, within ±1 C.

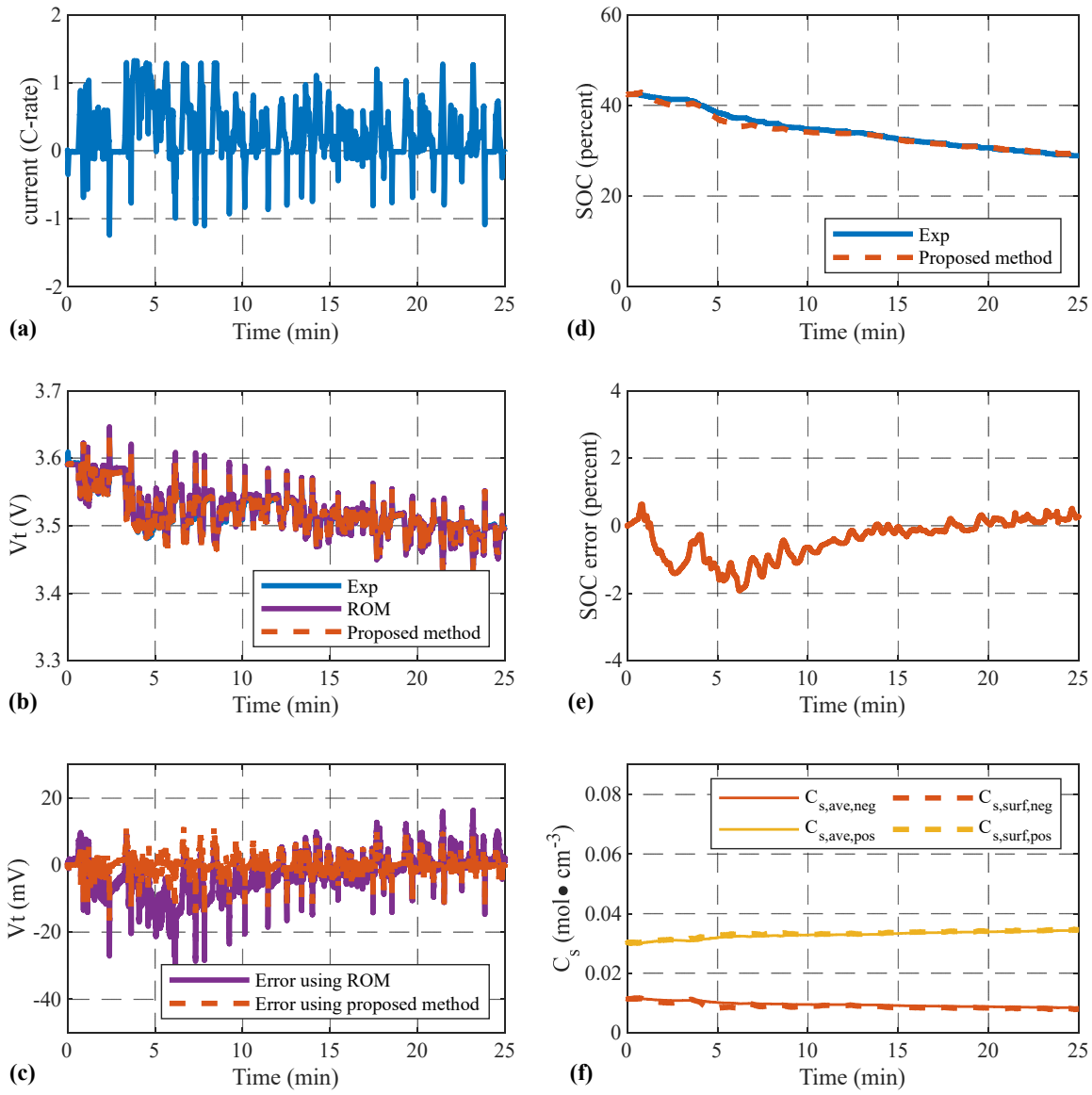

Figure 19. Results of a BIL test using a driving cycle profile. (a) Current profile; (b) estimated and experimentally-measured terminal voltage; (c) voltage error; (d) estimated and experimentally-obtained SOC; (e) SOC estimation error; (f) ion concentration in solid.

3.4 Summary

In this section, a new SOC estimation algorithm is proposed based on a reduced-order electrochemical model. The key ideas are: First, the algorithm was modified from a standard

Kalman-based nonlinear filter by adding extra equality constraints to the state vector and an adaptive algorithm that automatically adjusts the covariance matrices of process and measurement noise of the system. Specifically, the constraints were introduced that is based on the principle of the charge conservation, which allows for estimating the SOC from the ion concentration in solid of the cathode, rather than the anode, due to a higher magnitude of the equilibrium potential, which accelerates the convergence of the estimation. Second, an adaptation algorithm was integrated that is based on covariance-matching method, which allows for updating the covariance matrices of unknown process noise. Third, the performance of three candidates–AEKF, ASPKF, and ASR-SPKF–was evaluated in terms of accuracy, error bounds, convergence time, and computational time. The accuracy of SOC estimation by ASR-SPKF and ASPKF is similar and better than the AEKF with reliable error bounds, while the computational time of ASR-SPKF and AEKF is comparable and shorter than the ASPKF. Therefore, the ASR-SPKF was used for estimating SOC in real-time. Finally, the proposed method was verified at 25 ºC and 45 ºC, respectively, and finally tested using a BIL test station. Voltage and SOC errors observed using the fast charging profile were less than 22 mV and 2%, respectively, whereas these were less than 10 mV and 2%, respectively, during the driving cycle. Internal variables, such as surface and average ion concentration, were also estimated.

In conclusion, the proposed SOC estimation algorithm is able to estimate the SOC and internal variables with high accuracy and speed. An extension of the presented algorithm is a SOC/SOH co-estimator that is based on the ROM incorporated with a degradation model. Since the ion consumption inside the negative electrode reduces the number of cyclable ions, the charge conservation would always constrain the estimator that results in accurate SOC. On-going work is also focused on the development of optimal charging schemes that utilized the proposed algorithm

to reduce charging time and aging process while within safe and reliable operations constraints imposed on the SOC as well as internal variables.

Chapter 4. Online aging parameter and SOH estimation

4.1 Literature review

Lithium-ion batteries age during charging and discharging, and consequently their available energy and power decrease over time, which is directly related to the state of health (SOH) as an important metric to assess the performance of a battery. The SOH is commonly indicated by a decrease in cell capacity and an increase in internal resistance, which is mainly caused by undesirable side reactions that eventually lead to the loss of lithium ions and active materials, consumption of electrolytes solvents, and increase in solid electrolyte interphase (SEI) layer thickness, thus results in changes to aging parameters, such as the number of cyclable ions, volume fractions, and cell internal resistances. Therefore, an accurate estimation of the SOH and aging parameters is crucial for fulfilling load requirements, ensuring safe operations, extending lifespan, and reducing maintenance costs [35].

SOH is referred to as the percentage loss of capacity or power compared to the initial conditions. For instance, the end-of-life (EOL) is defined when the present capacity reaches 80% of the initial nominal capacity [36]. In order to determine the SOH directly, the present capacity or resistance needs to be measured accurately in a laboratory environment [37]. However, such methods require fully charging or discharging of a cell, or the impedance measurements and cannot be used for onboard applications.

In addition, during aging, numerous degradation processes take place that are functions of operating conditions. One of the dominant causes of degradation is the formation of an SEI layer that takes place at the interface between solid electrode particles and the electrolyte of the anode [9,38]. The growth of the SEI layer consumes cyclable lithium ions and the electrolyte solvent,

which decreases the effective surface area of electrode particles and the ionic conductivity, eventually leading to irreversible capacity and power fade [36]. Moreover, at low temperatures or high charging rates, another degradation mechanism called “lithium plating” takes place on the surface of the anode solid particles, predominantly near the separator. During charging, lithium ions from the electrolyte are inclined to form solid lithium metal and are deposited on the surface of the anode particles. Under certain circumstances [39,40], during discharging, the plated lithium can be partially dissolved and recovered as cyclable ions, which results in reversible capacity, known as “lithium stripping”. Meanwhile, the other portion of the plated lithium will further combine with electrolyte solvents to form compounds known as the “secondary SEI layer”, resulting in irreversible lithium loss [41].

These degradation processes make it challenging to mathematically and comprehensively describe the aging phenomenon. On the one hand, the SEI layer formation reaction has been modeled using a linearized Tafel equation to compute the flux rate of this side reaction, and it has been suggested that the layer thickness can be modeled as a time-dependent, one-dimensional film [42]. Using such a model, Ramadass et al. studied the effects of aging parameters, including film resistance, exchange current density, and side reaction overpotential [38]. On the other hand, Arora et al. first proposed a lithium deposition reaction model to describe the overcharge of the negative electrode and also studied related parameters [43]. Later, the model is modified to describe plating at the subzero temperatures [41]. Most recently, researchers have developed degradation models that combine the SEI layer formation with the lithium plating to achieve higher model fidelity. Studies using such models have shown that SEI growth is dominant in early cycles, while lithium plating starts to occur after a certain number of cycles, which causes an acute decrease of capacity [44]. However, the lithium stripping process has not been considered and the simulated results

were not validated against experimental data as a function of cycle numbers. Song et al. incorporated the lithium stripping into the degradation model and enables a separate calculation of capacity fade with respect to SEI layer formation, lithium plating, and lithium stripping [39].

Based on the aging model, approaches for parameter and SOH estimation have been developed. Fu et al. [45,46] estimated the decrease in the volume fraction of the active materials, and the increase in the resistance of SEI layer as the cycle number increases. In addition, the relationship between aging parameters and capacity and power fade was calculated, resulting in 2% and 3% error, respectively [19]. Without the consideration of aging mechanisms, another study used a pseudo-two-dimensional (P2D) model to optimize five parameters, including the maximum ion concentration, diffusivity and cell resistance by minimizing the terminal voltage error of aged cells using the genetic algorithm [47]. However, for each cell, an empirical relationship between the aging parameters and the battery degradation rate needs to be established, which is difficult to be generalized. Overall, the methods mentioned above might be easy to obtain high accuracy in a laboratory environment. However, an aging model alone is not suitable for online and onboard estimation for the following reasons:

1. An FOM is not appropriate for real-time implementation, which requires a simple and incrementally discretized model.
2. Degradation speed largely depends on operating conditions. Therefore, results from a single testing condition cannot be generalized to onboard operations.
3. Computing the degradation model in real time requires knowledge of the present capacity of a cell, which in practice, is difficult to measure.

Therefore, in order to estimate the SOH and parameters based on a physics-based model, first, the FOM should be simplified and discretized to create a platform of a real-time model that is, an incremental reduced-order degradation model, in which a future state can be updated based on the present state and an arbitrary input current [9]. Secondly, an adaptive filter can be applied that enables estimation in real-time. Since the model describes a highly nonlinear, non-Gaussian process, the particle filter is appropriate for this application [48,49].

Although many efforts have been made to develop algorithms for SOH estimation, challenges still remain, such as SOH prediction under various operating conditions, and the optimization of battery performance to minimize the degradation rate. Therefore, in this work, the objective is to develop algorithms for accurate estimations of not only the SOH but also aging mechanism-related parameters. The proposed method is able to estimate parameters, including the loss of lithium ions, decreases in the volume fraction of particles, and increases in the internal resistance due to the growth of the SEI layer and plated lithium based on a ROM. In addition, a particle filter is applied to facilitate the estimation of the SOH online even when a present capacity is not available. Moreover, the proposed method is well validated with different operating conditions, including different temperatures and current rates. Therefore, three contributions are made:

1. A new ROM is developed for onboard applications, where a single particle model (SPM) is applied to the cathode for maximum reduction of computation complexity, while a P2D model is used in the anode, making available the potential gradient across the thickness direction so that lithium plating and stripping can be predicted.

2. A sensitivity analysis of aging parameters is conducted by studying analytical derivation of sensitivity functions of the terminal voltage and the SOC with respect to five key parameters.

3. To the best of the authors' knowledge, for the first time, a particle filter is incorporated into the physics-based aging model for online parameter and SOH estimation, which enables online diagnosis even when a laboratory test is not available. The proposed method is also validated against experiments conducted at different temperatures and current rates.

4.2 Degradation model

Of all the degradation mechanisms, side reactions that occur at the electrode-electrolyte interface on the anode are considered to be the primary cause [42]. In particular, two dominant degradation mechanisms are the formation of the SEI layer and lithium plating. The SEI layer formation reaction is more likely to occur at elevated temperatures, where a passive layer is formed on the surface of the anode particles. When the active material of the anode is graphite and the electrolyte solvents are ethylene carbonate (EC), the main compounds of the deposits are Li_2CO_3 and $(CH_2OCO_2Li)_2$, which are described by Eqs. (68) and (69), respectively.

$$2Li^{+}+2e^{-}+EC\rightarrow C_2H_4\uparrow+Li_2CO_3\downarrow, \tag{68}$$

$$2Li^{+}+2e^{-}+2EC\rightarrow C_2H_4\uparrow+(CH_2OCO_2Li)_2\downarrow. \tag{69}$$

When a cell is charged for the first time, an initial SEI layer is created that protects the graphite from further reactions with the remaining solvent in the electrolyte, due to its permeability to ions and the impermeability to the electrons. As a cell ages, the pores of the particles are covered with the SEI layer, which leads to a decrease in the accessible active electrode surface area and an increase in the internal impedance. In addition, the reduction reaction that produces the SEI layer

consumes lithium ions at the same time and, eventually, a number of particles will be isolated with ions trapped inside, which leads to the further and simultaneous loss of ions and active materials. As a result, the SEI layer grows, which leads to both power and capacity fade.

The second mechanism, lithium plating, usually occurs acutely at subzero temperatures or under high charging rates when ion diffusion inside the solid particles is slow. When charging a cell under such cases, the surface solid-electrolyte potential difference becomes negative, especially near the separator, which causes lithium ions from the electrolyte to be reduced to metallic lithium, which deposits on instead of intercalating into the anode particles. This process can be described as

$$\mathrm{Li}^{+}+e^{-}\leftrightarrow\mathrm{Li}_{(s)}. \tag{70}$$

Furthermore, the plated lithium metal tends to react with the electrolyte and to form insoluble deposits with a composition similar to that of the SEI layer, called the "secondary SEI layer", therefore leading to irreversible ion loss and increased impedance. On the other hand, under certain conditions, a certain amount of plated lithium can be dissolved and recovered as ions before further reactions, which is called "lithium stripping" [40,50].

In order to develop a physics-based degradation model, the following assumptions are made:

- Only side reactions that take place in the negative electrode are considered and theses reactions are regarded as occurring independently [36].
- During SEI layer formation, the oxidation reaction rate is much slower than the rate of reduction and is therefore neglected. In other words, SEI layer formation is an irreversible process.

- Lithium deposition reaction is semi-reversible, which implies that the reduction reaction rate is twice as that of the oxidation rate.
- Both the primary and secondary SEI layers are a mixture of Li_2CO_3 and $(CH_2OCO_2Li)_2$.
- Other degradation mechanisms, such as mechanical stress and the dissolution of cathodic active materials, are not considered.

4.2.1 Main reaction

The main intercalation reaction rate, j_{int}, which is governed by the Butler-Volmer equation, is described by the main electrochemical reaction that takes place at the interphase between the solid and electrolyte as

$$j_{int} = a_s i_0 \left(\exp\left(\frac{\alpha_a F}{RT}\eta\right) - \exp\left(-\frac{\alpha_c F}{RT}\eta\right)\right), \tag{71}$$

where $a_s = 3\varepsilon/R_s$, is the specific interfacial surface area, η is the surface overpotential, α_a and α_c are the anodic and cathodic charge transfer coefficients, respectively, and i_0 is the exchange current density of the main intercalation reaction that is expressed as

$$i_0 = k(c_e)^{\alpha_a}\left(c_{s,max} - c_{s,surf}\right)^{\alpha_a}\left(c_{s,surf}\right)^{\alpha_c}, \tag{72}$$

where k is a kinetic rate constant, and $c_{s,max}$ and $c_{s,surf}$ are the maximum and surface concentration of the solid particles, respectively. The direction of ion flux is dependent upon the overpotential

$$\eta = \phi_s - \phi_e - U_{eq} - \frac{R_{SEI}}{a_s} j_{tot}, \tag{73}$$

where ϕ_s and ϕ_e are the potential of the solid and electrolyte phase, respectively. U_{eq} is the equilibrium potential, and j_{tot} is the total reaction rate that is given by a sum of the main intercalation, SEI layer formation, and lithium deposition reaction rates

$$j_{tot} = j_{int} + j_{SEI} + j_{LP}, \tag{74}$$

where j_{SEI} and j_{LP} denote the reaction rate for the SEI growth and lithium plating, respectively. R_{SEI} denotes the total resistance of the SEI layer that includes the initial, primary, and secondary SEI layers

$$R_{SEI} = R_{SEI,0} + R_{SEI,pri} + R_{SEI,sec}, \tag{75}$$

where $R_{SEI,0}$ refers to the resistance of the initial generated SEI layer, $R_{SEI,pri}$ denotes the primary SEI resistance that corresponds to the SEI layer formulation reaction, $R_{SEI,sec}$ denotes the secondary SEI that corresponds to the SEI layer generated by the further reaction of the plated lithium with solvents of the electrolyte.

4.2.2 Side reaction

The SEI layer formation reaction rate, j_{SEI}, is described using a Tafel equation, where only a reduction reaction takes place. This is consistent with the assumption that the reaction is irreversible and

$$j_{SEI} = -a_s i_{0,SEI} \exp\left(-\frac{\alpha_{SEI} n_{SEI} F}{RT} \eta_{SEI}\right), \tag{76}$$

where η_{SEI} is the side-reaction overpotential that is determined as

$$\eta_{SEI} = \phi_s - \phi_e - U_{SEI} - \frac{R_{SEI}}{a_s} j_{tot}, \tag{77}$$

where U_{SEI} is the equilibrium potential of SEI layer formation reaction that is chosen to be 0.4 V [13]. $i_{0,SEI}$ is the exchange current density of the reaction and it is a function of temperature, and n_{SEI} is the moles of ions involved in Eqs. (68) and (69) with a value of two.

On the other hand, the reaction rate of lithium plating and stripping is expressed using a modified Butler-Volmer equation:

$$j_{LP/S} = a_s i_{0,LP}\left(\exp\left(\frac{\alpha_{a,LP}F}{RT}\eta_{LP/S}\right) - \exp\left(-\frac{\alpha_{c,LP}F}{RT}\eta_{LP/S}\right)\right), \tag{78}$$

where $i_{0,LP}$ is the exchange current density, and $\eta_{LP/S}$ denotes the overpotential of lithium plating or stripping. In fact, during charging, the lithium plating occurs only at locations in the anode where $\eta_{LP/S} < 0$, i.e.,

$$\eta_{LP} = \min\left(0, \phi_s - \phi_e - U_{LP} - \frac{R_{SEI}}{a_s} j_{tot}\right), \tag{79}$$

where U_{LP} is the equilibrium potential for lithium plating and stripping, which is measured with respect to Li and is thus equal to zero [51]. Eq. (79) restricts the reaction rate of lithium plating, $j_{LP} = 0$ where $\eta_{LP} \geq 0$, and $j_{LP} < 0$ where $\eta_{LP} < 0$.

Conversely, during resting or discharging, lithium stripping takes place, and the plated lithium dissolves and is released as lithium ions. However, it should be noted that if the plated lithium has already reacted with the electrolyte solvents to form the secondary SEI, or if it has been completely covered by the SEI layer to become dead lithium, then it can no longer be dissolved. Therefore, a favored condition for lithium stripping to occur is when $\eta_{LS} > 0$,

$$\eta_{LS} = \max\left(0, \phi_s - \phi_e - U_{LP} - \frac{R_{SEI}}{a_s} j_{tot}\right). \tag{80}$$

4.2.3 Analysis of degradation effect

Once the side reaction rates have been calculated, the amount of loss of lithium ion (LLI), q_{LLI}, due to SEI growth, and lithium plating can be obtained by a summation of integration of j_{SEI} and j_{LP} over the thickness of the negative electrode, respectively:

$$\frac{\partial q_{LLI}}{\partial t} = \frac{\partial q_{LLI,SEI}}{\partial t} + \frac{\partial q_{LLI,LP}}{\partial t} - \frac{\delta q_{LS}}{\delta t} = -A\int_0^{\delta_{neg}} j_{SEI}\, dx - A\int_0^{\delta_{neg}} j_{LP}\, dx + A\int_0^{\delta_{neg}} j_{LS}\, dx. \quad (81)$$

where a dimensionless coefficient, λ, is introduced to express the fraction of the plated lithium that forms the secondary SEI, and the coefficient is obtained through validation against the experimental data.

The SEI layer thickness as a function of electrode thickness can be calculated by the ordinary differential equation:

$$\frac{\partial \delta_{SEI}}{\partial t} = -\frac{\tilde{V}_{SEI}}{n_{SEI} a_s F} \cdot j_{SEI} - \frac{\tilde{V}_{SEI}}{n_{LP} a_s F} \cdot \lambda j_{LP}, \quad (82)$$

where $\tilde{V}_{SEI}$ is the molar volume of SEI. The coefficient $n_{SEI} = 2$ indicates that the consumption of two moles of lithium ions produces one mole of SEI [18,46]. This allows the loss of active materials to be computed as

$$\frac{\partial \Delta\varepsilon_{s,neg}}{\partial t} = -k_{AM} a_s \frac{\partial \delta_{SEI}}{\partial t}, \quad (83)$$

where $\Delta\varepsilon_{s,neg}$ is the change of solid phase volume fraction, and k_{AM} is a dimensionless coefficient that describes how fast the anode materials are lost from SEI layer growth. The coefficient is obtained by validating the model simulation against the experimental data. The formation of the SEI layer and plated lithium also leads to an increase of surface film resistance:

$$R_{SEI} = R_{SEI,0} + \frac{\delta_{SEI}}{\kappa_{SEI}}, \tag{84}$$

where $R_{SEI,0}$ corresponds to the resistance of the initial formed SEI layer, and κ_{SEI} is the conductivity. Moreover, increases in the deposit layer thickness and resistance from the plated lithium can be expressed as

$$\frac{\partial \delta_{DL}}{\partial t} = \frac{\tilde{V}_{Li}}{n_{LP}F}(1-\lambda)\, j_{LP}, \tag{85}$$

$$R_{DL} = R_{DL,0} + \frac{\delta_{DL}}{\kappa_{DL}}, \tag{86}$$

where $\tilde{V}_{Li}$ is the molar volume of the plated lithium, $R_{DL,0}$ corresponds to the initial resistance of the deposit layer that is equal to zero, and κ_{DL} is the conductivity of the deposit layer. Finally, the formation of the primary and secondary SEI also consumes the electrolyte solvents as shown in Eq. (68) and (69), which is modeled by the decrease of the volume fraction of electrolyte:

$$\frac{\partial \varepsilon_e}{\partial t} = -\frac{\alpha \tilde{V}_e}{\delta_{neg}F}\int_0^{\delta_{neg}} \left(j_{SEI,k-1} + \lambda j_{LP,k-1}\right)\, dx, \tag{87}$$

where $\tilde{V}_e$ is the molar volume of the electrolyte, and α is a dimensionless coefficient indicating the number of moles of electrolyte solvents that are involved in the reaction when one mole of the plated lithium is consumed and is equal to 0.75 when assuming the same reaction rate of Eq. (68) and (69).

4.2.4 Optimization of ROM

To estimate the degradation state and parameter in real time requires information of the internal variable such as ion concentrations, electrode potentials, and the main reaction rate. These variables can be computed using a high-fidelity electrochemical model. However, such a model consists of a set of coupled nonlinear partial differential equations, which are derived from the first

principles of thermodynamics, transport theory, and electrochemical kinetics, which are solved numerically by finite difference method or finite element method. Solving these equations is very computationally expensive. For real-time applications, the model needs to be simplified while maintaining decent accuracy. In this work, a ROM where calculations of the anode and the cathode internal states are carried out by approximations of multiple particles, and a single particle, respectively. Specifically, because numerous side reactions take place in the anode with different stages of degradation across the thickness direction and increasing severity toward the separator, computation of internal variables is needed at more than one spatial location in the electrode. Conversely, because of the assumption for the cathode, the sub-model is simplified to an SPM, where only one particle is considered in the calculation. The concept is shown in Figure 20. With a separate degree of simplification, the computational time of the proposed ROM, referred to as a P2D-SPM, is greatly reduced, while its fidelity is maintained. The P2D-SPM parameters were obtained using a genetic algorithm-based automatic tuning method that was developed in our previous work [52]. The values of optimized parameters, as well as design parameters given by the manufacturer, are listed in **Error! Reference source not found.**. Temperature-dependent parameters, such as the diffusivities, were optimized by means of the Arrhenius relationship.

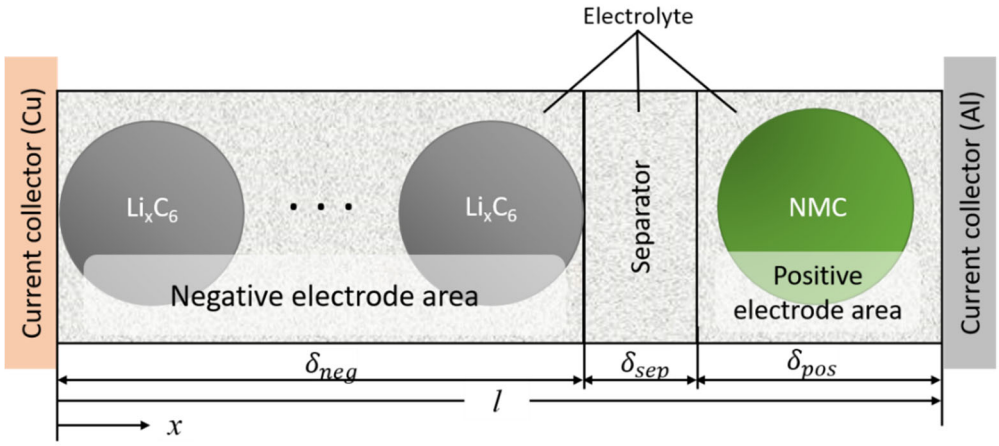

Figure 20. A schematic diagram of a P2D-SPM model.

4.2.5 Model validation

The simulated and measured capacity is compared as a function of the cycle number at different temperatures and charging rates, as shown in Figure 21(a), where more than 20% capacity fade are achieved. The simulations, represented by the solid lines, are in agreement with the experimental data, and are denoted by the dots. In addition, Figure 21(b)-(d) show the individual amount of ion loss due to SEI layer formation, lithium plating, and active material loss. At 25 ºC, the rate of degradation increases when the current rate increases, despite the ion losses due to SEI layer formation being comparable between 2 C and 3 C. Therefore, the rate increase is caused by the increased rate of lithium plating. As can be seen in Figure 21(b), no plated lithium is formed until the 60th cycle. Conversely, as shown in Figure 21(c), lithium metal starts to plate from the very first cycle. In other words, the rate of lithium plating is higher when the charging current is greater, where the lithium plating overpotential, η_{Li}, is lower; therefore, plating is more likely to occur. On the other hand, the rate of SEI layer growth increases as the temperature elevates, which can be observed by comparing Figure 21(c) and (d). By contrast, lithium plating is less likely to

take place when the temperature is higher, for instance, the simulation indicates no lithium plating at 45 ^{o}C. Moreover, the active material loss has a similar magnitude to that of the loss due to both SEI layer formation and lithium plating, which indicates its strong correlation to the loss of lithium ions [53]. The EIS spectra of the cell cycled at 25 ^{o}C, 3 C CC-CV is shown in Figure 21(e), where the impedance spectra shift rightwards as the cycle number increases, which implies an increase of Ohmic resistance. The resistance includes the resistance of electrodes, electrolytes, and current collectors. The SEI resistance, which is represented by the radius of the semi-circle in the impedance spectra, also increases as the cycle number is augmented, as shown in Figure 21(f).

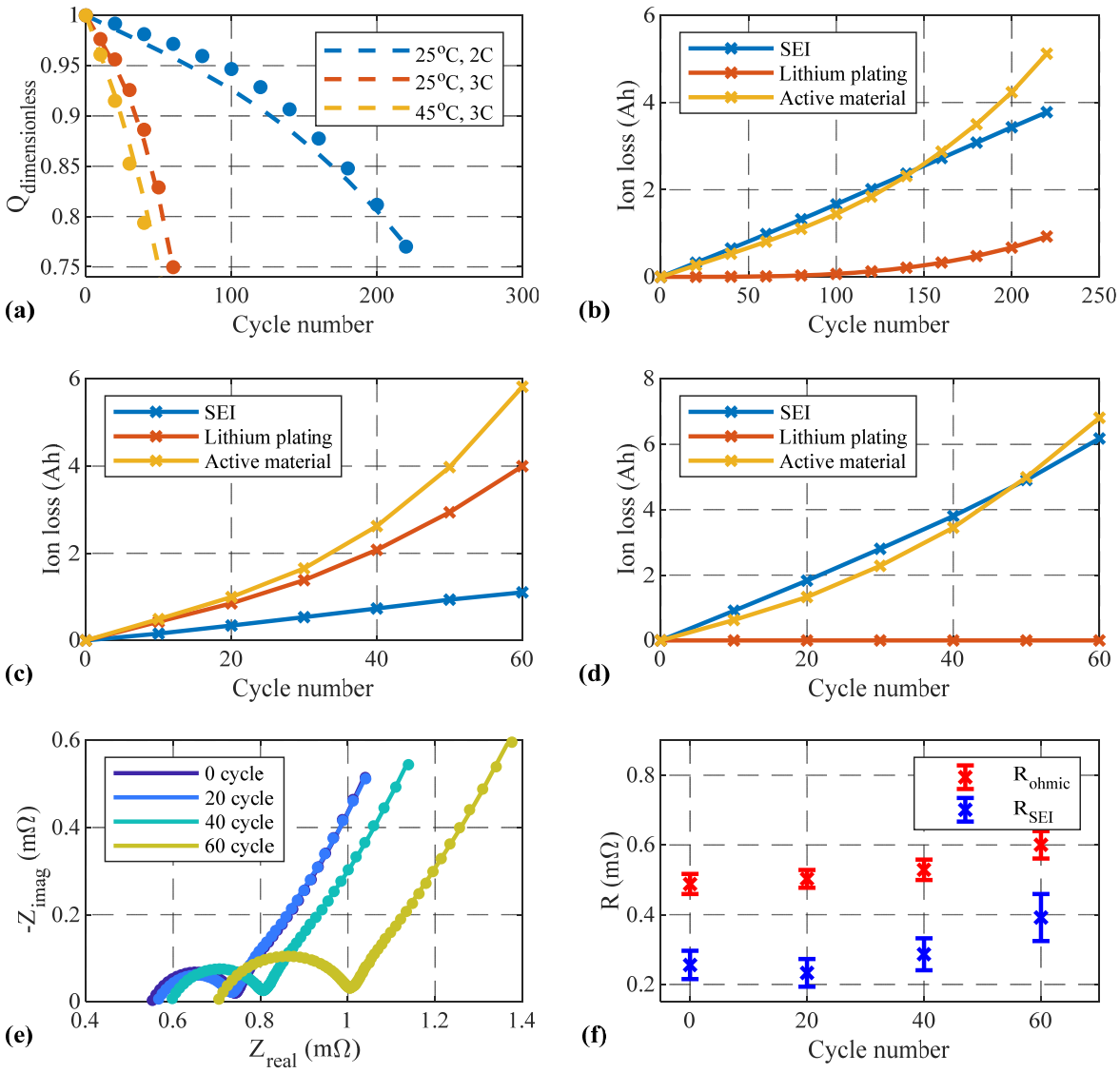

Figure 21. Validation of degradation at different temperatures and C rates: (a) comparison of simulated and measured capacity fade; (b) sources of ion loss at 25 ºC, 2C CC-CV charging; (c) sources of ion loss at 25 ºC, 3C CC-CV charging; (d) sources of ion loss at 45 ºC, 3C CC-CV charging; (e) impedance spectra of the cell cycled at 25 ºC, 3C CC-CV; (f) Ohmic and SEI resistance extracted from the EIS measurement.

4.3 Online aging parameters and SOH estimation

4.3.1 Effect of aging parameters on SOH

The aging parameters related to the SOH are the change in the loss of lithium ions, the solid active material volume fraction, the electrolyte volume fraction, the deposit layer resistance, and the SEI layer resistance, of which the first two cause the capacity fade, while the last three lead to the power fade. In addition, the loss of lithium ion affects the OCV characteristic, which causes a shift in the stoichiometric operating windows. In this section, definitions of SOH with respect to capacity (SOH_Q) and power (SOH_P) are given, respectively, and the effects of aging parameters on the SOH are analyzed.

Capacity fade is one of the most important indicators for evaluating the performance of degraded cells. A definition of SOH with respect to capacity is given as

$$SOH_Q = \frac{Q_{aged}}{Q_{fresh}} \times 100\%, \tag{88}$$

where Q_{aged} and Q_{fresh} are the maximum capacity of an aged and a fresh cell, respectively. The maximum capacity can be calculated either from the positive or negative electrode as

$$Q_{max,pos} = (y_{max} - y_{min})\varepsilon_{s,pos}\delta_{pos}AFc_{s,max,pos}\,/3600, \tag{89}$$

$$Q_{max,neg} = (x_{max} - x_{min})\varepsilon_{s,neg}\delta_{neg}AFc_{s,max,neg}\,/3600. \tag{90}$$

Because our assumption is that the degradation takes place mainly at the anode, parameters of Eq. (90) is updated. Specifically, the loss of active materials is reflected in the changes in the volume fraction of solid particles ε_s, and the loss of lithium ions is reflected in the changes in the operating window of the stoichiometric number, x_{max}-x_{min}. When lithium ions are lost because of side reactions, the stoichiometric number operating window shifts by

$$x_{shift} = \frac{q_{LLI}}{\varepsilon_{s,neg}\delta_{neg}Ac_{s,max,neg}F}, \tag{91}$$

This makes the stoichiometric number, x, less than that of the fresh cell. At the same time, a certain amount of active material of the negative electrode is lost, which is reflected in a decrease of the volume fraction. Furthermore, the stoichiometric numbers, $x_{max}, x_{min}, y_{max}, y_{min}$ must be adjusted during aging. Figure 22 shows the simulated OCV as a function of both the SOC and maximum capacity. As a cell is aged, the maximum capacity is decreased, and the shape of the OCV curve becomes smoother.

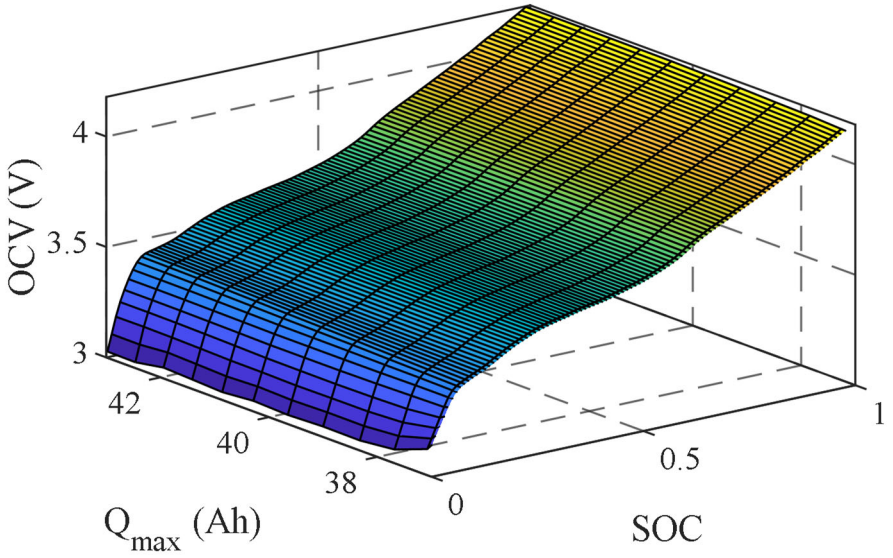

Figure 22. Change of OCV as functions of SOC and $Q_{max.}$

Another crucial indicator for cell performance evaluation is the power fade, which is mainly due to the rise of cell resistance. Similar to the SOH_Q, SOH with respect to power (SOH_P) is commonly defined by cell internal resistance as [54]

$$SOH_P = \left(1 - \frac{R_{aged} - R_{fresh}}{R_{fresh}}\right) \times 100\%, \tag{92}$$

where R_{aged} and R_{fresh} are the cell resistance of an aged and a fresh cell, respectively.

4.3.2 Analysis of aging parameters

The validated degradation model is applied to study the aging state and parameters at different temperatures with a variety of current profiles. For real-time applications, we first need to convert the continuous-time equations Eqs.(81)-(84) into discrete-time equations, as shown in Table 8.

Table 8. Discretized equation for aging parameter calculation.

$\varepsilon_{s,k} = \varepsilon_{s,k-1} + \frac{k_{AM} V_{SEI} \Delta t}{F}\left(-\frac{1}{n_{SEI}} \cdot j_{SEI,k-1} - \frac{1}{n_{LP}} \cdot \lambda j_{LP,k-1}\right)$	(93)
$q_{LLI,k} = q_{LLI,k-1} - A\Delta t \sum_{\delta_{neg}} \left(j_{SEI,k-1} + j_{LP,k-1} - j_{LS,k-1}\right)$	(94)
$R_{SEI,k} = R_{SEI,k-1} + \frac{V_{SEI}\Delta t}{F a_s \kappa_{SEI}}\left(-\frac{1}{n_{SEI}} j_{SEI,k-1} - \frac{1}{n_{LP}} \lambda j_{LP,k-1}\right)$	(95)
$R_{DL,k} = R_{DL,k-1} - \frac{V_{Li}\Delta t}{n_{LP} F a_s \kappa_{DL}} (1-\lambda) \sum_{\delta_{neg}} j_{LP,k-1}$	(96)
$\varepsilon_{e,k} = \varepsilon_{e,k-1} - \frac{\alpha V_e \Delta t}{\delta_{neg} F} \sum_{\delta_{neg}} \left(j_{SEI,k-1} + \lambda j_{LP,k-1}\right)$	(97)

In order to quantitatively investigate the effects of parameters on capacity and power, the sensitivity of the aging parameters is analyzed with respect to the terminal voltage and the SOC. First, a dimensionless sensitivity is defined as

$$S_z^\theta = \frac{\theta}{z}\frac{\partial z}{\partial \theta}, \tag{98}$$

where the superscript θ denotes the parameters, while the subscript z is the system output. Then, the sensitivity is carried out analytically. For instance, the sensitivity of the terminal voltage to the solid volume fraction is calculated by applying the chain rule as

$$S_{V_t}^{\varepsilon_{s,neg}} = \frac{\varepsilon_{s,neg}}{V_t}\frac{\partial V_t}{\partial \varepsilon_{s,neg}} = -\frac{\varepsilon_{s,neg}}{V_t}\left(\frac{\partial U_{eq,neg}}{\partial c_s}\frac{\partial c_s}{\partial \varepsilon_{s,neg}} + \frac{\partial \eta_{neg}}{\partial \varepsilon_{s,neg}}\right), \tag{99}$$

where the first term inside the parentheses, $\frac{\partial U_{eq,neg}}{\partial c_s}\frac{\partial c_s}{\partial \varepsilon_s}$, accounts for the impact of change in ε_s on the equilibrium potential through c_s [55], and the second term accounts for the overpotential. Specifically, $\frac{\partial U_{eq,neg}}{\partial c_s}$ can be obtained by differentiating the negative equilibrium potential with respect to the ion concentration in the solid, $\frac{\partial c_s}{\partial \varepsilon_s}$ can be obtained by directly differentiating the state space sub-model of c_s, and $\frac{\partial \eta_{neg}}{\partial \varepsilon_{s,neg}}$ can be further derived via chain rule:

$$\frac{\partial \eta_{neg}}{\partial \varepsilon_{s,neg}} = \frac{\partial \eta_{neg}}{\partial a_{s,neg}}\frac{\partial a_{s,neg}}{\partial \varepsilon_{s,neg}} = -\frac{3R\cdot T\cdot j_{int}}{2\alpha\cdot F\cdot i_0\cdot a_{s,neg}^2\cdot R_s}\frac{1}{\sqrt{1+\left(\frac{j_{int}}{2i_0 a_{s,neg}}\right)^2}}. \tag{100}$$

The rest of the dimensionless parameter sensitivity to the terminal voltage and SOC is computed similarly. The sensitivity is calculated using both static and dynamic input profiles, namely, the CC discharging, and dynamic stress test (DST) profiles. It is noted that since the SOC is not a function of R_{DL} and ε_e, the sensitivities are equal to zero. Figure 23 visualizes the ranks of the averaged dimensionless sensitivity magnitudes over different input profiles.

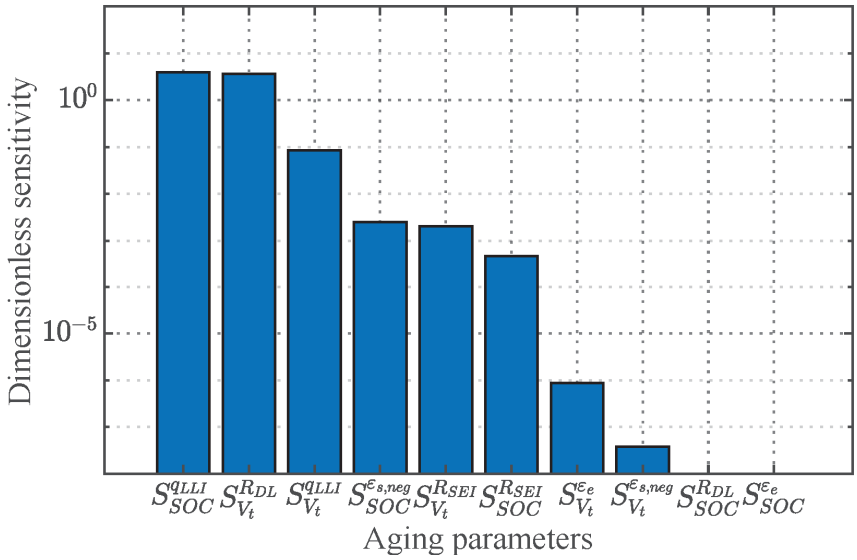

Figure 23. The sorted averaged dimensionless parameter sensitivity.

As shown in Figure 23, the sensitivity of q_{LLI} to the SOC as well as the sensitivity of R_{DL} to the terminal voltage are the highest. This is because, on the one hand, the loss of lithium ions shifts the range of the stoichiometric number [56], directly affecting the SOC; while, on the other hand, the change of R_{DL} contributes to the change of cell internal resistance, which is related to the terminal voltage by a scaling factor, which is the magnitude of the input current, therefore, it also has a relatively high sensitivity, which is also consistent with the results reported in $S_{V_t}^{q_{LLI}}$ is less than $S_{SOC}^{q_{LLI}}$ because the ion loss affects V_t through the slope of the anode equilibrium potential,$\frac{dU_{eq,neg}}{dx}$, which is small in magnitude. Finally, $S_{SOC}^{R_{SEI}}$, $S_{V_t}^{R_{SEI}}$, and $S_{SOC}^{\varepsilon_s}$ have comparable high sensitivity and are larger than $S_{V_t}^{\varepsilon_e}$, and $S_{V_t}^{\varepsilon_s}$. Overall, the conducted sensitivity analysis provides the following conclusions.

- Since the volume fraction of the electrolyte, ε_e, has a low sensitivity to V_t and no effects on the SOC, therefore, it is not considered as an estimated parameter.

- Four parameters will be estimated online—that is, the lithium ion loss, q_{LLI}, the deposit layer and SEI layer resistance, R_{DL} and R_{SEI}, and the active material volume fraction of the anode $\varepsilon_{s,neg}$.

4.3.3 SOH and parameter estimation using a particle filter

4.3.3.1 State and output equation

Despite the performance of the degradation model has been demonstrated, there are still errors, particularly in real-time applications, such as:

- Lack of knowledge of the present states of aging parameters, which are usually not precisely known.
- Model uncertainties due to simplified assumptions and unmodeled dynamics of side reactions.
- Measurement errors caused by a current or voltage sensor.

To actively compensate for these errors, an online aging parameter and SOH estimation algorithm is designed based on the ROM with the consideration of degradation and a particle filter. In particular, a general discrete-time state-space form for the particle filter is shown as

$$x_k = f_{k-1}(x_{k-1}, u_{k-1}, w_{k-1}), \tag{101}$$

$$z_k = h_k(x_k, u_k, v_k). \tag{102}$$

Eq. (101) is the state equation, where x_k is the state vector of the system at time index k. In this work, the aging parameters are chosen as the state of the filter, namely, $x = [q_{LLI} \quad R_{DL} \quad R_{SEI} \quad \varepsilon_{s,neg}]^T$. u_k denotes the input of the system, that is, $u_k = [j_{SEI} \quad j_{LP}]^T$,

where the process noises, w_k, are added to model the unknown dynamics that affect the state of the system. v_k represents the measurement noise that affects the measurement of the system. The output of the system in Eq. (102), z_k, which is a function of x_k, u_k, and v_k, is chosen to be $z = [V_t \quad SOC]^T$.

The concept of using a particle filter for SOH and aging parameters estimation is shown in Figure 24The ROM with a degradation model that comprises the P2D-SPM and aging dynamics calculates the side reaction rates that serve as inputs to the state. At each time step, the particle filter takes into account the difference between the measured and calculated V_t and SOC to adapt the aging parameters through equations described in Table 8. At the same time, the updated aging parameters are also applied to the degradation model for calculation of the next time step.

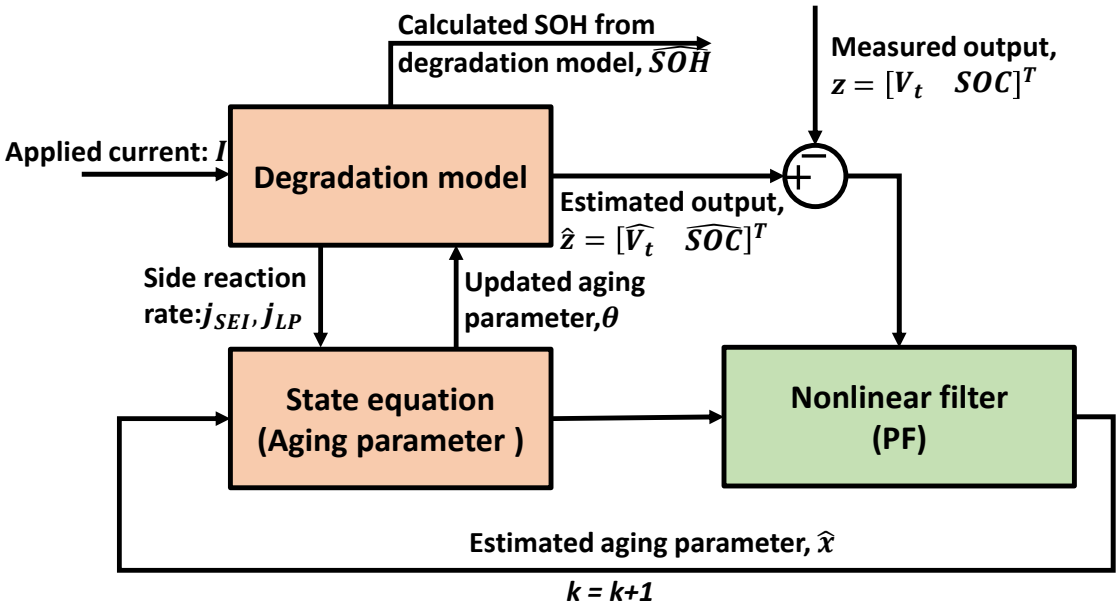

Figure 24. Concept of PF for aging parameter and SOH estimation.

4.3.3.2 Principle of Particle filter

A particle filter is a state space tracking algorithm that is suitable for state and parameter estimation for highly nonlinear systems with non-Gaussian noise. Compared to other commonly used nonlinear filters such as the extended Kalman filter (EKF) [57], and sigma-point Kalman filter (SPKF) [58], the advantages of the particle filter are summarized as follows:

- *Increased accuracy.* Existing online SOH estimation methods assume capacity or internal resistance as constant parameters [59,60]. Incorporation of degradation mechanisms model provides detailed dynamics about how aging parameters and capacity change are subject to input current, temperature, and other operating conditions.

- *Better error bounds*. Particle filters release the white noise assumption of the process and measurement noises to arbitrary distributions. Particularly for nonlinear systems, a more accurate estimation of distribution leads to a tighter error bound and an increased confidence level for the estimation.

- *Automatic incorporation of state constraints.* Aging parameters are physically reasonable within a specific numerical range, which is interpreted mathematically as inequality constraints that can be incorporated automatically by defining the region of support of the distribution of the states.

Due to the above advantages, the particle filter is used to estimate aging parameters and SOH in real-time. In fact, there are uncertainties in the model and unknown noise in the measurement. Due to this randomness in the model and measurements, the estimated states are regarded as random variables, each of which is represented by a particle set. These “particles” are obtained by drawing samples from the posterior probability density function, which is derived from the

probabilities of state estimates from the last time step. In conjunction with the particle, a set of corresponding weights are also propagated through a recursion that utilizes the likelihood of the output measurements. There are several types of proposed particle filters, of which the sequential importance sampling (SIS) is one of the most widely used forms [61].

Essentially, the algorithm consists of two steps: prediction and correction. In the prediction step, a predicted posterior—that is, a probability of estimation state given all the measurements up to the previous time step—is calculated as

$$p(x_k|\, z_{0:k-1}) = \int \; p(x_k|x_{k-1})p(x_{k-1}|z_{0:k-1})\, dx_{k-1}, \tag{103}$$

where x_k is the state vector of the system at time index k, and $z_{0:k-1}$ denotes the output of the system from time $t = 0$ up to $t = k - 1$.

In fact, analytical solutions of the integral are impossible to obtain due to the complexity of the physics-based aging model. On the other hand, the computational intensity of using numerical integration increases acutely as the dimension of the state increases, which is inappropriate for real-time implementation. The particle filter carries out this integration by the Monte Carlo method, which approximates the results of integration with a finite number of samples, which is called "particles" by convention. It is noted that the term *particle* here is different from the physical electrode particles mentioned in the electrochemical model.

When the measurement of the present time is available, the posterior can be updated using the Bayes' rule

$$p(x_k|\, z_{0:k}) = \frac{p(z_k|x_k)p(x_k|\, z_{0:k-1})}{p(z_k|\, z_{0:k-1})}. \tag{104}$$

This expression can be further reformulated by the introduction of weights,

$$w_k^{(i)} = \frac{p\left(z_k|x_k^{(i)}\right)p\left(x_k^{(i)}|x_{k-1}^{(i)}\right)}{q\left(x_k^{(i)}|x_{k-1}^{(i)},z_k\right)} w_{k-1}^{(i)}, \tag{105}$$

where q is the importance density and chosen to be the prior, that is $q\left(x_k^{(i)}|x_{k-1}^{(i)},z_k\right) = p\left(x_k^{(i)}|x_{k-1}^{(i)}\right)$ [61]. As the iteration precedes, the updated weights are likely to deviate and lead to the ineffectiveness of the majority of the particles, which is referred to as the particle degeneracy problem [62]. This issue is addressed by resampling the particles when the effective sample size,

$$N_{eff} = \frac{1}{\sum_{i=1}^{n_p}\left(w_k^i\right)^2}, \tag{106}$$

is below a threshold chosen to be 10% of the total number of particles, $N = 0.1n_p$. A detailed algorithm of a particle filter can be found in [62].

Moreover, the resulting posterior consists of a set of weighted impulses. In order to solve for the error bounds of the estimation, a kernel density estimation method is used, that is,

$$\hat{p}(x_k) = \sum_i w_n^i b\left(x_k - x_k^i\right),$$

where b denotes the biweight kernel function.

$$b(u) = c(1-u^2)^2 p(u),$$

where c is a normalizing constant that ensures $\int_{-\infty}^{\infty} b(u)du = 1$, and $p(u)$ is a unit pulse function.

4.4 Results and discussion

4.4.1 Aging parameters estimation as a function of time

To analyze the performance of the particle filter, the estimation results of aging parameters are investigated at 25°C using 3 C as an example to promote the formation of SEI layer and plated lithium. The change of aging parameters as a function of time using a CC-CV charging profile is

shown in Figure 25 to Figure 28. In particular, the change of LLI at fifth and 60th cycles are plotted in Figure 25 and Figure 26. As shown in Eq. (76) and (78), the side reaction rate is mainly determined by the reaction overpotential, namely, η_{SEI} and η_{LP}. When a cell is being charged, the η_{SEI} is firstly decreased during the CC stage, then increased during the CV stage. At the CC, the CV transition point, η_{SEI}, reaches a minimum. In this case, the transition occurs at around 700 s, which explains the drastic increase in the change of LLI. In addition, because of the nonlinear degradation rate, the change of LLI at the 60th cycle is larger than that at the fifth cycle. By comparing the results from model validation and online simulation, the absolute error is kept within ± 0.01 Ah, which is around 6% of the maximum change of LLI per cycle. A 95% confidence interval is also provided retaining the error within the bound at the fifth cycle; whereas at 60th cycle, the error is out of the bound during CC charging. This is because of an increase in the uncertainty of the degradation model as a cell is aged. Figure 27 and Figure 28 show the estimated resistance of the deposit layer at fifth and 60th cycles, respectively. Because SEI layer formation tends to be more severe at the separator side, a distinctive dense layer is formed at the anode/separator interface, which is defined as a deposit layer [46]. The layer resistance increases as the cycle number increases. After 700 s, the particle filter estimated results match well with the model validation.

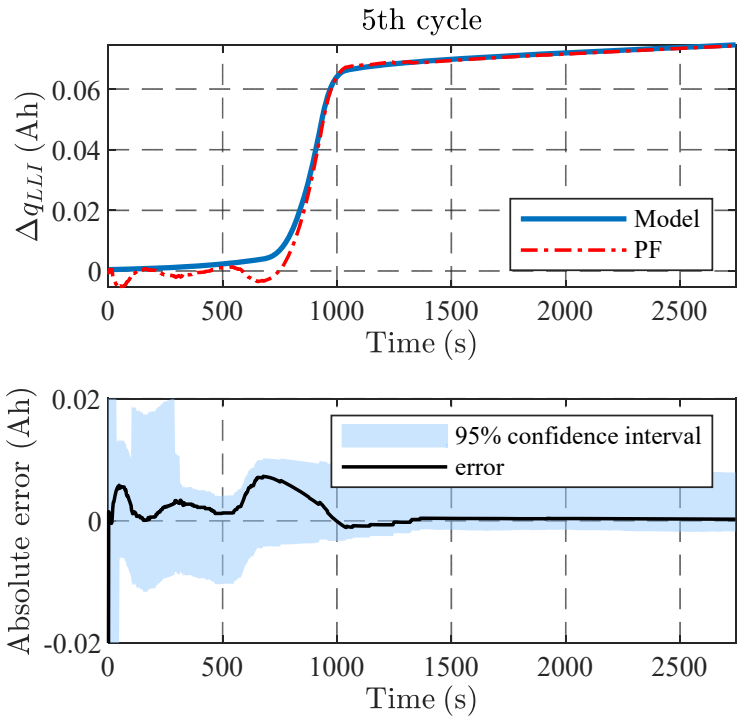

Figure 25. Comparison of change of loss of lithium ion calculated from model and PF with its absolute error together with the 95% confidence interval at the fifth cycle.

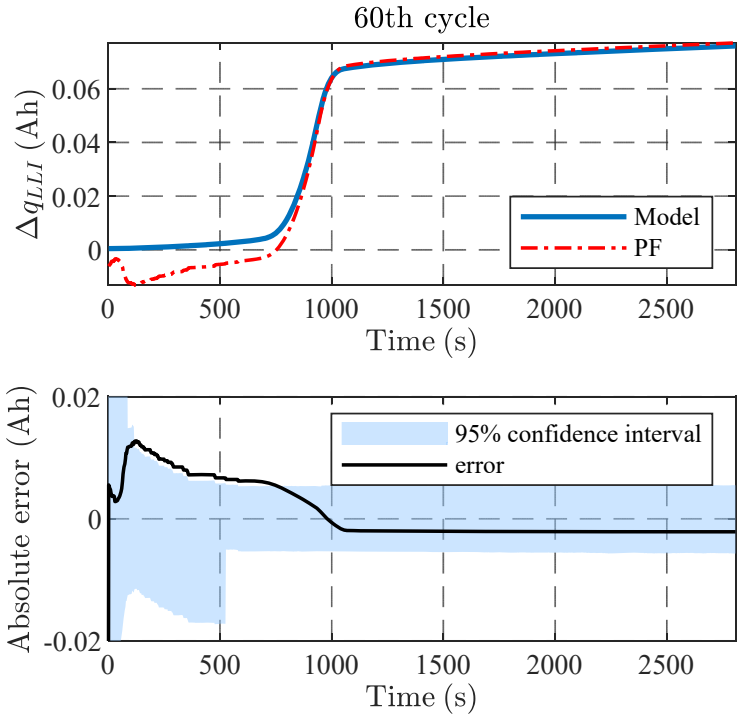

Figure 26. Comparison of change of loss of lithium ion calculated from model and PF with its absolute error together with the 95% confidence interval at the 60th cycle.

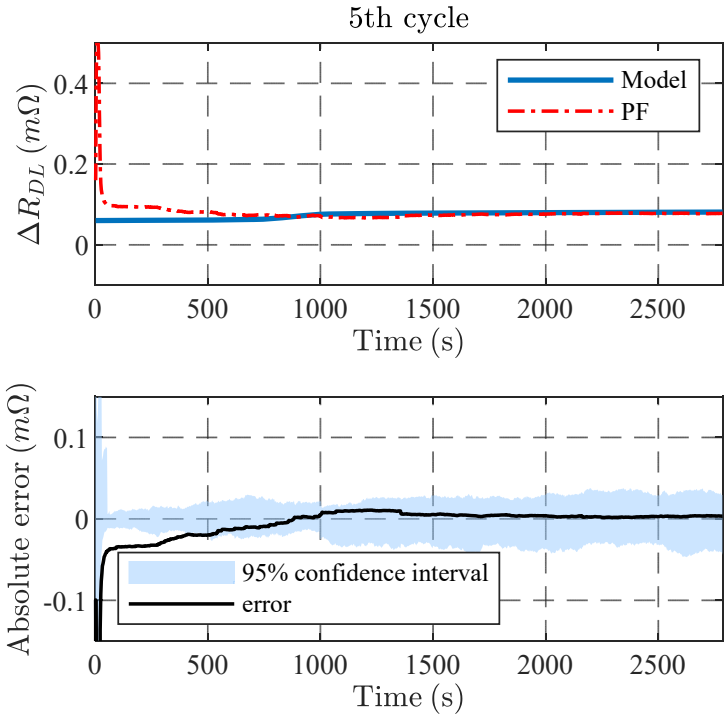

Figure 27. Comparison of deposit resistance with its absolute error together with the 95% confidence interval at the fifth cycle.

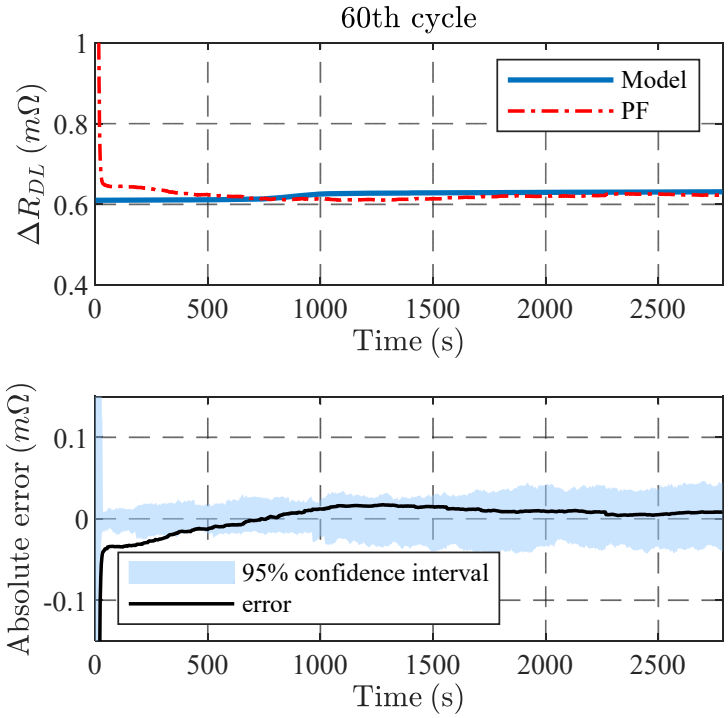

Figure 28. Comparison of deposit resistance with its absolute error together with the 95% confidence interval at the 60th cycle.

4.4.2 Aging parameters estimation as a function of cycle number

At a larger time scale, estimated aging parameters as a function of cycle number are plotted in Figure 29. As shown in Figure 29(a), Q_{LLI} increases nonlinearly as the number of cycles increases, due to the continuous consumption of recyclable lithium ions involved in the reaction of SEI formation and lithium plating. On the other hand, the deposit layer resistance also increases, which is proportional to the ion loss. Because the P2D model is applied only to the negative electrode, the change in SEI resistance is estimated along the thickness direction, as shown in Figure 29(c). The x-axis denotes the dimensionless electrode thickness. Specifically, $\delta_{neg,dimensionless} = 0$ and $\delta_{neg,dimensionless} = 1$ represent the location of the interface between the current collector and the composite electrode, as well as that between the composite electrode and the separator, respectively. Toward the separator where $\delta_{neg,dimensionless} = 1$, the ΔR_{SEI} increases faster due to the higher side reaction rate. Accordingly, Figure 29(c) shows that the volume fraction of the solid decreases as the cycle number increases due to the loss of active material, with higher magnitude toward the separator.

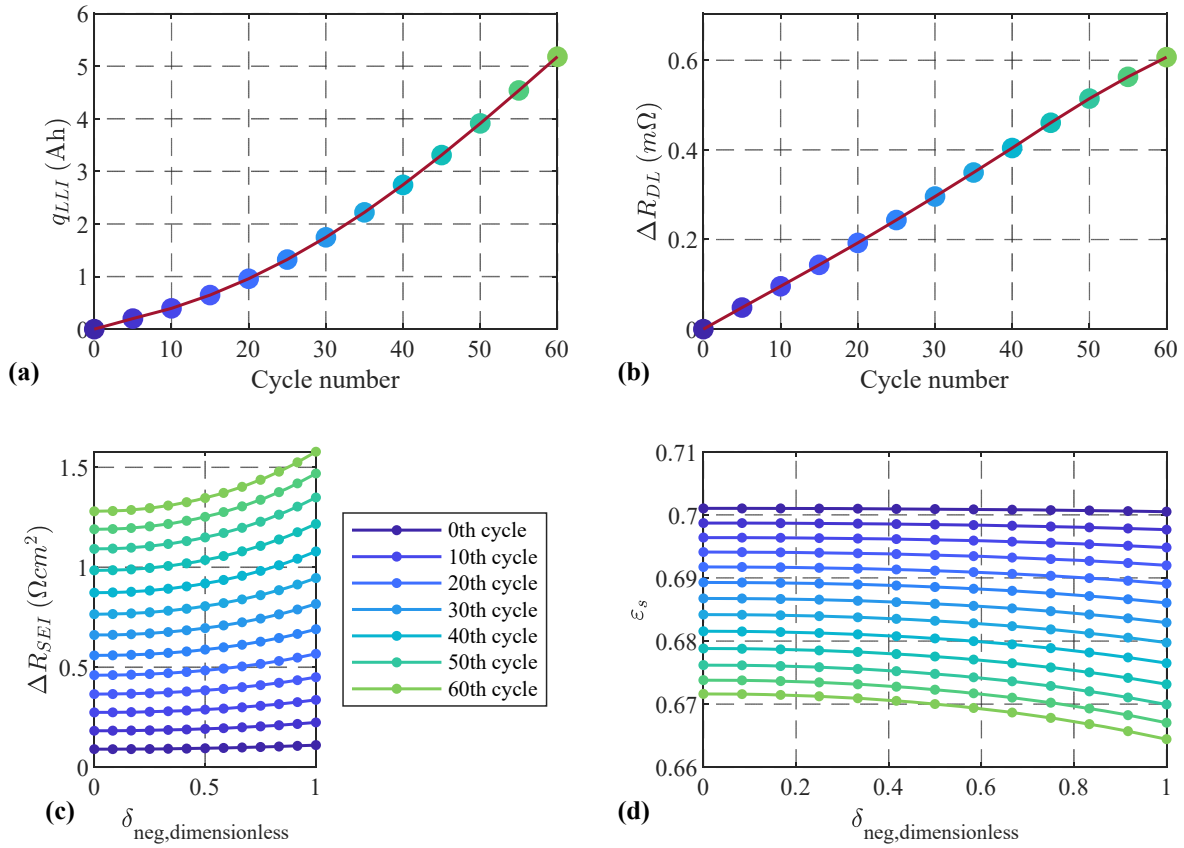

Figure 29. Estimation of four degradation parameters as functions of cycle number: (a) change in lihtium ion loss (b) change in deposit layer resistance; (c) change in SEI resistance along electrode thickness direction; (d) change in volume fraction of negative electrode along electrode thickness direction.

4.4.3 SOH estimation

Here, we demonstrate the estimation performance when the capacity is initialized with a 5% error. Figure 30(a) and (b) represent the convergence of the SOH_Q estimation to its measured values at the first and 60th cycles, respectively. The solid blue line represents the measured SOH_Q that are 100% and 75%, respectively, and the solid red line represents the estimated values that are calculated by taking the mean of the particles of the filter. The convergence time is 2000 s, and

1100 s, respectively, when the sampling period is selected to be 2.5 s. The convergence time can be further reduced by reducing the sampling period. In addition, the convergence speed can be 'tuned' by varying the covariance of the process and measurement error. However, because of the slow-changing nature of the SOH, the time constant of the estimator is already much faster than that of the dynamics of the SOH, which makes the estimator adequate. In practice, the performance needs to be adjusted by tuning the filter to meet the design requirements.

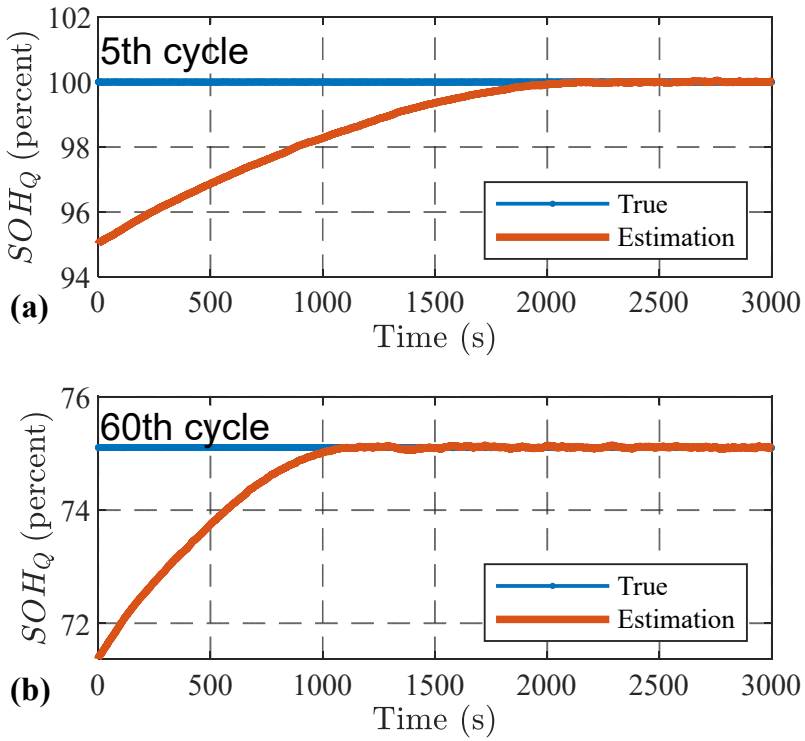

Figure 30. Comparison between estimated and measured SOH_Q with 5% initial error at the fifth and the 60th cycle.

The SOH_Q estimations from the beginning-of-life to the EOL under 0°C, 25°C, and 45°C, and different C-rates are shown in Figure 31(a). The dots, and markers denote the experimental data, and online estimation results, respectively. Because the particle filter incorporates the information of SOC and terminal voltage measurements, the estimation accuracy has been improved compared to the validation results using the model only. The SOH_Q error between the

experimental data and online estimation is shown in Figure 31(b), which is less than 3%. The SOH_P estimations under different temperatures and C-rates are shown in Figure 32(a). The dots and markers denote the experimental data and online estimation results, respectively. With the estimation of the change of the SEI and deposit layer resistance, the estimated power decreases as the cycle number increases. The overall error of power estimation is within 4%, as shown in Figure 32(b).

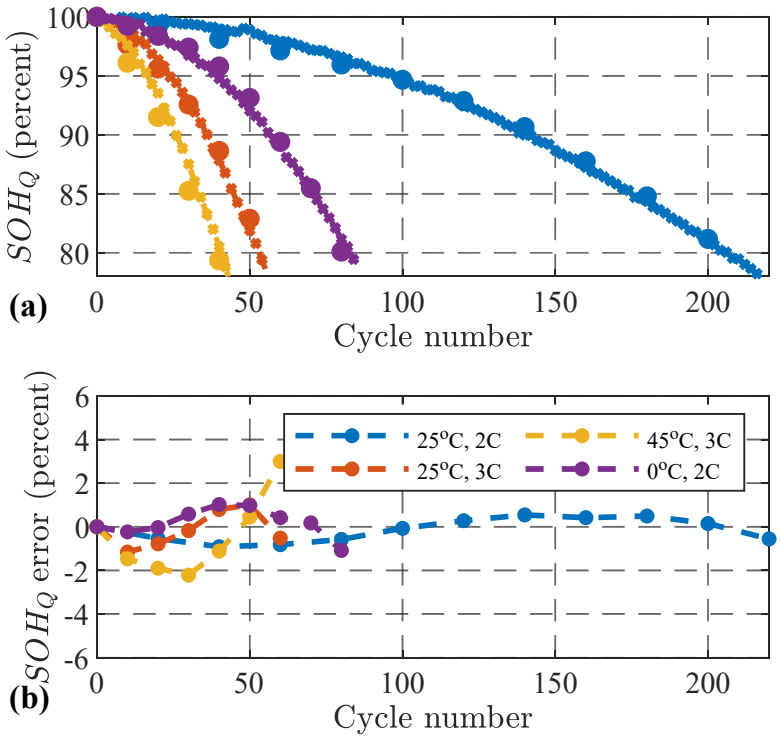

Figure 31. (a) Results of estimated SOH_Q as a function of cycle number, where the dots, and markers denote the experimental data, and online estimation results, respectively; and (b) the SOH_Q error.

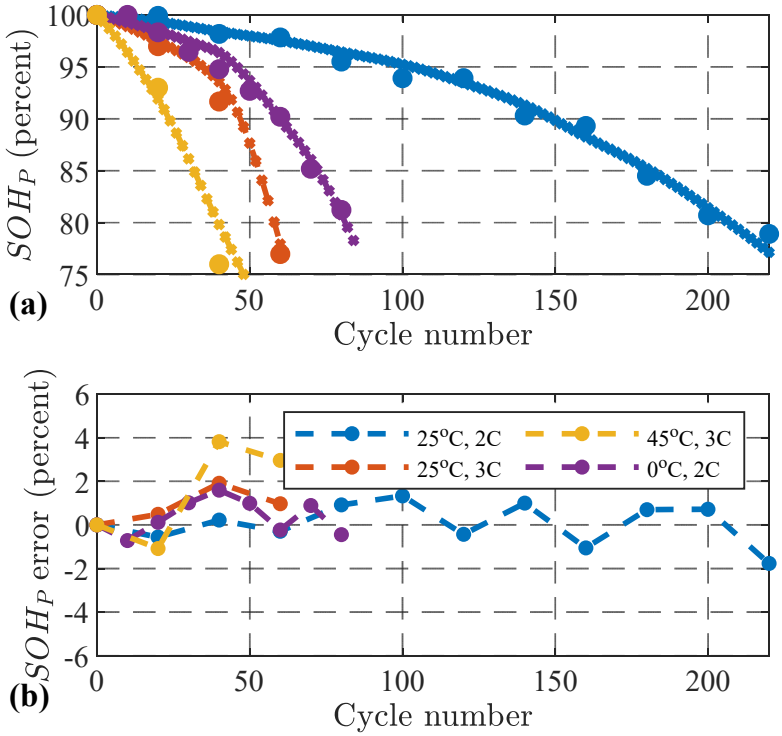

Figure 32. (a) Results of estimated SOH_P as a function of cycle number, where the dots, and markers denote the experimental data, and online estimation results, respectively; and (b) the SOH_P error.

4.4.4 Validation of BIL test

Finally, the proposed method was implemented into a battery in the loop (BIL) test station capable of running in real time. The ROM with the SOH estimation algorithm was written in a MATLAB script and embedded in the LabVIEW. At each time step, the input current profile was updated. The terminal voltage and SOC were also measured, and the difference between the measured and estimated voltage and SOC was calculated to determine SOH in real-time. To assess SOH estimation performance, an urban dynamometer driving schedule (UDDS) profile is applied in which the maximum charge and discharge current of the profile are 2.6 C and 2.3 C,

respectively, as shown in Figure 33(a). In Figure 33 (b), the solid blue line and dashed red line represent the experimentally obtained and simulated terminal voltage, respectively. The simulation shows a good match with the experimental data, and more specifically, a root-mean-square error (RMSE) of 23.6 mV is achieved, which demonstrated the fidelity of the proposed ROM-P2D-SPM, even under highly dynamic driving cycles. Figure 33(c) to (e) show the estimated and experimentally obtained maximum capacity at zeroth, 20th, and 40th cycles, which correspond to a capacity fade of 0%, 4.5%, and 10.7%, respectively. At the beginning of every cycle, a 5% initial capacity offset was added to mimic the unknown capacity of a cell at the instant. Despite the different stages of degradation, the estimated capacities always converge to the actual capacities with a convergence time in the range from 828 s to 2556 s. The difference of the convergence time is related to the accuracy of voltage and SOC estimation, which may vary slightly at different degradation conditions. Figure 33(c) shows the change of the effective sample size of the particle filter as a function of time. Specifically, a relatively small sample size of 50 is selected to avoid high computation cost. In addition, because of the 10% threshold, the resampling step takes place whenever N_{eff} is less than 5. Therefore, this BIL test has demonstrated that the proposed algorithm is capable of estimating SOH online and in real-time.

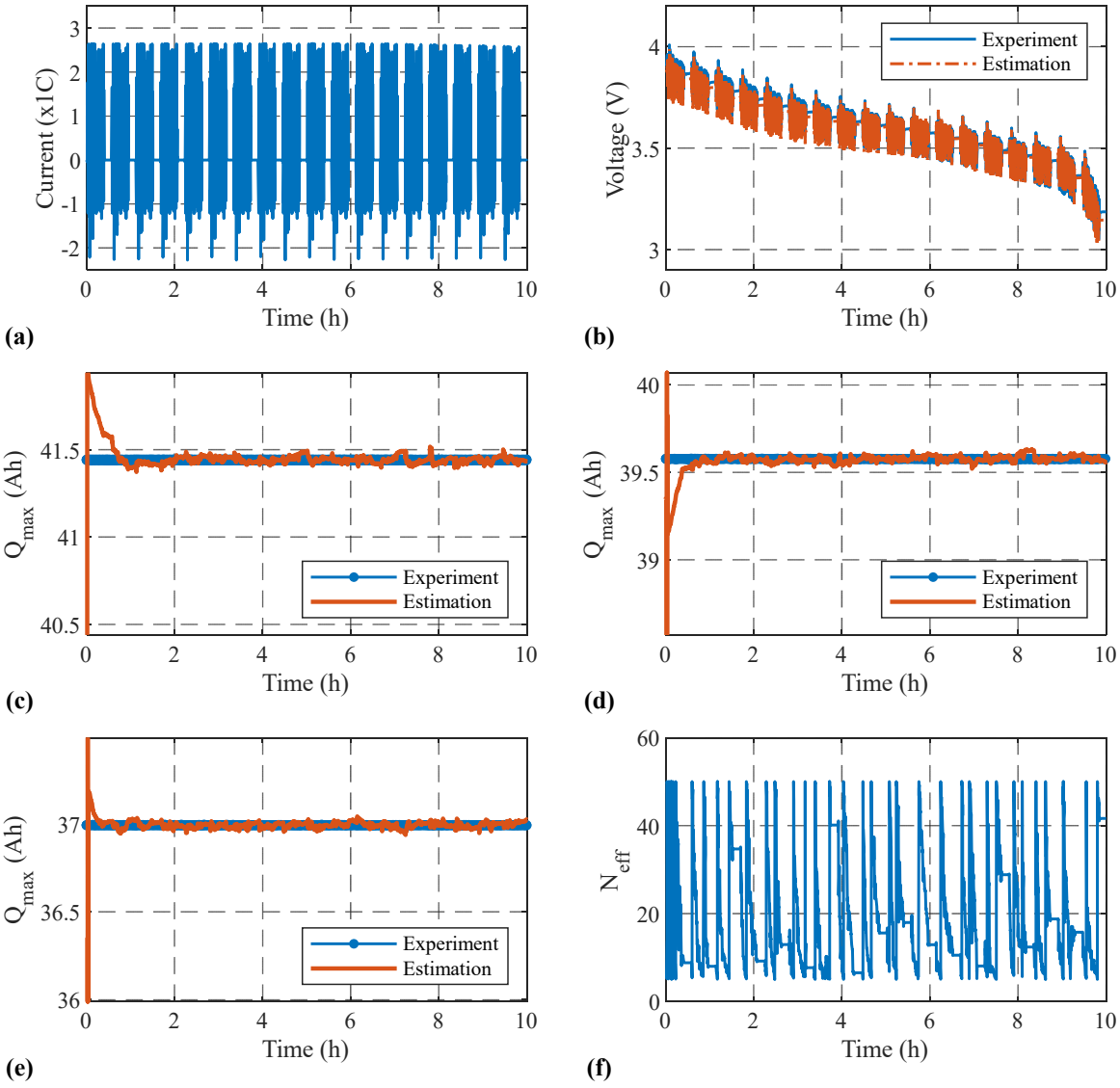

Figure 33. Results of a BIL test using a UDDS profile: (a) current profile; (b) estimated and experimentally measured terminal voltage; (c) estimated and experimentally obtained maximum capacity at zeroth; (d) 20th; and (e) 40th cycles; and (f) effective sample size.

4.5 Summary

An online SOH and aging parameter estimation method is proposed based on an ROM that considers two major degradation mechanisms. The degradation model is capable of predicting the ion loss from SEI layer formation and lithium plating, in addition to predicting the active material loss. A set of incrementally discretized state equations for aging parameter updates was also developed, and the effects of these parameters on the OCV, capacity, and power are analyzed. Then, a sensitivity analysis was conducted whereby the sensitivity of aging parameters was assessed with respect to both the terminal voltage and the SOC. We revealed that the q_{LLI} has the highest sensitivity with respect to the SOC, whereas the R_{DL} reflects the terminal voltage. According to these analyses, four aging parameters were selected for online estimation via the implementation of a particle filter. Specifically, the particle filter is applied to the discretized state equations whose inputs are the side reaction rates of SEI layer formation reaction and lithium plating, respectively. Both the terminal voltage and SOC are used for measurement updates to ensure the observability of the parameters. In addition, the results of the aging parameter and SOH estimation were analyzed at different time scales, which demonstrates the estimation accuracy with 95% confidence interval, and reveals the changing tendency of each aging parameter as a function of electrode thickness direction. The latter shows that the SEI resistance and volume fraction of the solid particle increases and decreases the most, respectively, toward the separator. This facilitates the diagnosis of cell degradation down to the thickness scale. Furthermore, the estimated SOH_Q and SOH_P are compared with the experimental data, which shows that the convergence speed within 2560 s and the maximum error is less than 3% and 4%, respectively. Finally, the proposed algorithm was tested using a BIL test station and a UDDS profile.

Chapter 5. Conclusions and future work

5.1 Conclusions

This dissertation develops an online state and parameter estimation algorithm based on a ROM with a degradation model. Using a large-format 42 Ah Li(NiMnCo)O_2/Carbon battery throughout this work, we:

1. Develop and experimentally validate a parameter estimation procedure to estimate sensitive parameters of the ROM at the BOL. This procedure achieves automatic estimation without human intervention to obtain accurate and fast key parameter estimation.

2. Design an SR-SPKF based nonlinear estimator with equality constraints and adaptive error covariance update to estimate SOC with improved speed and accuracy, and, equally importantly, surface and average concentrations inside the battery from only applied current and voltage measurements.

3. Employ a particle filter for online aging parameter and SOH estimation based on a reformulated, control-oriented incremental aging model with the consideration of two major degradation mechanisms. The SOH and aging parameters are monitored from real-time current and terminal voltage measurements even when the present capacity is not available.

In summary, this work develops a parameter and state estimation framework throughout battery life. When a fresh cell is received from the manufacturer, a set of a baseline test, which consists of CC-CV charge and CC discharge under different temperatures, is conducted for automatic BOL parameter estimation. This allows for obtaining an optimal parameter set with

minimized terminal voltage error (Chapter 2). Once the BOL parameters are obtained, an adaptive nonlinear filter is incorporated so that internal states, such as lithium ion surface and average concentration, and the SOC are estimated online and in real time. Apart from monitoring cell SOC, the estimator also provides accurate information on internal states that can be potentially used for online charging strategy design (Chapter 3). During repeated cycles, the developed aging parameter and SOH estimator is applied to continuously monitor the health of a cell as it ages toward the EOL, which enables detection of local cell degradation and failure (Chapter 4).

Moreover, the developed scheme exhibits excellent performance that is comparable to ECM-based and empirical methods presently used in the industry. Specifically, these achievements are:

- The automatic parameter estimation procedure can achieve accurate terminal voltage estimation whose RMSE is less than 12 mV [63].
- The SOC estimator achieves a maximum SOC error that is less than 3% [26].
- The SOH and parameter estimator achieves maximum relative errors of capacity and power fade are less than 3% and 4%, respectively, up to 30% capacity and power fade [49].

5.2 Future work

5.2.1 SOC and SOH co-estimation at a wider temperature range

The SOC and SOH should be estimated simultaneously to improve estimation accuracy. Generally, co-estimation may be achieved either via a joint estimator (using one filter with combined states) or a dual estimator (using two separator estimators within one feedback loop). The joint estimator would result in large matrix operations due to the high dimensionality of the

combined states and poor numeric conditioning due to the different time scales of SOC and SOH, as well as vastly different magnitudes of states and parameters. Therefore, the latter is recommended because a dual estimator is able to take consideration of different time scales to improve estimation efficiency, as well as incorporate individually developed filters without modification. However, additional technical challenges remain, such as by decoupling SOC from SOH estimation, the cross-correlations between the two are lost, leading to the possibility of poorer estimation accuracy overall. In addition, when initial offsets are present in both SOC and SOH, the 'accuracy' model assumption of nonlinear filtering would no longer hold, which could potentially lead to failure in convergence. To address these challenges, it is important to carefully design the updating time scales of SOC and SOH as well as the structure of the dual filter. Moreover, in order to develop a complete estimation scheme, experimental validation of subzero temperatures (i.e., -30 ºC to 0 ºC) is as equally important as that of the above-zero temperatures discussed in this work. For subzero temperatures, lithium plating and stripping mechanisms need to be further investigated to obtain a high-fidelity model for estimation.

5.2.2 Physical-informed deep neural network for battery state estimation

Due to the drastic increase of computational power and the availability of a large amount of electric vehicle battery data, a number of data-driven methods have been investigated [64,65]. In particular, due to the complicated and also not fully understood aging mechanisms of battery, the data-driven method may be considered to be a new approach for modeling such mechanisms. However, existing implementations are mainly focused on extract information purely from data and overlook its underlining physics insight. Therefore, to improve the interpretability of such data-driven model, deep neural networks can be combined with PDEs and used for tasks such as model order reduction [66,67], and parameter estimation [68] by constructing the network to

minimize errors of differential operator, initial condition, and boundary conditions. Moreover, the degradation model developed in this work can be incorporated into the data generation process for model training to obtain a map between the input data to internal states and aging parameters. One the one hand, this proposed approach may release the experimental effort since the training data can be generated using the PDEs. On the other hand, once the physical-informed deep neural network is well trained, it can replace the original PDE, and hence reduce the computational complexity while maintaining the model accuracy. The proposed approach aims to combine both the advantages of physics-based and data-driven modeling, and can be easy generalized to any chemistry and even next-generation batteries.

Reference

[1] S. Santhanagopalan, R.E. White, Online estimation of the state of charge of a lithium ion cell, J. Power Sources. 161 (2006) 1346–1355. doi:10.1016/j.jpowsour.2006.04.146.

[2] L. Zhang, L. Wang, G. Hinds, C. Lyu, J. Zheng, J. Li, Multi-objective optimization of lithium-ion battery model using genetic algorithm approach, J. Power Sources. 270 (2014) 367–378. doi:10.1016/j.jpowsour.2014.07.110.

[3] A. Jokar, B. Rajabloo, M. Désilets, M. Lacroix, An Inverse Method for Estimating the Electrochemical Parameters of Lithium-Ion Batteries I. Methodology, J. Electrochem. Soc. 163 (2016) A2876–A2886. doi:10.1149/2.0191614jes.

[4] B. Rajabloo, A. Jokar, M. Désilets, M. Lacroix, An Inverse Method for Estimating the Electrochemical Parameters of Lithium-Ion Batteries, J. Electrochem. Soc. 164 (2017) A99–A105. doi:10.1149/2.0221702jes.

[5] M.A. Rahman, S. Anwar, A. Izadian, Electrochemical model parameter identification of a lithium-ion battery using particle swarm optimization method, J. Power Sources. 307 (2016) 86–97. doi:10.1016/j.jpowsour.2015.12.083.

[6] S.J. Moura, F.B. Argomedo, R. Klein, A. Mirtabatabaei, M. Krstic, Battery State Estimation for a Single Particle Model with Electrolyte Dynamics, IEEE Trans. Control Syst. Technol. 25 (2017) 453–468. doi:10.1109/TCST.2016.2571663.

[7] Y. Zhao, S.-Y. Choe, A highly efficient reduced order electrochemical model for a large format LiMn2O4/Carbon polymer battery for real time applications, Electrochim. Acta. 164 (2015) 97–107. doi:10.1016/j.electacta.2015.02.182.

[8] M. Ecker, T.K.D. Tran, P. Dechent, S. Kabitz, A. Warnecke, D.U. Sauer, Parameterization of a Physico-Chemical Model of a Lithium-Ion Battery: I. Determination of Parameters, J. Electrochem. Soc. 162 (2015) A1836–A1848. doi:10.1149/2.0551509jes.

[9] A. V. Randall, R.D. Perkins, X. Zhang, G.L. Plett, Controls oriented reduced order modeling of solid-electrolyte interphase layer growth, J. Power Sources. 209 (2012) 282–288. doi:10.1016/j.jpowsour.2012.02.114.

[10] K.H. Xue, G.L. Plett, A convective transport theory for high rate discharge in lithium ion cells, Electrochim. Acta. 87 (2013) 575–590. doi:10.1016/j.electacta.2012.09.109.

[11] T.S. Dao, C.P. Vyasarayani, J. McPhee, Simplification and order reduction of lithium-ion battery model based on porous-electrode theory, J. Power Sources. 198 (2012) 329–337. doi:10.1016/j.jpowsour.2011.09.034.

[12] P. Ramadass, B. Haran, P.M. Gomadam, R. White, B.N. Popov, Development of First Principles Capacity Fade Model for Li-Ion Cells, J. Electrochem. Soc. 151 (2004) 196–203. doi:10.1149/1.1634273.

[13] S. Santhanagopalan, Q. Guo, P. Ramadass, R.E. White, Review of models for predicting the cycling performance of lithium ion batteries, J. Power Sources. 156 (2006) 620–628.

doi:10.1016/j.jpowsour.2005.05.070.

[14] S. Santhanagopalan, Q. Guo, R.E. White, Parameter Estimation and Model Discrimination for a Lithium-Ion Cell, J. Electrochem. Soc. 154 (2007) A198. doi:10.1149/1.2422896.

[15] S.G. Stewart, V. Srinivasan, J. Newman, Modeling the Performance of Lithium-Ion Batteries and Capacitors during Hybrid-Electric-Vehicle Operation, J. Electrochem. Soc. 155 (2008) A664. doi:10.1149/1.2953524.

[16] G.L. Plett, Extended Kalman filtering for battery management systems of LiPB-based HEV battery packs - Part 3. State and parameter estimation, J. Power Sources. 134 (2004) 277–292. doi:10.1016/j.jpowsour.2004.02.033.

[17] K. Smith, C.-Y. Wang, Power and thermal characterization of a lithium-ion battery pack for hybrid-electric vehicles, J. Power Sources. 160 (2006) 662–673. doi:10.1016/j.jpowsour.2006.01.038.

[18] Y. Zhao, S.-Y. Choe, J. Kee, Modeling of degradation effects and its integration into electrochemical reduced order model for Li(MnNiCo)O2/Graphite polymer battery for real time applications, Electrochim. Acta. 270 (2018) 440–452. doi:10.1016/j.electacta.2018.02.086.

[19] X. Zhao, Y. Bi, S.-Y. Choe, S.-Y. Kim, An integrated reduced order model considering degradation effects for LiFePO4/graphite cells, Electrochim. Acta. 280 (2018) 41–54. doi:10.1016/j.electacta.2018.05.091.

[20] Y. Yin, Y. Hu, S.-Y. Choe, H. Cho, W.T. Joe, New fast charging method of lithium-ion batteries based on a reduced order electrochemical model considering side reaction, J. Power Sources. 423 (2019) 367–379. doi:10.1016/j.jpowsour.2019.03.007.

[21] M. Doyle, Modeling of Galvanostatic Charge and Discharge of the Lithium/Polymer/Insertion Cell, J. Electrochem. Soc. 140 (1993) 1526. doi:10.1149/1.2221597.

[22] R. Van der Merwe, E.A. Wan, The square-root unscented Kalman filter for state and parameter-estimation, 2001 IEEE Int. Conf. Acoust. Speech, Signal Process. Proc. (Cat. No.01CH37221). 6 (n.d.) 3461–3464. doi:10.1109/ICASSP.2001.940586.

[23] D. Di Domenico, A. Stefanopoulou, G. Fiengo, Lithium-Ion Battery State of Charge and Critical Surface Charge Estimation Using an Electrochemical Model-Based Extended Kalman Filter, J. Dyn. Syst. Meas. Control. 132 (2010) 061302. doi:10.1115/1.4002475.

[24] K.D. Stetzel, L.L. Aldrich, M.S. Trimboli, G.L. Plett, Electrochemical state and internal variables estimation using a reduced-order physics-based model of a lithium-ion cell and an extended Kalman filter, J. Power Sources. 278 (2015) 490–505. doi:10.1016/j.jpowsour.2014.11.135.

[25] E.A. Wan, R. Van Der Merwe, The unscented Kalman filter for nonlinear estimation, Adapt. Syst. Signal Process. Commun. Control Symp. 2000. AS-SPCC. IEEE 2000. (2002) 153–158. http://ieeexplore.ieee.org/xpls/abs_all.jsp?arnumber=882463.

[26] G.L. Plett, Sigma-point Kalman filtering for battery management systems of LiPB-based

HEV battery packs. Part 2: Simultaneous state and parameter estimation Gregory, J. Power Sources. 161 (2006) 1356–1368. doi:10.1016/j.jpowsour.2006.06.003.

[27] Y. Wang, C. Liu, R. Pan, Z. Chen, Modeling and state-of-charge prediction of lithium-ion battery and ultracapacitor hybrids with a co-estimator, Energy. 121 (2017) 739–750. doi:10.1016/j.energy.2017.01.044.

[28] F. Yang, Y. Xing, D. Wang, K.L. Tsui, A comparative study of three model-based algorithms for estimating state-of-charge of lithium-ion batteries under a new combined dynamic loading profile, Appl. Energy. 164 (2016) 387–399. doi:10.1016/j.apenergy.2015.11.072.

[29] X. Li, M. Xiao, S.-Y. Choe, Reduced order model (ROM) of a pouch type lithium polymer battery based on electrochemical thermal principles for real time applications, Electrochim. Acta. 97 (2013) 66–78. doi:10.1016/j.electacta.2013.02.134.

[30] N. Magnus, N.K. Poulsen, O. Ravn, New developments in state estimation for nonlinear systems, 36 (2000) 1627–1638.

[31] J. Du, Z. Liu, Y. Wang, State of charge estimation for Li-ion battery based on model from extreme learning machine, Control Eng. Pract. 26 (2014) 11–19. doi:10.1016/j.conengprac.2013.12.014.

[32] Y. Wang, C. Zhang, Z. Chen, A method for joint estimation of state-of-charge and available energy of LiFePO4 batteries, Appl. Energy. 135 (2014) 81–87. doi:10.1016/j.apenergy.2014.08.081.

[33] X. Song, F. Yang, D. Wang, K.-L. Tsui, Combined CNN-LSTM Network for State-of-Charge Estimation of Lithium-Ion Batteries, IEEE Access. 7 (2019) 88894–88902. doi:10.1109/access.2019.2926517.

[34] C. Zhang, Y. Zhu, G. Dong, J. Wei, Data-driven lithium-ion battery states estimation using neural networks and particle filtering, Int. J. Energy Res. (2019) er.4820. doi:10.1002/er.4820.

[35] G.L. Plett, Extended Kalman filtering for battery management systems of LiPB-based HEV battery packs: Part 1. Background, J. Power Sources. 134 (2004) 262–276. doi:10.1016/j.jpowsour.2004.02.032.

[36] J. Vetter, P. Novák, M.R. Wagner, C. Veit, K.C. Möller, J.O. Besenhard, M. Winter, M. Wohlfahrt-Mehrens, C. Vogler, A. Hammouche, Ageing mechanisms in lithium-ion batteries, J. Power Sources. 147 (2005) 269–281. doi:10.1016/j.jpowsour.2005.01.006.

[37] R. Xiong, L. Li, J. Tian, Towards a smarter battery management system: A critical review on battery state of health monitoring methods, J. Power Sources. 405 (2018) 18–29. doi:10.1016/j.jpowsour.2018.10.019.

[38] P. Ramadass, B. Haran, P.M. Gomadam, R. White, B.N. Popov, Development of First Principles Capacity Fade Model for Li-Ion Cells, J. Electrochem. Soc. 151 (2004) A196. doi:10.1149/1.1634273.

[39] M. Song, S.-Y. Choe, Fast and safe charging method suppressing side reaction and lithium

deposition reaction in lithium ion battery, J. Power Sources. 436 (2019) 226835. doi:10.1016/j.jpowsour.2019.226835.

[40] C. von Lüders, J. Keil, M. Webersberger, A. Jossen, Modeling of lithium plating and lithium stripping in lithium-ion batteries, J. Power Sources. 414 (2019) 41–47. doi:10.1016/j.jpowsour.2018.12.084.

[41] X. Zhao, Y. Yin, Y. Hu, S.-Y. Choe, Electrochemical-thermal modeling of lithium plating/stripping of Li(Ni 0.6 Mn 0.2 Co 0.2)O 2 /Carbon lithium-ion batteries at subzero ambient temperatures, J. Power Sources. 418 (2019) 61–73. doi:10.1016/j.jpowsour.2019.02.001.

[42] P. Arora, R.E. White, M. Doyle, Capacity fade mechanisms and side reactions in lithium-ion batteries, J. Electrochem. Soc. 145 (1998) 3647–3667. doi:10.1149/1.1838857.

[43] P. Arora, Mathematical Modeling of the Lithium Deposition Overcharge Reaction in Lithium-Ion Batteries Using Carbon-Based Negative Electrodes, J. Electrochem. Soc. 146 (1999) 3543. doi:10.1149/1.1392512.

[44] X.G. Yang, C.Y. Wang, Understanding the trilemma of fast charging, energy density and cycle life of lithium-ion batteries, J. Power Sources. 402 (2018) 489–498. doi:10.1016/j.jpowsour.2018.09.069.

[45] R. Fu, S.-Y. Choe, V. Agubra, J. Fergus, Modeling of degradation effects considering side reactions for a pouch type Li-ion polymer battery with carbon anode, J. Power Sources. 261 (2014) 120–135. doi:10.1016/j.jpowsour.2014.03.045.

[46] R. Fu, S.-Y. Choe, V. Agubra, J. Fergus, Development of a physics-based degradation model for lithium ion polymer batteries considering side reactions, J. Power Sources. 278 (2015) 506–521. doi:10.1016/j.jpowsour.2014.12.059.

[47] R. Xiong, L. Li, Z. Li, Q. Yu, H. Mu, An electrochemical model based degradation state identification method of Lithium-ion battery for all-climate electric vehicles application, Appl. Energy. 219 (2018) 264–275. doi:10.1016/j.apenergy.2018.03.053.

[48] S. Schwunk, N. Armbruster, S. Straub, J. Kehl, M. Vetter, Particle filter for state of charge and state of health estimation for lithium-iron phosphate batteries, J. Power Sources. 239 (2013) 705–710. doi:10.1016/j.jpowsour.2012.10.058.

[49] E. Shi, F. Xia, D. Peng, L. Li, X. Wang, B. Yu, State-of-health estimation for lithium battery in electric vehicles based on improved unscented particle filter, J. Renew. Sustain. Energy. 11 (2019). doi:10.1063/1.5065477.

[50] D. Ren, K. Smith, D. Guo, X. Han, X. Feng, L. Lu, M. Ouyang, J. Li, Investigation of lithium plating-stripping process in Li-ion batteries at low temperature using an electrochemical model, J. Electrochem. Soc. 165 (2018) A2167–A2167. doi:10.1149/2.0661810jes.

[51] M. Tang, P. Albertus, J. Newman, Two-Dimensional Modeling of Lithium Deposition during Cell Charging, J. Electrochem. Soc. 156 (2009) A390. doi:10.1149/1.3095513.

[52] Y. Bi, S.-Y. Choe, Automatic Estimation of Parameters of a Reduced Order

Electrochemical Model for Lithium-ion Batteries at the Beginning-of-life, 2018 IEEE Veh. Power Propuls. Conf. (2018) 1–6. doi:10.1109/VPPC.2018.8604954.

[53] J. Zhu, M.S. Dewi Darma, M. Knapp, D.R. Sørensen, M. Heere, Q. Fang, X. Wang, H. Dai, L. Mereacre, A. Senyshyn, X. Wei, H. Ehrenberg, Investigation of lithium-ion battery degradation mechanisms by combining differential voltage analysis and alternating current impedance, J. Power Sources. 448 (2020) 28–30. doi:10.1016/j.jpowsour.2019.227575.

[54] A. Cordoba-Arenas, S. Onori, Y. Guezennec, G. Rizzoni, Capacity and power fade cycle-life model for plug-in hybrid electric vehicle lithium-ion battery cells containing blended spinel and layered-oxide positive electrodes, J. Power Sources. 278 (2015) 473–483. doi:10.1016/j.jpowsour.2014.12.047.

[55] Q. Lai, S. Jangra, H.J. Ahn, G. Kim, W.T. Joe, X. Lin, Analytical sensitivity analysis for battery electrochemical parameters, in: Proc. Am. Control Conf., 2019: pp. 890–896. doi:10.23919/acc.2019.8814950.

[56] N. Legrand, B. Knosp, P. Desprez, F. Lapicque, S. Raël, Physical characterization of the charging process of a Li-ion battery and prediction of Li plating by electrochemical modelling, J. Power Sources. 245 (2014) 208–216. doi:10.1016/j.jpowsour.2013.06.130.

[57] Y. Bi, X. Zhao, S.-Y. Choe, A Hybrid State of Charge Estimation Method of a LiFePO 4 /Graphite Cell Using a Reduced Order Model with an Extended Kalman Filter, in: 2019 Am. Control Conf., IEEE, 2019: pp. 3155–3160. doi:10.23919/ACC.2019.8814310.

[58] Y. Bi, S.-Y. Choe, An adaptive sigma-point Kalman filter with state equality constraints for online state-of-charge estimation of a Li (NiMnCo) O 2 / Carbon battery using a reduced-order electrochemical model, Appl. Energy. 257 (2019) 113925. doi:10.1016/j.apenergy.2019.113925.

[59] J. Bi, T. Zhang, H. Yu, Y. Kang, State-of-health estimation of lithium-ion battery packs in electric vehicles based on genetic resampling particle filter, Appl. Energy. 182 (2016) 558–568. doi:10.1016/j.apenergy.2016.08.138.

[60] G.L. Plett, Sigma-point Kalman filtering for battery management systems of LiPB-based HEV battery packs. Part 1: Introduction and state estimation, J. Power Sources. 161 (2006) 1356–1368. doi:10.1016/j.jpowsour.2006.06.003.

[61] A. Doucet, S. Godsill, C. Andrieu, On sequential Monte Carlo sampling methods for Bayesian filtering, Stat. Comput. (2000) 197–208. doi:10.1023/A:1008935410038.

[62] M.S. Arulampalam, S. Maskell, N. Gordon, T. Clapp, A tutorial on particle filters for online nonlinear/non-Gaussian Bayesian tracking, IEEE Trans. Signal Process. 50 (2002) 174–188. doi:10.1109/78.978374.

[63] G.L. Plett, Extended Kalman filtering for battery management systems of LiPB-based HEV battery packs - Part 2. Modeling and identification, J. Power Sources. 134 (2004) 262–276. doi:10.1016/j.jpowsour.2004.02.032.

[64] K.A. Severson, P.M. Attia, N. Jin, N. Perkins, B. Jiang, Z. Yang, M.H. Chen, M. Aykol, P.K. Herring, D. Fraggedakis, M.Z. Bazant, S.J. Harris, W.C. Chueh, R.D. Braatz, Data-

driven prediction of battery cycle life before capacity degradation, Nat. Energy. 4 (2019) 383–391.

[65] X. Li, L. Zhang, Z. Wang, P. Dong, Remaining useful life prediction for lithium-ion batteries based on a hybrid model combining the long short-term memory and Elman neural networks, J. Energy Storage. 21 (2019) 510–518. doi:10.1016/j.est.2018.12.011.

[66] J.N. Kani, A.H. Elsheikh, DR-RNN: A deep residual recurrent neural network for model reduction, (2017). http://arxiv.org/abs/1709.00939.

[67] Y. Yu, H. Yao, Y. Liu, Aircraft dynamics simulation using a novel physics-based learning method, Aerosp. Sci. Technol. 87 (2019) 254–264. doi:10.1016/j.ast.2019.02.021.

[68] M. Raissi, P. Perdikaris, G.E. Karniadakis, Physics-informed neural networks: A deep learning framework for solving forward and inverse problems involving nonlinear partial differential equations, J. Comput. Phys. 378 (2019) 686–707. doi:10.1016/j.jcp.2018.10.045.

Appendix 1

Model parameters used in the ROM.

Parameter	*Negative electrode*	*Separator*	*Positive electrode*	*unit*
Thickness, δ	1.14×10^{-2}			*m*
Maximum solid phase concentration, $c_{s,max}$	3.05×10^{4}		4.98×10^{4}	*mol·m^{-3}*
Ionic conductivity in solid, σ	100		1	*S m^{-1}*
Diffusion coefficient in solid, D_s	*D_s=f(T)*			*m^2 s^{-1}*
Diffusion coefficient in electrolyte, D_e	*D_e=f(T)*			*m^2 s^{-1}*
Stoichiometry at 0% SOC, $Stoi_0$	0.0450		0.8818	
Stoichiometry at 100% SOC, $Stoi_{100}$	0.9550		0.1182	
Exchange current density, i_0	13.2×10^{4}	0	6.79×10^{4}	*A m^{-2}*
Charge-transfer coefficients,α_a, α_c	0.5,0.5		0.5,0.5	
Bruggeman porosity exponent, p	1.5	1.5	1.5	
Li+ transference number, t_+^0	0.363	0.363	0.363	
Electrolyte phase ionic conductivity,κ	$\kappa = 11.06\, c_e \exp\left[-8900\, c_e^{1.4}\right]$			*S m^{-1}*
Equilibrium potential of NMC	$U_{pos}(x) = 0.6379 + 0.5416\exp(-305.5309x) + 0.0440\tanh\left(-\frac{x-0.1958}{0.1088}\right) - 0.1978\tanh\left(\frac{x-1.0571}{0.0854}\right) - 0.6875\tanh\left(\frac{x+0.0117}{0.0529}\right) - 0.0175\tanh\left(\frac{x-0.5692}{0.0875}\right)$			*V*
Equilibrium potential of Li_xC	$U_{neg}(y) = 3.4323 + 0.8428\exp(-80.2493y) + 3.2474\times10^{-6}\exp\left(20.2645y^{3.8003}\right) - 3.2482\times10^{-6}\exp\left(20.2646y^{3.7995}\right)$			*V*

Appendix 2

Test matrix used in this work.

<table>
<tr><th colspan="5">Test for automatic parameters estimation</th></tr>
<tr><td>Types</td><td>Temperature</td><td>Current</td><td>SOC range</td><td>Determined parameters</td></tr>
<tr><td>Initial cycles</td><td>25°C</td><td>1C</td><td>0% – 100%</td><td>-</td></tr>
<tr><td>OCV-SOC curve</td><td>0,15,25,35,45°C</td><td>C/3 pulse</td><td>0% – 100%</td><td>$U_{eq,neg}$, $U_{eq,pos}$</td></tr>
<tr><td>Capacity measurement</td><td>25°C</td><td>C/3</td><td>0% – 100%</td><td>$Q_{max}, c_{s,max}$</td></tr>
<tr><td>EIS test</td><td>25°C</td><td>3 A (AC)</td><td>50%</td><td>R_{SEI}</td></tr>
<tr><td>Baseline data collection</td><td>0,15,25,35,45°C</td><td>C/5, C/2, 1C, 2C</td><td>0% – 100%</td><td>$D_{s,neg}$, $D_{s,pos}, D_e$, R_0</td></tr>
<tr><th colspan="5">Test for degradation model validation</th></tr>
<tr><td>Types</td><td>Temperature</td><td>Current</td><td>SOC range</td><td>Characteristic test</td></tr>
<tr><td rowspan="5">Cycle test</td><td>0°C</td><td>1C/1C</td><td>0% – 100%</td><td rowspan="5">• Every 20 cycles
• Capacity measurement at C/3, 25°C
• EIS test at 50% SOC, 25°C</td></tr>
<tr><td>15°C</td><td rowspan="4">2C/1C
3C/1C</td><td rowspan="4">0% – 100%</td></tr>
<tr><td>25°C</td></tr>
<tr><td>35°C</td></tr>
<tr><td>45°C</td></tr>
</table>